Cellular responses to complex strain fields studied in microfluidic devices

Sophie Chagnon-Lessard

A thesis submitted to the Faculty of Graduate and Postdoctoral Studies in partial fulfillment of the requirements for the degree of

Doctoral of Philosophy in Physics

Department of Physics
Faculty of Science
University of Ottawa, Canada

À la douce mémoire de Pauline Moisan,

ta force, ta générosité et ton cœur d'enfant ont inspiré ce travail.

ABSTRACT

Cells in living organisms are constantly experiencing a variety of mechanical cues. From the stiffness of the extra cellular matrix to its topography, not to mention the presence of shear stress and tension, the physical characteristics of the microenvironment shape the cells' fate. A rapidly growing body of work shows that cellular responses to these stimuli constitute regulatory mechanisms in many fundamental biological functions. Substrate strains were previously shown to be sensed by cells and activate diverse biochemical signaling pathways, leading to major remodeling and reorganization of cellular structures. The majority of studies had focused on the stretching avoidance response in near-uniform strain fields. Prior to this work, the cellular responses to complex planar strain fields were largely unknown. In this thesis, we uncover various aspects of strain sensing and response by first developing a tailored lab-on-a-chip platform that mimics the non-uniformity and complexity of physiological strains. These microfluidic cell stretchers allow independent biaxial control, generate cyclic stretching profiles with biologically relevant strain and strain gradient amplitudes, and enable high resolution imaging of on-chip cell cultures. Using these microdevices, we reveal that strain gradients are potent mechanical cues by uncovering the phenomenon of cell gradient avoidance. This work establishes that the cellular mechanosensing machinery can sense and localize changes in strain amplitude, which orchestrate a coordinated cellular response. Subsequently, we investigate the effect of multiple changes in stretching directions to further explore mechanosensing subtleties. The evolution of the cellular response shed light on the interplay of the strain avoidance and the newly demonstrated strain gradient avoidance, which were found to occur on two different time scales. Finally, we extend our work to study the influence of cyclic strains on the early stages of cancer development in epithelial tissues (using MDCK-Ras^{V12} system), which was previously largely unexplored. This work reveals that external mechanical forces impede the healthy cells' ability to eliminate newly transformed cells and greatly promote invasive protrusions, as a result of their different mechanoresponsiveness. Overall, not only does our work reveal new insights regarding the long-range organization in population of cells, but it may also contribute to paving the way towards new approaches in cancer prevention treatments.

STATEMENT OF ORIGINALITY

To the best of the author's knowledge, the work presented in this thesis is fully original. Research and manuscript preparation were performed under the supervision of Dr. Andrew Pelling and Dr. Michel Godin in the Center for Interdisciplinary Nanophysics Laboratories in the Department of Physics at the University of Ottawa. The Chapters 2 is partially based on a manuscript published in a refereed, peer-reviewed scientific journal, while Chapter 3-5 are composed of manuscripts published, submitted, or in preparation for refereed, peer-reviewed scientific journals:

Chapter 2 is partially based on (summary of my contribution to the paper with additional technical information):

> Tremblay D., **Chagnon-Lessard, S.**, Mirzaei, M., Pelling, A.E., Godin, M. A microscale anisotropic cell stretching device for applications in mechanobiology. *Biotechnology Letters* **36,** 657-665 (2014).

Chapter 3 is an adaptation of:

> **Chagnon-Lessard, S**., Jean-Ruel, H., Godin, M., Pelling, A.E. Cellular orientation is guided by strain gradients. *Integrative Biology* **9**, 607-618 (2017).

Chapter 4 is an adaptation of:

> **Chagnon-Lessard, S**., Godin, M., Pelling, A.E. Time dependence of cellular responses to dynamic and complex strain fields. (submitted to *Integrative Biology* on April 20th 2018, BioRxiv preprint server: https://doi.org/10.1101/286625)

Chapter 5 is an adaptation of:

> **Chagnon-Lessard, S**., Jean-Ruel, H., Godin, M., Pelling, A.E. Mechanical strains drive newly transformed epithelial cells toward invasiveness. (manuscript in preparation)

OTHER CONTRIBUTIONS

Contributions to other manuscripts (not summarized in this thesis):

- Tahvildari, R., Beamish, E., Briggs, K., **Chagnon-Lessard, S.**, Sohi, A.N., Han, S., Watts, B., Tabard-Cossa, V., Godin, M. Manipulating electrical and fluidic access in integrated nanopore-microfluidic arrays using microvalves. *Small* **13**, 1602601 (2016).

- Walker, M., **Chagnon-Lessard, S.**, Godin, M., Pelling, A.E. Investigating Mechanically-Induced Intercellular Calcium Dynamics. (in preparation)

Conferences & Workshops:

- **Chagnon-Lessard, S**., Jean-Ruel, H., Godin, M., Pelling, A.E. Mechanical strains trigger invasive behaviors in newly transformed epithelial cells. World Congress of Biomechanics, Dublin, Ireland, July 2018. (talk)

- **Chagnon-Lessard, S**., Jean-Ruel, H., Godin, M., Pelling, A.E. Cellular responses to non-uniform strain employing microfluidic devices. Ottawa-Carleton Institute Symposium, Ottawa, Ontario, May 2017. (talk)

- **Chagnon-Lessard, S**., Godin, M., Pelling, A.E. Dynamics of the Earliest Stage of Epithelial Cancer under Cyclic Mechanical Strain. Cell Dynamics Workshop, Keen, Ontario, May 2014. (talk)

- **Chagnon-Lessard, S**., Tremblay, D., Godin, M., Pelling, A.E. Microfabricated cell stretcher: techniques and challenges. Cell Dynamics Workshop, Keen, Ontario, May 2013. (poster)

STATEMENTS OF CONTRIBUTIONS

I, Sophie Chagnon-Lessard, contributed the large majority of the work constituting this thesis. It includes the final design of the microstretcher, microfabrication (photolithography, PDMS molding and assembly), device characterization (strain field calculation and optical imaging capabilities), electronic and pressure control setup assembly, cell culture, cell stretching experiments, cell staining and confocal microscopy imagining (and tailoring these techniques to microdevices), overall data acquisition, image and statistical analysis, and interpretation of the results. I have first authored 3 papers. I have written the draft of these manuscripts and performed the required revisions. They are presented in Chapters 3, 4, and 5. Dr. Andrew Pelling and Dr. Michel Godin have both contributed to initiate and guide the researches, as well as to guide and revise all the manuscripts.

These manuscripts build upon a paper written by Dr. Dominique Tremblay (former postdoctoral researcher), to which I have greatly contributed. I am second author of this paper and I have summarized my contribution to this work in Chapter 2 (note that the paper itself is not included in this thesis). Dr. Godin, Dr. Mirzaei, and Dr. Tremblay have designed the initial microstretcher. Following this work, I have modified this initial generation to better suit the type of experiments presented in Chapter 3, 4, and 5.

Dr. Hubert Jean-Ruel and myself have written as a team the Maltab programs required for the data analysis. Dr. Hubert Jean-Ruel has also contributed to the revision of the manuscripts.

ACKKNOWLEDGMENTS

First of all, I thank Dr. Andrew Pelling and Dr. Michel Godin for giving me the opportunity to join their exceptional team of researchers, and for offering their support and patience during the exploration of uncharted waters. Your way to encourage research creativity has helped me navigating through this challenging interdisciplinary journey and has greatly contributed to my growth as a scientist.

My sincere thanks in advance to my thesis committee, Dr. James Harden, Dr. Mads Kaern, Dr. Emily Heath, and Dr. Craig Simmons for their insightful comments. I also express my deepest gratitude to all the members of the Pelling and Godin labs, past and present, who have contributed to make the working environment stimulating, resourceful, and importantly, very friendly.

Finalement je remercie de tout cœur ma famille, la famille Chagnon-Lessard, qui a été présente tout au long de mes études, offrant sans compter amour, aide, encouragements, et plusieurs discussions positives et enrichissantes. J'aimerais également souligner l'écoute et le support précieux de ma deuxième famille, la famille Jean-Ruel. Enfin et surtout, Hubert, merci pour ton amour et ta confiance inébranlable. Notre synergie a transformé les moments éprouvants de mon Doctorat en découvertes. Tu es une source inépuisable d'inspiration, un homme et un scientifique exceptionnel.

TABLE OF CONTENTS

LIST OF ABBREVIATIONS

- AFM - Atomic Force Microscopy
- ATCC – American Type Culture Collection
- DMEM - Dulbecco's Modified Eagle's Medium
- DMSO - Dimethyl Sulfoxide
- ECM - Extracellular Matrix
- EDAC - Epithelial Defense Against Cancer
- F-actin - Actin Filament
- FA - Focal Adhesion
- FAK - Focal Adhesion Kinase
- FBS - Fetal Bovine Serum
- FWHM – Full Width at Half Maximum
- GAP - GTPase-Activating Protein
- GEF - Guanine nucleotide Exchange Factor
- GFP - Green Fluorescent Protein
- HBSS - Hanks' Balanced Salt Solution,
- HEPES - 4-(2-hydroxyethyl)-1-piperazineethanesulfonic acid
- HFF - Human Foreskin Fibroblast
- IF - Intermediate Filament
- MDCK - Madin-Darby Canine Kidney
- MLC - Myosin Light Chain
- MLCK - Myosin Light Chain Kinase
- MT - Microtubule
- NA - Numerical Aperture
- PBS - Phosphate Buffered Saline
- PDMS - Polydimethylsiloxane
- PFA - Paraformaldehyde
- PSF - Point Spread function
- Re - Reynold number
- ROCK - Rho associated protein Kinase
- S1P - Sphingosine-1-Phosphate
- SF - Stress Fiber
- TX - Triton X-100
- WT – Wild Type

LIST OF FIGURES

LIST OF TABLES

CHAPTER 1 | INTRODUCTION

The dynamic nature of the living world raises the following question: how do mechanical forces affect the smallest unit of life, the cell? External physical cues are now recognized as key determinants of cells' fate since they constitute critical regulators of cell biochemistry[1–3]. It is established that mechanical signals play a crucial role in cellular development and homeostasis, in gene expression, and in many fundamental cellular functions. Dysregulation of the cell's physical interaction with its environment is now believed to be a common feature of a wide span of human diseases[4–6]. Despite major advances over the last decades, countless questions have yet to be elucidated and there are many uncharted waters to be explored. The essence of this work is to develop enabling tools and gain insights into the rapidly evolving field of mechanobiology, specifically to better understand the effect of external forces on the cells' fate.

The cellular microenvironment is characterized by an ensemble of physical properties which are intimately linked to the specificities of the cells and tissues they host. In addition to the passive characteristics of the extracellular matrix (ECM) such as stiffness and topography, cells are constantly bombarded with mechanical signals in the form of tension, shear stress, and compression[7,8]. Classic examples are the compression and tensile loads applied to cartilages, muscles, tendons, and bones during body movements such as walking. Blood flow imposes shear stresses to the vascular cells[9]. Blood pressure, by its pulsatile nature, imposes cyclic stretching via the expansion of blood vessels. Similarly, cardiomyocytes themselves undergo cyclic stretching due to pumping of the hearts[10]. The cells forming the lungs are also constantly subjected to a cocktail of mechanical forces caused by blood flow, surface tension, and the cyclic stretching induced by breathing[11]. There are countless other examples such as urine flow, sound waves, compression of dermal tissues upon touching, etc. In fact, through tissue matrix deformations and cytoskeleton-adhesion interfaces, most cells in vivo are stretched or compressed to a certain degree[12]. A key challenge is to understand how cells sense and respond to mechanical cues and conversely how they shape the physical properties of their microenvironment.

Cells can act as a bridge between the macroscopic world and molecular events. The forces discussed above can be sensed by the cells via conformational changes of proteins[3,13]. This can result, for instance, in the alteration of binding affinities or in the opening of membrane ion channels. This is how forces induced internally or by the microenvironment can activate a cascade

of signaling pathways, thus deeply changing the cellular biochemistry. The various mechanisms by which cells translate mechanical signals into biochemical signals are referred as mechanotransduction processes. In the early stages, research in mechanobiology was mostly concerned with sensory cells, as they are prominent manifestations of mechanotransduction. A classic example is the hair cells of the cochlea located in the inner ear[14]. Sound waves are mechanically converted into fluid motions within the cochlea, which deflect the sensory organelles stereocilia with respect to one another. This relative motion causes tension in the protein bridges between the stereocilia tips. This load pulls open mechanically-gated channels to induce ion flux and trigger downstream signaling.

Mechanobiology has later evolved to explore many different cellular functions and transduction mechanisms that are important for both non-specialized and specialized cells. For instance, morphogenesis in embryos is greatly impacted by external mechanical cues[15]. High-shear flow patterns were shown to play a critical role in various stages of developing zebrafish hearts[16]. Flow pattern perturbations can result in the formation of defective valves or an abnormal third chamber, sharing strong similarities with congenital cardiac diseases in humans. Also, stem cells specialize for different functions through differentiation processes which are affected by the stiffness, topology, and strain of the ECM[17–19]. There are countless examples in mature organisms as well. To name a few, increased load resulting from exercise lead to cardiac and skeletal muscle cell hypertrophy, while decreased load can lead to atrophy[20,21]. The signaling pathways regulating load-induced muscle development are not fully understood, but growth factors and protein complexes activating protein translation are believed to be involved[20,22]. Also, vascular smooth muscle cells forming blood vessels undergo remodeling under altered shear stress and stretching conditions[23]. Finally, another example is the bone and cartilage remodeling (and repair) upon changes in mechanical load[24]. More generally, mechanical stimuli play a fundamental role at the cellular level in regulating protein synthesis, cell death, secretion, proliferation, migration, and much more[7,25,26].

Being essential in a multitude of cellular functions and in maintaining tissue homeostasis, it is not surprising that the etiology of many diseases results from defects in mechanotransduction processes[4,5]. Changes in the ECM mechanics, cellular structure and organization, or deregulation of the sensing/transducing molecular mechanisms can be the sources of many abnormalities. A very small sample of diseases that involve deficient mechanotransduction is: hypertension, heart

failure, osteoarthritis, osteoporosis, diabetic nephropathy, glaucoma, asthma, pulmonary fibrosis, kidney disease, metastasis, and cancer. Despite increasing efforts in integrating mechanical considerations in biological and medical research, much remains to be uncovered, in particular in understanding the underlying mechanisms. Continuing to explore these avenues to find the molecules mediating mechanotransduction can prove to be pivotal in developing new therapeutic approaches. Bone pathologies, in particular osteoporosis, are a prime case[6]. For instance, the decreased bone mass and increased fragility which characterize disuse osteoporosis are associated with changes in mechanotransduction signaling caused by a reduction of mechanical stress. In particular, sclerostin was identified as an inhibitor of bone development which expression is regulated by mechanical loading. Promisingly, bone loss was prevented in mice models using antibodies against sclerostin[27].

Many technical challenges are encountered in in vitro mechanobiology studies: i) micromanipulation of molecules, cells, or tissues; ii) mechanical properties measurements of tiny dynamic objects; iii) precise application of diverse mechanical cues on specific cell structures; iv) creation of cellular microenvironments which are increasingly complex and physiologically relevant, exhibiting for example substrate stiffness gradient or heterogeneous topologies. A powerful way to study forces at the cellular level is to shrink down the laboratory to their scale. This is the approach of microfluidics, a field in which integrated systems are miniaturized with the aim of manipulating small amounts of fluid and what they host[28]. Indeed, numerous successful cell mechanics studies have exploited the multiple advantages of microfluidics[25,29]. These advantages include the ability to tailor the microenvironment to closely mimic in vivo conditions, integrate multiple stimuli, parallelize experiments (thus multiplying throughput), and minimize reagent quantities (hence lowering costs). On the other hand, one of the challenges of employing microfluidics for performing mechanobiology research resides in its novelty. It results in the constant need for developing novel platforms with improved capabilities, since the array of tools available is still under construction.

One of the key approaches adopted for understanding the effect of ECM forces on cell behavior is to deform the substrate on which they are cultured. When applied cyclically, as it often occurs in vivo, these substrate strains have been shown to activate multiple intracellular signaling pathways, leading to various responses[8,30–33]. In the context of 2D stretchable membranes, previous studies have largely focused on simple, uniform strain fields[30,34–40]. Although there is an

increasing effort to integrate stress conditions that mimic in vivo complexity*, little is known about the effect of non-uniformity in strain direction and amplitude[41–43]. The objective of this thesis is to advance experimental techniques and assess the cellular responses to biologically relevant complex strain fields. This was achieved by i) developing efficient microfluidic platforms generating non-uniform strain patterns; ii) thoroughly characterizing its primary effects on cellular reorganization in a model system; iii) assessing the time evolution of the cellular responses and exploring the impact of temporal discontinuities; iv) studying a cancer cell model in such non-uniform strains. A brief outline of the thesis is now presented.

Chapter 1. The objective of this introductory chapter is to expose key concepts and background information that are relevant to the technological achievements and biophysical studies presented in this thesis. First, various elements of mechanobiology are briefly covered. Second, fluid mechanics at the microscale, strain fields formalism, and high-resolution optical microscopy are discussed.

Chapter 2. A multitude of macroscale stretching devices and several microdevices have been developed previously to study the cellular response to strain. However, significant efforts were needed to achieve a platform tailored to answer the biological questions addressed in this thesis. General requirements include: i) encompassing a microenvironment suitable for cell culture, ii) reconstituting the complexity of in vivo ECM forces, and iii) enabling high resolution imaging. We hypothesized that a pneumatic-based microfluidic system could fulfill these requirements. The objective of Chapter 2 is the elaboration (design, fabrication, and characterization) of such system. Specifically, the platform we developed offers independent biaxial control and can generate strain fields with biologically relevant strain gradients while

*Previous studies have indicated that different aspects of complex stress conditions can have specific effects on the cellular response. For example, uniaxial compression of 3D gels leads to up-regulation of proteoglycan synthesis in chondrocytes[272]. Interestingly, up-regulation of the collagen synthesis only occurs when shear stress is superimposed to the uniaxial compression pattern. This study suggests that cells can operate uncoupled mechanoresponses that depend on the type of applied mechanical stress.

retaining moderate strain amplitudes. The capabilities and characterization of this microstretcher were presented in an article published in Biotechnology Letters[44] in 2014, on which Chapter 2 is partially based.

Chapter 3. A large body of studies have previously demonstrated that cells sense substrate deformations and exhibit a strain avoidance response. However, it was largely unknown prior to this work whether cells have the ability to sense and respond to strain gradients, to which cells composing our body are largely exposed. We hypothesized that they do, in analogy to their known ability to sense stiffness and chemical gradients. The objective of Chapter 3 is to investigate strain gradients as potent mechanical cues influencing cells' fate. Our stretching platform allowed a comprehensive analysis of the cellular reorientation responses under a non-uniform strain field. Cellular strain gradient avoidance was demonstrated for the first time, which shows that cells possess the required mechanosensing machinery to sense and localize subtle changes in strain amplitudes. The investigation of key cellular structures involved in this process provides insights into how strain gradients shape the long-range organization in population of cells. This manuscript was published in *Integrative Biology* in 2017[45].

Chapter 4. The results presented in Chapters 2 and 3 raised new questions which lead us to push the analysis and the strain pattern complexity one step further. Not only are cells in our body exposed to non-uniform strain fields, but the conditions can also change over time (daily activities, embryo development, injury, etc). The cells' ability to adapt to multiple changes in stretching direction had been little explored previously, let alone in a non-uniform strain field. The objective of Chapter 4 is to determine if cells can reorient a large number of times and thoroughly characterize the evolution of their responses. We hypothesized that the cellular response to a changing strain pattern is fully consistent. Five reorientations were successfully achieved, but subtle differences were observed from one cellular reorientation to the next. The evolution of the cellular response uncovered the interplay of two different mechanical cues, which we demonstrated occur on different time scales. This provides new insights on the strain mechanoresponse process. This manuscript is submitted to *Integrative Biology*. Chapter 4 also includes additional details on the device design modifications which were required to carry the work presented in Chapters 3 to 5.

Chapter 5. Here we put our new platform at work to study non-healthy cells. The majority of cancers are believed to originate from epithelial cells[46]. The capacity of normal epithelial cells to eliminate newly transformed cells depends on the concerted action of various cytoskeletal proteins[47], the activity of which are known to be modulated by mechanical stimuli. Prior to this work, however, very little was known about the influence of strains on the mechanism of epithelial defense against cancer (EDAC). We hypothesized that strain-induced cellular remodeling affects the interaction of normal and transformed cells during the process of apical extrusion. The objective of this chapter is to characterize the impact of substrate strain on the early stage of cancer development in epithelial tissues. This work showed that external forces greatly promote invasive behaviors of Ras^{V12}-transformed cells and jeopardize their apical extrusion. Gaining insights on cancer spreading from such novel perspective could pave the way toward new therapeutic approaches. The manuscript presented in Chapter 5 is in preparation.

1.1 ELEMENTS OF MECHANOBIOLOGY

Various concepts of mechanobiology relevant to the studies presented in Chapters 3-5 are now discussed. After introducing the general interactions between the cell and the ECM, major members of the cellular mechano-machinery are presented. Key aspects of the mechano-sensing, -transduction, and -response associated with cyclic substrate stretching are then discussed. Finally, the importance of forces in both healthy epithelia and in the presence of transformed cells are addressed, setting the stage for Chapter 5.

1.1.1 THE CELL AND ITS MICROENVIRONEMENT

The ECM provides support to adherent cells and helps maintaining tissue shapes by opposing resistance to external forces. Beyond the structural role that it fulfills, the ECM gives instructions to cells in the form of physical signals[2]. Not only do the cells sense these external cues, but they also continuously respond to them by actively adapting their biophysical properties and by remodeling the microenvironement. Through this loop, the ECM shapes cells, and cells shape the ECM. This mechanical equilibrium is imperative for good health. Numerous fundamental cell functions are orchestrated via the mechanical reciprocity existing between the physical properties of a cell and those of its microenvironement.

Cells exert forces on their surroundings to execute many function such as migration, sensing, cell-cell communication, maintenance of tissue functions and integrity, tissue

remodeling, wound healing, and embryo growth/development[5,48–51]. To preserve or achieve the optimal ECM-cell mechanical homeostasis, cells employ feedback mechanisms designed to restore or change the ECM mechanical properties when required[2]. To this end, for example, cells forming soft connective tissues are believed to employ various mechanisms. These include controlling the rates of ECM synthesis and degradation, the type of ECM constituents synthesized, and the degree of pre-stress incorporated in the ECM constituents[52–54].

For instance, if a decrease in ECM stiffness is detected, pathways that engender ECM stiffening are normally activated. A rapid way for cells in vivo to fine-tune the ECM stiffness is to modulate the forces exerted on it, since many biological materials are strain-stiffening (e.g. collagen)[55]. For example, soft connective tissues exhibit a near-linear stress-stiffness behavior resulting from a near-exponential stress-strain relationship[2]. Alternatively, to avoid having to actively maintain such tension onto the ECM, cells can rather organize newly synthesized or pre-existing ECM constituents in such way as to introduce built-in tension within the ECM. The type of constituents that are deposited, their density, their orientation, and their degree of crosslinking can also change the structural integrity and stiffness of the tissue[2].

Conversely, the surrounding mechanical information guide a large array of physiological processes such as cell growth, mobility, differentiation, proliferation, and gene expression[56,57]. Hence, gaining insight on the mechanisms by which cells sense and transduce mechanical signals is necessary to better understand the molecular pathways leading to numerous cellular processes and diseases. Before exploring how substrate strains are transmitted, sensed and transduced, the cellular machinery involved in force processing is briefly examined in the next section.

1.1.2 CELLULAR MECHANO-MACHINERY

Various cellular components are involved in the mediation of the ECM sensing and its associated cellular responses. The main components include adhesion receptors that bind the ECM, cytoskeletal networks with their related motor proteins, and other intracellular cytoskeletal and focal adhesion signaling proteins[58].

Focal adhesions. The primary link joining the ECM proteins to the actin cytoskeleton are macromolecules assemblies called focal adhesions (FAs). They contain heterodimer integrins (α and β subunits) that are transmembrane receptors directly binding the ECM[1]. Integrins are also

connected to the intracellular portion of the FAs, which consists in various proteins, many of which are crucial mechanosensors[59]. The capacity of FAs to sense and transmit forces to the cytoskeleton was first shown by directly applying twisting forces on their adhesion receptors via magnetic beads[60]. The magnitude of the applied stress was directly correlated with an increased in cytoskeleton stiffness.

Cytoskeleton. The cytoskeleton consists in an interconnected network of filaments formed by polymers and associated with signaling proteins[61]. Many functions are carried out by the cytoskeleton, in particular the organization of intracellular components, the generation of coordinated forces, and the tuning of the cell's mechanical properties[1]. The cytoskeleton also participates to bridging the cell to the external environment, connecting their physical and chemical events. Far from being a fixed structure, the cytoskeleton is constantly remodeling by self-assembling and -disassembling, using a variety of proteins as building blocks[62]. The specific architecture of its network mediates critical cellular functions and therefore it is determined by the cell's changing needs. A multitude of regulatory proteins control the cytoskeleton structure by initiating and terminating filament growth, promoting faster growth or disassembly rate, and arranging filaments to form highly organized and reinforced networks. Both extracellular and intracellular mechanical forces influence these regulatory proteins, thus impacting cytoskeletal activity and ultimately cellular functions.

Concerted action of the focal adhesions and the cytoskeleton. Cells probe the physical properties of the microenvironment via contractile forces generated by the actin cytoskeleton and transmitted via adhesions[63]. In response to the physical properties they probe, cells have the ability to remodel their FAs and cytoskeleton, tuning for instance their own contractility and stiffness[64]. For example, in vitro cells cultured on rigid substrates apply increased tension (by adjusting their cytoskeleton) in comparison with cells grown on a compliant surface[65,66]. Traction force microscopy allows to study such interactions by tracking the displacements of beads (or other markers) that are embedded into an elastic hydrogel substrate[67]. As another example, when a cell is subjected to uniaxial cyclic substrate strain, its FAs sense and transmit this mechanical stimulus. As a response, its body usually aligns along the direction of minimum strain[30,34–41,44,68]. This strain-induced cellular reorientation requires major cytoskeleton remodeling in order for the cell to reach a stable mechanical equilibrium. The three types of cytoskeletal protein filaments

found in mammalians cells are believed to have mechanical roles in this phenomenon[1]. They are the actin filaments (F-actin), the microtubules (MTs), and the intermediate filaments (IFs).

Intermediate filaments. While F-actin and MTs are composed of polarized global subunits, IFs are rather formed by neutral α-helical chains[8]. Their structural and functional integrity are relatively stable because of their assembly and disassembly mechanisms. IFs play a protective role against external forces and regulate numerous signaling events related to cellular growth, architecture organization, migration, and much more[69]. A recent study demonstrated the implication of IFs in the cellular response to external force in the context of mesendoderm cells migration[70]. Polarized cell protrusions and cell migration were induced using magnetic beads to mimic intercellular forces. This led to the accumulation and reorganization of IFs at the sites of applied stress. Moreover, cellular responses under cyclic stretching, including alignment, elongation, and spreading were shown to be affected by the IFs' integrity in muscle cells[71]. The results of this study suggest that IFs are involved in the transduction of mechanical forces. Indeed, the IFs connect the nucleus to the cellular surface[72], making them potential actors in mechanotransduction.

Microtubules. Despite being the most rigid of the cytoskeletal filaments, MTs are highly dynamic structures. They are formed by alpha and beta subunits. The rapid polymerization and depolymerization at their free ends can generate pushing or pulling forces[45,73]. These properties allow MTs to execute critical duties such as establishing the cell shape, guiding cargo-carrying motor proteins, moving considerable intracellular structures like the nucleus or chromosomes, and constituting solid and stable anchor points to support and counterbalance the tugging of actin stress fibers during cell migration[74,75]. MTs may also be important players in the cellular reorientation under cyclic stretching. In particular, it was demonstrated in Airway smooth muscle cells that MTs must maintain an adequate strain onto the actin stress fiber to help balancing the external forces[76]. In this context, the concerted action of the MT and actin networks was believed to be central in re-establishing a homeostatic mechanical state in cells.

Actin. While the architecture of the MT network is regulated by a central organizing center, the specific configuration of the actin cytoskeleton is rather determined by the local signaling activity[77]. The F-actin composing the actin cytoskeleton consists in helical polymers (Fig. 1.1). The later are formed by globular actin molecules, which rapid turnover permits efficient

remodeling of the cytoskeleton[8]. This process is influenced by the presence of polymerization proteins such as profilin and formin[78]. The actin networks form complex structures with varying architectures via the concerted action of diverse actin-binding proteins such as α-actinin and fascin. The cooperation of these proteins gives the cytoskeleton unique characteristics such as enhanced stiffness[79]. Actin cytoskeleton networks generate different types of forces which are tailored to accomplish specific cellular functions[80]. Cell migration and division, as well as processes like endocytosis and trafficking, require the mechanical contribution of the actin cytoskeleton. For example, the protrusion formation during cellular migration uses actin polymerization as a mean to generate forces, the growing filaments pushing the plasma membrane forward [48,81]. One specific actin network acting as a major force generator, including in the context of cellular migration, is the actomyosin cytoskeleton[82]. Contractile forces are achieved by the translocation of actin microfilaments, driven by the coordinated activity of the motor proteins myosin II. Actin stress fibers (SFs) are bundles of actomyosin. Their adaptive property allows rapid changes in their configuration upon application of forces. As a relevant example, cellular cyclic stretching generally leads to a reinforcement of actin SFs[83] and to their gradual polarization perpendicular to the applied force[33]. In fact, SFs do not only produce forces, but they also sense them[8].

The next section presents an overview of the potential mechanisms involved in substrate strain sensing, transducing, and response.

1.1.3 MECHANOSENSING -TRANSDUCTION AND -RESPONSE TO CYCLIC SUBSTRATE STRAINS

Cellular mechanosensing relies on proteins whose conformations change in response to mechanical forces[84]. The modified protein activity triggers multiple intracellular signaling events, hence converting mechanical information into biochemical signals. This leads to alterations in cellular structure and/or function in response to forces and other physical parameters. Deformations of the ECM are transmitted to the whole cell via the ECM-FA-actin chain, allowing mechanotransduction processes to take place beyond the FA sites. For instance, substrate deformations are propagated to the cellular membrane and activate mechanosensitive ion channels, controlling the ion flux across the membrane[85]. Also, mechanical stress on the nucleoskeleton influences nuclear structure and function[86].

The origin of forces affecting cellular behaviors is not limited to the microenvironment. Cells can use mechanotransduction processes to self-regulate by generating forces via their

actomyosin cytoskeletons[84,87]. For instance, FAs are force-bearing structures and the application of tensile forces lead to their maturations[87]. Whether these forces come from the ECM or are generated internally by contractions, they induce FA growth by protein recruitments. This FA reinforcement is mediated by proteins such as talin, whose mechanoresponse activates integrin and promote vinculin binding to strengthen the FA complex.

The remaining of this section explains how substrate stretch can lead to cytoskeleton remodeling. Pulling forces on FAs induce conformational rearrangements which promote both the recruitment and the activation of many proteins. Substrate strains thus trigger a cascade of signaling events, including the activation of GEFs, which in turns activates RhoA (Fig. 1.1). Two RhoA downstream effectors that are key player in the strain-induced response are first presented. The activation of RhoA by GEFs is then discussed.

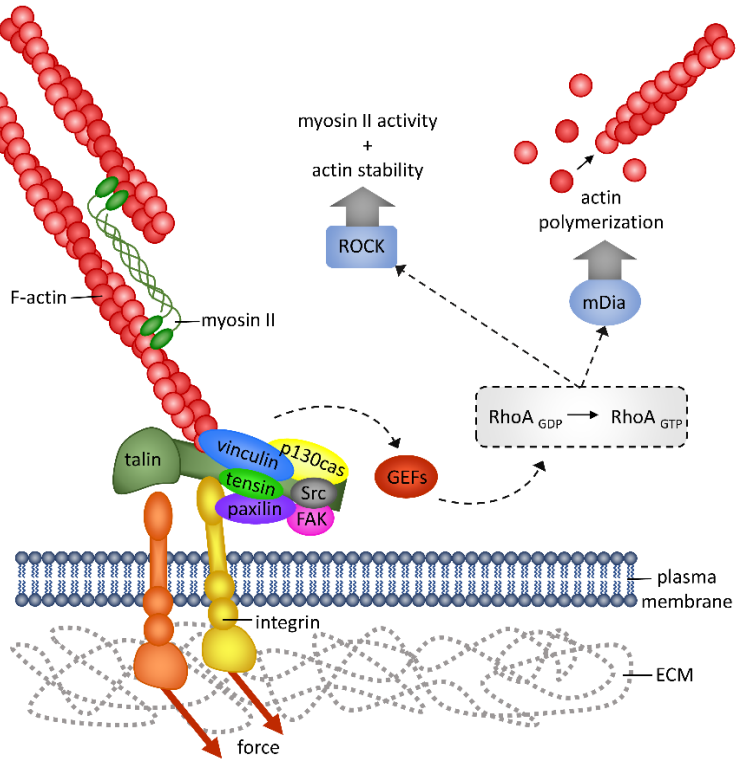

Figure 1.1 Regulation of the actomyosin cytoskeleton in response to cyclic stretching. The transmembrane proteins (integrins) bind the ECM and transmit the external force to the intracellular FA complexes. The actin cytoskeleton connects the integrins via anchoring proteins such as talin and tensin. Pulling forces on the FA complexes induce their maturation via vinculin recruitment. The resulting cascade of compositional changes include recruitment of proteins transducing tension into biochemical signals, among them FAK, Src, paxillin, and p130cas[87]. Many GEFs are activated via this tension-induced biochemical signaling. They target in particular RhoA,

Rac1 and/or Cdc42[30], which have different effects on actin. Among the numerous signaling pathways triggered by mechanical forces, many lead specifically to the activation of RhoA, which is responsible for much of the intracellular force generation[33]. GEFs catalyze the exchange of GDP for GTP to activate RhoA, which remodels the actomyosin cytoskeleton via two key downstream effectors, ROCK and mDia.

Role of RhoA and its downstream effectors in remodeling the cytoskeleton. Members of the subgroup Rho GTPases of the Ras superfamily have long been considered to be key players in various mechanotransduction processes[84,88]. Acting like switches, their states cycle from the inactive form GDP-bound to the active form GTP-bound. They constitute regulation mechanisms of various cellular functions since their active forms interact with numerous downstream effectors to trigger a myriad of signaling events. The cellular functions regulated by Rho GTPases cover a wide spectrum, from cell growth, to gene expression and membrane trafficking[88]. Activation of the family members RhoA, Rac1, and Cdc42 in response to mechanical forces can lead to important cellular adhesion and actin cytoskeleton reorganizations[89]. RhoA, one of the main regulators of intracellular force production, has two major downstream effectors: Rho kinase (ROCK) and mDia[90,91]. These effectors influence the actomyosin cytoskeleton architecture in many ways. ROCK promotes myosin II activity by increasing phosphorylation of the myosin light chain (MLC), and stabilizes the F-actin network by indirectly inhibiting the actin severing-protein cofilin. When stimulated by RhoA, the formin mDia promotes the formation of actin filament via actin polymerization[90].

Tension-induced activation of GEFs targeting RhoA. Guanine nucleotide-exchange factors (GEFs) and GTPases-activation proteins (GAPs) govern the RhoA GTP/GDP switch with their respective activation and inactivation roles[33]. Many of these proteins are associated to the cytoskeleton and adhesion complexes, suggesting their potential role in mechanotransduction. Guilluy *et al.* showed that two GEFs (GEF-H1 and LARG) were recruited in the vicinity of the cell-ECM adhesion complexes following the application of mechanical forces on integrins using fibronectin-coated beads[92]. The activation of RhoA by cyclic stretching can result from the recruitment of numerous GEFs, such as GEF-H1[31], Vav2 [32], and Solo[30]. Various pathways can activate the different GEFs in response to external forces on integrins. For example, LARG is activated by tyrosine kinase Fyn (Src family) while the FAK/Ras/ERK signaling pathway stimulates GEF-H1 activity[92]. We also note that in high-density population of cells, cyclic deformations of the substrate can result in tension on both ECM-cell and cell-cell adhesions. In cyclically stretched

endothelial cells, it was suggested that RhoA activation mediated by Solo operates at the cell-cell (cadherins) adhesion sites[30].

The mechanisms discussed above explain the strain-induced actomyosin remodeling and reinforcement. Nevertheless, they do not explain why cells subjected to cyclic stretching reorient their body, SFs, and FAs approximately perpendicular to the stretching direction[30,34–39,44,68]. An overview of the existing models developed to describe this reorientation response is given in Chapter 3, mainly in section 3.4.1.

1.1.4 CELLULAR FORCES ARE REQUIRED TO INSURE VITAL EPITHELIUM FUNCTIONS

Epithelial cells form thin layers covering the surfaces of our body, from cavities such as the lungs, stomach, and intestines, to other vital organs such as the kidneys, liver, and pancreas. The integrity of these tissues is critical due to the protective functions they insured, especially for preventing the passage of cells, pathogens and certain macromolecules[93]. Their selective permeability allows the adequate transport between compartments. Dying epithelial cells are quickly expulsed and replaced via mitosis to maintain the optimal cell density and avoid epithelium gaps [94,95]. When the epithelium density is too high, exceeding cells are removed from the tissue by a process called apical extrusion (Fig. 1.2). This process also allows to eliminate dying or abnormal cells by expulsing them away from the organ, resulting in their rapid death. A defect in these processes can result in altered barrier properties, potentially leading to organ damage and other types of pathologies such as intestinal diseases[93].

The molecular signal sphingosine-1-phosphate (S1P) has been reported to be secreted by dying cells[95]. When the bioactive signal SP1 is released into the extracellular environment, it binds to the S1P2 receptors of the adjacent healthy cells. This process activates the small GTPase Rho, which promotes the actomyosin cytoskeleton development at the circumference of the adjacent cells to form a strong contractile belt[94,96]. This cytoskeleton remodeling leads to the generation of concerted forces, squeezing out the dying (or abnormal) cell[46]. Thereby, a biological signal secreted by a dying cell was shown to trigger the production of contractile forces in neighboring cells, as required to drive its extrusion.

The following question then emerges: does a dying cell contribute mechanically to its own extrusion? A recent study has demonstrated that tension first emerges from the F-actin and

myosin rings of the dying cell itself; only later does the mechanical participation of the neighbors arise[97]. The extruding cell thus has an active physical contribution in the process of cell removal. The cortical contractile apparatuses of cells are mechanically coupled via cadherin-based cell-cell adhesions. Interestingly, these adhesion complexes are constantly transmitting and integrating tension across neighboring cells[98]. This rises another important question: can the initial contractile force generated by the dying cell constitute a triggering cue in itself? Epithelial monolayers can generate complex patterns of contractile tension throughout their junctions. The cortical contractile cytoskeleton, in cooperation with the adhesion complexes, influence the local landscape of cellular junctional tension[99]. The later has been recently proposed as a potential cell sorting mechanism, determining if a cell is to remain in a population or not[100,101].

1.1.5 CANCER DEVELOPMENT IN EPITHELIA

The development of cancer is a complex multistep process involving the cooperation of numerous genetic mutations. Inactivation of tumor gene suppressors combined to the alteration of proto-oncogenes that become active regardless of the microenvironment, confer special abilities to a transformed cell[102]. These cancer hallmarks are: i) sustained proliferation signals, ii) insensitivity to growth suppressors, iii) cell death resistivity, iv) controlled angiogenesis (to increase blood supply), v) unlimited replication, and vi) invasion and metastasis potential[103]. Other emerging hallmarks include vii) the ability to bypass immunological destruction and viii) the modification of the cellular metabolism to better support proliferation.

Cancer progression is increasingly viewed as a journey marked not only by genetic alterations, but also by important changes in cell and tissue architecture and mechanics[104]. In addition to biological and functional modifications, the cell's physical properties are deeply altered due to significant reorganizations of their cytoskeleton. When a tumor cell extracts itself from a primary tumor to invade a secondary site, it must undergo constant cytoskeleton remodeling to achieve the mechanical properties driving metastasis behavior. Constantly applying mechanical forces to their surroundings, tumor cells generate for instance traction forces for their locomotion and protrusion forces at their leading edge. Also, since it is believed that cancerous cell's softness correlates with invasive potential[105], it is not surprising that some cancerous epithelial cells have been shown to be softer than their healthy counterparts [106,107].

As discussed previously, a rapidly growing body of work shows that cells utilize multiple strategies to sense mechanical signals and transduce them into biochemical signals. One exciting challenge now is to understand the role of mechanotransduction in the cell's oncogenic activity. Promising studies are starting to show how physical cues are potential tumor growth regulators[65]. Breast cancer progression is promoted by ECM stiffening, where the latter is attributed to the deposition of collagenous components by activated stromal myofibroblast[108]. Also, sustain mechanical compressive stress enhances coordinated migration of cancer cells via the formation of leader cells[109]. Finally, interstitial fluid pressure in tumor produce mechanical forces that are believed to act as positive regulator of cancer cell proliferation[110].

The majority of cancers begin with the transformation of a single cell in epithelia following gene mutations[111]. Studies using Madin-Darby canine kidney (MDCK) epithelial cells with constitutively active oncogenic Ras^{V12} have shown a dependence of the transformed cell's fate on its interaction with neighboring normal cells[47]. When surrounded by normal cells, a Ras^{V12}-transformed cell is either extruded from the epithelial sheet or grows invasive protrusions. In the majority of the cases, cells are extruded apically in a process involving the formation of cytoskeletal contractile rings. This is known as the epithelial defense against cancer (EDAC)[112]. The Ras proteins impact many signaling pathways, including Rho[113,114], which most likely actively participate to the cytoskeleton remodeling of the transformed cell. Oncogenic extrusion can be driven by changes in the tension pattern at the cell-cell junctions[100,101]. Cell-cell junctional patterns of forces are significantly determined by the cortical F-actin networks. It is thus of prime interest to investigate cues from the microenvironment that have the potential of influencing the F-actin networks, such as mechanical strains. Finally, defects in the extrusion process that can change the direction of extrusion (from apical to basal) are believed to favorize the transformed cell survival and to promote its invasiveness potential[115] (see Fig. 1.2).

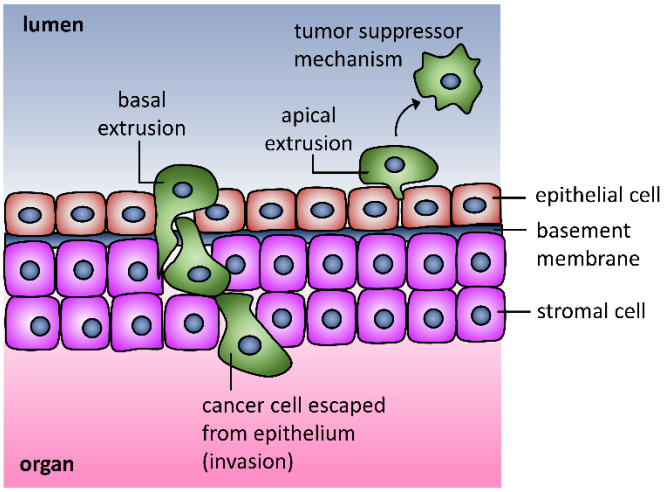

Figure 1.2 Basal vs apical cell extrusion. Cells are typically extruded apically into the lumen by contraction of actomyosin networks. Once fully detached, the cells usually die, deprived from the survival signals of the matrix. Apical extrusion of transformed cells is believed to represent a defense mechanism against cancer. However, because of their upregulated survival signals, tumor cells can be extruded from the epithelium in a death-independent manner. Also, some mutations in tumor cells can redirect their extrusion basally (toward the organ), which may constitute an oncogenic mechanism to initiate invasion. Adapted from[115].

1.2 ELEMENTS OF MICROFLUIDIC PHYSICS AND MICROSTRETCHERS

The miniaturization of fluidic systems allows precise manipulation of nano- and microliters of solutions as well as small objects. Microfluidic platforms find applications in a vast array of fields including proteomics, forensics, clinical treatments, molecular diagnostics, DNA manipulations, organ-on-a-chip research, etc[28]. The study of the cellular responses to complex substrate strain fields can also be advantageously performed in microfluidic-based stretchers, for reasons that will be evidenced throughout this work. Concurrently, additional considerations and challenges also result from scaling down the cell stretching device and using microfluidic channels for various operations (membrane functionalization, cell loading, culture media exchange, drug addition, fluorescence staining procedures, etc). In this section, elements of microfluidic physics are presented briefly to assess in particular the importance of fluid shear stress, since it can perturb cellular behaviors[116]. A special attention must be paid to such external microenvironment factor if the effect of strain fields is to be properly interpreted. This section also includes physical and chemical specificities of the cell substrate and the overall culture environment. Finally, an introduction to strain formalism is presented to set the ground for Chapters 2 and 4, where the microstretchers are described in details.

1.2.1 FLUID DYNAMICS IN MICRODEVICES

Even on the scale of microdevices, fluid dynamics is typically described using the macroscopic approach of modelling matter as a continuum material. In fluid dynamics, one is generally concerned with finding the velocity field $\vec{u}$ characterizing the flow under study, given boundary conditions. The general strategy is to determine the forces acting on a small fluid element and apply momentum conservation and mass continuity equations. The continuity equation simply states that the change in mass within a control volume is equal to the net flux of mass across its surfaces. For an incompressible flow, which is a good approximation for the fluids used in our work, the density ρ is constant and the continuity equation can be written as[117]:

$$\nabla \cdot \vec{u} = 0 \tag{1}$$

Fluid motion is governed by the Navier-Stokes equations, which is essentially the continuum version of Newton's second law expressed per unit volume. For an incompressible Newtonian fluid with uniform viscosity η, when body forces (Coulomb and gravitational forces) are negligible, the equation can be written as:

$$\rho \frac{\partial \vec{u}}{\partial t} + \rho \vec{u} \cdot \nabla \vec{u} = \eta \nabla^2 \vec{u} - \nabla \mathrm{p} \tag{2}$$

where p is the pressure. The left-hand side corresponds to the acceleration terms and the right-hand side to the sum of forces. More specifically, the first left term is the temporal change in momentum in a given fixed control volume. In contrast, the second term represents the acceleration (multiplied by the density) of a fluid element that results from its change in position in the velocity field. In other words, it is the net momentum convected out of (or in) the control volume. The force terms on the right arise from the stress on the surface of the control volume. There are two contributions: the viscous force and the pressure force (both per unit volume), respectively. The specific form of the viscous force in equation (2) results from the linear relationship between the viscous stress and the strain rate (essentially a measure of the velocity gradient) assumed in Newtonian fluids.

In general, the Navier-Stokes equations must be solved numerically, mainly because of the non-linear convective acceleration term $\vec{u} \cdot \nabla \vec{u}$. Analytical solutions exist for simplified geometries, for example when the fluid velocity and the velocity gradient are orthogonal, in which case the non-linear term vanishes. This is essentially the case in long microchannels having a uniform cross-section. In fact, the convective acceleration term can often be neglected in

microfluidics, independently of the channel geometry, since it is typically negligible compared to the viscous forces. The Reynolds number (Re) captures the relative importance of these two terms; it corresponds to the ratio of inertial forces to viscous forces:

$$Re = \frac{\rho U l}{\eta} \tag{3}$$

where U is the characteristic velocity, and l the characteristic length scale. In microfluidic systems, Re is often $\ll 1$, leading to linear flows[28]. Low Re numbers result in laminar flows, which are smooth and stable to perturbations, as opposed to transitional or turbulent flows. For typical flow velocities ($U_{channel} \sim 10^1$ mm/s and $U_{cell\ chamber} \sim 10^0$ mm/s) and considering the device geometry used in our work (Fig. 1.3c,d and Fig. 2.1), the Re is on the order of 10^0, ensuring laminar flows.

1.2.2 FLOW PROFILES AND BOUNDARY CONDITIONS

It is informative to consider the velocity profile of a pressure-driven flow in a circular microchannel. This is known as the steady Hagen-Poiseuille flow[118]. The unsteady term of equation (2) vanishes, as well as the convective acceleration term due to geometry considerations. The Navier-Stokes equation can be solved by direct integration. There are two boundary conditions: i) the velocity in the center of the channel must be finite; ii) the velocity of the fluid in contact with the wall is zero. This is the no-slip condition, consistent to a large degree with observations in most microfluidic systems[117]. The Hagen-Poiseuille flow equation for a channel of radius R and oriented along the z-axis is:

$$u_z(r) = -\frac{1}{4\eta}\frac{\partial p}{\partial z}(R^2 - r^2) \tag{4}$$

where u_z is the axial velocity as a function of the radial position r. The simulated velocity profile is shown in Fig 1.3a. Channels are usually rectangular in lithography-based microfluidic devices. The velocity profile for a pressure-driven flow in such channel geometry is qualitatively similar, as shown in Fig. 1.3b. In the microstretchers that we developed (Fig. 2.1), the cross-section area of the cell chamber at its maximum width is ~10 times larger than that of the loading microchannels. Considering incompressible flows, the velocity is correspondingly smaller in the cell chamber (Fig. 1.3c). Importantly, the cell chamber can be viewed roughly as a local enlargement of the rectangular microchannel. Although this geometry results in a non-vanishing convective acceleration, the cross-sectional velocity profile can be expected to remain qualitatively similar to

the Hagen-Poiseuille flow since the flow remains laminar and its profile is determined largely by the no-slip condition (Fig. 1.3d).

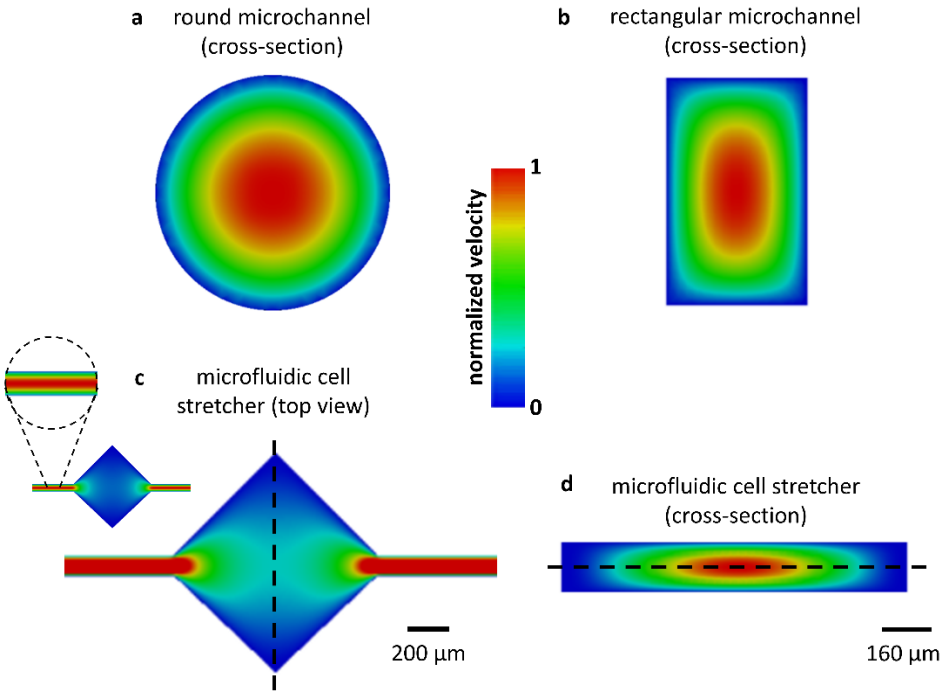

Figure 1.3 Velocity profiles of pressure-driven flows. The profiles are simulated in SimScale, for different channel geometries (laminar flows and no-slip conditions at the walls were assumed). The scale of the lower left image was saturated to increase the visibility of the flow profile within the diamond-shaped cell chamber; the corresponding inset shows the unsaturated scale. Note that each flow profile has been normalized independently. SimScale information: Mesh: hex-dominant and moderate fineness; Simulation: incompressible, laminar, and steady-state; Boundary conditions: no-slip at the surface of walls, fixed inlet velocity, and fixed outlet pressure.

1.2.3 SHEAR STRESS ON CELLS

For a Newtonian fluid, the viscous stress associated with a cylindrically symmetric unidirectional flow $u_z(r)$ is given by[117]:

$$\tau_{zr} = \eta \frac{\partial u_z}{\partial r} \tag{5}$$

Using equations (4), the shear stress on adhered cells (at r=R) that results from a pressure-driven flow in a cylindrical microchannel is thus:

$$\tau_{zr} = \frac{4\eta Q}{\pi R^3} \tag{6}$$

where Q is the volumetric flow rate (product of cross-section and mean velocity). This equation is very similar (within a factor 2) to that of a rectangular channel of equal cross-section[119] and therefore can be used to estimate the shear stress in our microstretchers.

Depending on the experimental protocol used, fluid flow in our microstretchers can occur during cell seeding, culture medium exchange, drug addition, and fluorescence staining. The flow velocity employed during these processes are somewhat of a compromise between minimizing the shear stress exerted on the cells and completing the operation in a reasonable time. It can be inferred from Fig 1.3c that the shear stress in the cell chamber is maximum in the regions immediately adjacent to the input and output channels. In contrast, the shear stress is minimum (near-vanishing) in the opposite corners of the cell chamber. Considering a maximum flow rate of approximately 10^{-1} mm^3/s, the shear stress is varying between ~0 and ~10^{-1} Pa (never above 1 Pa during our experiments). How significant is this? Interstitial flow occurring in vivo is known to modulate critical cellular functions such as gene expression, migration, morphology, proliferation, intracellular signaling events, protein secretion, etc[116,120,121]. Effects on cell behaviors were observed with magnitudes ranging from ~10^{-3} - 10^{2} Pa, over a few minutes to many days. Importantly, the direction of laminar fluid flow has been shown to guide the orientation of the cell body and the direction of their intercellular stress. Fluid shear stress on the order of 1 Pa applied to endothelial cell activate integrins (within a few minutes) and induces cell body and cytoskeleton alignment (after several hours) in a Rho-dependent manner[122,123]. Although minimizing fluid flow is advantageous in the context of our studies, it had negligible effects in our case since fluid flow was limited to a few minutes during an experiment (many hours) and it was under 0.1 Pa over most of the cell chamber. Moreover, the open-top capabilities (see Chapter 2, section 2.6) were typically employed for critical processes such as fixing and staining to prevent bias. Finally, we evaluated the maximum fluid shear stress caused by the motion of the vacuum cavities to be on the order of 10^{-4} Pa.

1.2.4 DIFFUSION AND MIXING

The velocity profiles within the external input tube, the device microchannel, and the cell chamber of our devices are non-uniform. This raises the question of how practical it is to expose all cells across the membrane to drugs or immune-fluorescence staining solutions. When a new solution is inserted in the input tube, its front (i.e. the interface of the two fluids) progresses forward non-

uniformly according to the Poiseuille flow profile. In absence of diffusion, this would result in a parabolic front stretching indefinitely. Similarly, given the laminarity of the flow and its Poiseuille profile, a fluid element going through the center of the cell chamber has previously travelled approximately through the center of the input tube. Likewise, a fluid element passing within a few microns of the cell chamber's membrane has previously travelled within a few microns of the walls in the input external tube and in the device microchannel. We can consider the flow profiles shown in Fig 1.3c to estimate the time required for a fluid element to travel from the entrance of the external tube to the downstream end the cell chamber. Limiting the average velocity in the microchannel to ~ 10^1 mm/s and considering a typical external tube length of ~ 10^2 mm, we can calculate such travel time. It varies between ~ 10^1 s for elements in the center of the flow profile and $\gg 10^2$ s for elements in the vicinity of the solid interfaces. Flushing times of several minutes are thus required. But even then, one may wonder if the full cell chamber membrane can ever be in contact with new solutions, given the no-slip condition? First, the no-slip condition is an approximation; in reality, the tangential velocity is not necessarily zero at the wall, depending on the surface chemistry[28,124]. Second, diffusion smears out the interface between two solutions. This results from Brownian motion. The characteristic time τ_{diff} required for a solute to diffuse across a length l_{diff} is on the order of[117]:

$$\tau_{diff} = \frac{{l_{diff}}^2}{D} \tag{7}$$

where D is the diffusivity. For a spheroidal particle in a viscous fluid, the diffusivity can be approximated by the Stokes-Einstein relation:

$$D = \frac{k_B T}{6\pi\eta a} \tag{8}$$

where k_B is the Boltzmann's constant, T is the temperature, and a is the particle radius. The larger the particule, the lower the diffusivity and the longer the diffusive time. In the studies presented in Chapters 3 to 5, the molecular sizes of the drugs and immunofluorescence stains employed were typically on the order of 1 nm diameter (or less), leading to a diffusivity on the order of 10^3 μm^2/s. The time required to diffuse across a few microns is thus $\ll$ 1 s (and it is ~10^1 s over a characteristic length of 100 μm). Consequently, a few minutes after the introduction of a new solution, all areas of the cell chamber's membrane will indeed be exposed.

The challenge of mixing solutions in microfluidic devices, in which flows are essentially always laminar, is addressed extensively in literature[28]. In our case however, as shown above, it was not necessary to implement mixing-specific elements in our design considering that our experimental conditions typically involved exposure times well above the characteristic diffusion times.

1.2.5 MICRODEVICES AS CELL HOSTS

Cell culture in microdevices is becoming more prevalent with the increasing popularity of microfluidics as biological exploration tools. They are particularly useful to precisely deliver physical cues (e.g. fluid flow, ECM topography and stiffness) and chemical cues (e.g. drug and growth factors). Importantly, they also allow to probe the associated cellular responses. Polydimethylsiloxane (PDMS) is a widely used material to this end since it offers many advantages such as biocompatibility, optical transparency down to 230 nm, low autofluorescence, and elasticity[125]. Importantly, this silicone based organic polymer permits the fabrication of various microstructures integrated into multiple layers, increasing the versatility in design and operating functions[126]. For cell culture applications, its permeability to gases facilitates the maintenance of adequate culture medium pH, while its impermeability to water allows fluid manipulation. Cell cultures generally require maintaining the microdevices at the physiological temperature of 37^{o}C, hence evaporation has to be minimized to avoid changes in cell medium concentration. This can be achieved by ensuring that the ambient gas has a humidity level sufficiently high. All-PDMS platforms also have downsides for biological applications that must be carefully considered[127]. First, hydrophobic molecules from the serum contained in the media can be absorbed into PDMS, thus decreasing the concentration of certain growth factors. Using high volume of media, as we did in Chapters 3-5, minimize this effect. Second, uncured oligomers from the polymer may interact with the cellular membranes. Special care was taken when mixing and curing PDMS to minimize their presence.

As mention in section 1.2.3, if the effect of shear stress is not a parameter under study, special care is required to minimize it since physiological shear stress amplitudes are easily reached in microfluidics. Others physical parameters to consider when designing a microdevice for cell culture are the substrate stiffness and the platform topography/confinement. For example, mesenchymal stem cells specify their lineage and phenotypes directly according to the

ECM stiffness[17]. Also, a single geometric degree of confinement was shown to drive the formation of spherical cell mass (embryogenesis) in embryonic stem cells[128]. Finally, the biochemical composition of the substrate should also be taken into consideration since it is the primary physical link between the cell's integrins and the microenvironment. The ECM composition in vivo is known as one of the most important cellular regulators[129]. For example, changes in biochemical ECM composition can lead to loss of polarity in epithelia, which in turn can increase cellular proliferation and drive tumor development[130]. Substrate functionalization in the microdevice is usually achieved with a fibrous protein or glycoprotein coating such as collagen and/or fibronectin.

In the work presented in this thesis, cells are largely constrained to a 2D environment. It is known that the dimensionality of the microenvironement impacts the cellular behavior. For instance, fibroblasts, osteoblasts, and endothelial cells are known to reorient preferentially parallel to the stretching direction in 3D cultures, as opposed to the near-perpendicular alignment observed on membranes[131]. In the context of cancer development, independently of stretching, the importance of dimensionality is well illustrated by the case of human mammary fibroblasts (HMFs). Their progression was observed to be more invasive when cultured in 3D scaffolds rather than on 2D substrates[132]. This was attributed to increased levels of several paracrine factors in response to the former geometry. In this thesis, we focused our exploratory work on complex 2D strain fields in order to build upon the particularly large body of work addressing the mechanoresponse of cells cultured on stretched membranes. In future studies, it would be relevant to investigate how the cellular gradient sensing and response observed in Chapters 3-4 hold in 3D environments. The 2D geometry of our device is biologically relevant in certain contexts, like in the work presented in Chapter 5 since in vivo epithelial cells form very thin layers enveloping organs.

Microfluidics are indeed powerful tools to create in vitro environments exhibiting physiological properties such as complex strain fields. The following section presents concepts related to the physics of material deformations that will be particularly useful for Chapters 2 to 4.

1.2.6 CHARACTERIZATION OF COMPLEX STRAIN FIELDS

The intrinsically dynamic nature of living organisms gives rise to a myriad of internal forces. Since biological tissues are for the most part compliant materials, these forces result in deformations

varying from less than one percent (human bone) up to tens of percent (heart, lung)[133–135]. In this thesis, the amplitudes of the applied deformations have been carefully determined based on previous in vitro studies operated under similar conditions. Amplitudes of 3-10% have been previously shown to induces cellular responses for both fibroblast[34,136] and epithelial[30,137] cells and are biologically relevant, as presented in Chapters 3-5. Substrate deformations can be quantified by mapping the strain field. A strain represents the relative deformation of a material resulting from an applied force. In one dimension, the strain ε of an elongated material is defined as:

$$\varepsilon = \Delta L / L_0 \tag{9}$$

where ΔL is the change in length and L_0 is the original length. In the context of biophysical studies, a common strategy employed to investigate the effect of strain on cellular behaviors consists in growing adherent cells on a stretchable membrane. In two dimensions, in addition to the longitudinal strain described above, one can define the shear strain. Consider the two-dimensional element represented by a square in Fig. 1.4a. A purely longitudinal strain would correspond to its elongation in X or Y while retaining four right angles. In contrast, a shear strain would correspond to a change in angle. The Green strain tensor can be used to described strains beyond one dimension. When a thin membrane is being stretched, the following equation allows the calculation of the Green strain components ε_{ij} at a given point on the membrane[138]:

$$\varepsilon_{ij} = \frac{1}{2}\left(\frac{\partial u_i}{\partial H_j} + \frac{\partial u_j}{\partial H_i} + \frac{\partial u_i}{\partial H_i}\frac{\partial u_i}{\partial H_j} + \frac{\partial u_j}{\partial H_i}\frac{\partial u_j}{\partial H_j}\right) \tag{10}$$

where u is the displacement vector and H is the position vector. Considering the two-dimensional element shown in Fig. 1.4b, the strain components can be approximated by:

$$\varepsilon_{xx} \approx \frac{ab_x - AB}{AB} + \left(\frac{ab_x - AB}{AB}\right)^2 \tag{11}$$

$$\varepsilon_{xy} \approx \frac{1}{2}\left(\frac{ac_x - 0}{AC} + \frac{ab_y - 0}{AB} + \left(\frac{ab_x - AB}{AB}\right)\left(\frac{ac_x - 0}{AC}\right) + \left(\frac{ab_y - 0}{AB}\right)\left(\frac{ac_y - AC}{AC}\right)\right) \tag{12}$$

where AB, AC, ab_x, ab_y, ac_x, ac_y are defined in Fig. 1.4b. It is always possible to define a coordinate system in which the shear strain is zero. This is accomplished by diagonalizing the Green strain matrix. The resulting eigenvalues correspond to the principal strain amplitudes and the eigenvectors give the principal strain directions. In the context of a stretched membrane, the maximum principal strain corresponds to the direction of maximum stretch and the minimum principal strain corresponds to the direction of minimum stretch (or maximal compression). The coordinate system of the principal strain is used to describe the strain fields in Chapters 3 to 5.

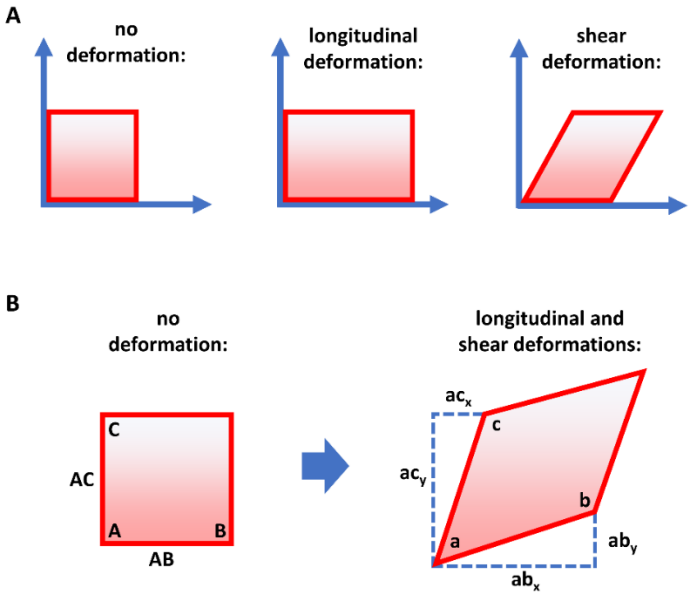

Figure 1.4 Strains in two dimensions. a) Deformations of a square element corresponding to a pure longitudinal strain and a pure shear strain. **b)** Definition of the lengths used in equations (11) and (12) for a combination of longitudinal and shear deformations.

Due to their scale and flexibility, microdevices are highly efficient platforms for mimicking various aspects of the complex mechanical landscape in which cells evolve in vivo. In particular, the cellular microenvironment is generally non-static and non-uniform, giving rise to spatially and temporally varying strain gradients. Reproducing the complexity of the strain fields occurring in vivo does not only require achieving similar strain amplitudes but also representative strain gradient amplitudes. It was reported by Richardson *et al.*[139] that strain gradients in vivo can range from 0 to ~10^2% mm^{-1}. If one wanted to produce a constant strain gradient of 10% mm^{-1} over a membrane length of 10 cm, it would imply a strain amplitude reaching at least 1000%. Evidently such high strain amplitude is not representative of typical in vivo environments and would lead to cell death or permanent damage (reported to occur around 40% strain for red blood cells[140] and 50% strain for rat primary alveolar epithelial cells[141]). Furthermore, very few materials can sustain this amplitude of deformation. Since the gradient amplitudes achieved with a given non-uniform strain pattern scales inversely with the device dimension, an effective solution is to use microdevices. For instance, the same gradient of 10% mm^{-1} can be achieved with a strain varying smoothly between 0 and 10% over a membrane length of 1 mm. This range of strain amplitudes is known to induce cell responses in the context of cyclic stretching[35,36,142].

In order to study the influence of complex strain fields on cellular behavior, we adopted such strategy of using microstretchers. The non-uniformity of the strain field requires a point-by-point characterization. Specifically, for each cell, it is of primary interest to extract the local maximum principal strain direction ($\theta_{\mathrm{strain}}(x,y)$) and amplitude ($\varepsilon_1(x,y)$), as well as the gradient amplitude ($|\nabla\varepsilon_1(x,y)|$) and direction ($\theta_{\mathrm{gradient}}(x,y)$). The gradient direction represents the direction for which the strain amplitude is changing most rapidly. The four local strain parameters noted above are determined directly from the local Green strain components $\varepsilon_{xx}(x,y)$, $\varepsilon_{yy}(x,y)$ and $\varepsilon_{xy}(x,y)$, as explained above. The latter are calculated with equations (11) and (12), based on the experimentally determined local membrane displacements upon stretching (the methodology is explained in Chapter 2).

1.3 OPTICAL MICROSCOPY IN MICROFLUIDIC DEVICES

To study the cellular response to membrane deformations, wide field phase contrast microscopy and confocal fluorescence microscopy were both used extensively in this work. Their working principles are now briefly described, along with their theoretical performances. The objective is to show their suitability to image the cells and cell components studied in this thesis and to investigate the consequence of imaging cells inside microfluidic devices.

1.3.1 WIDE FIELD PHASE CONTRAST MICROSCOPY

Optical contrast in standard brightfield microscopes arises from light absorption by the sample (naturally occurring or as a result of staining) which straightforwardly renders darker the image areas where the sample is more absorptive. When dealing with transparent samples such as most cells are, a label-free alternative can be employed: phase contrast microscopy. In the latter, contrast arises from variations in refractive index within the sample[143,144]. As the incident wavefront propagates through the sample, scattering objects having refractive indices different from the surrounding medium cause a fraction of the light to be diffracted and phase-shifted. The optical system is designed such as to convert these phase shifts into intensity differences upon interference with a reference wavefront (namely the fraction of light unperturbed by the scattering elements). It is worth noting that other than potentially degrading the resolution, the presence of a PDMS layer between the microscope objective and the cells does not affect one's ability to perform phase contrast imaging. The reason is that such object of uniform refractive

index will produce a uniform phase shift of the incident wavefront and it will not cause significant diffraction. A PDMS layer is thus essentially invisible.

1.3.2 CONFOCAL FLUORESCENCE IMAGING

Rather than relying on phase shifts, fluorescence microscopy involves the absorption by the sample of an incident photon at a given wavelength and its reemission at a red-shifted wavelength[143]. Such strategy allows high resolution imaging of specific sub-cellular structures upon labelling. This generally requires the attachment of fluorophores to the targeted sub-cellular structures. Fluorophores are fluorescent particles that have high quantum yields, i.e. a high ratio of number of photons emitted per number of photons absorbed. Attachment specificity is typically accomplished with immunofluorescence strategies which involve the use of antibodies to which the fluorophores are chemically linked. As mentioned in section 1.2.3, fluorescence staining via microfluidic channels unavoidably create shear stress on cells, thus increasing the chance of compromising their integrity. It is crucial to minimize perturbations to the cells in order to prevent immunofluorescence measurement artifacts which are associated with delocalization or extraction of proteins under study[145].

The capacity of scanning confocal fluorescence microscopes to acquire high-contrast and high-resolution images results from two key properties[146]. First, the fluorescence excitation is largely localized to a small volume within the sample due to the use of a laser and pinhole system that enables tight focusing. Second, only the fluorescence light emitted from the corresponding focal volume is efficiently collected, while the light emitted from other regions (in particular out-of-focus light) is rejected. This is achieved by introducing a second pinhole in front of the high-sensitivity detector. This pinhole is the conjugate of the excitation pinhole. The 2D image of each Z-slice is recorded point-by-point using a scanning system.

1.3.3 RESOLUTION OF OPTICAL MICROSCOPES AND THE EFFECT OF IMAGING WITHIN A MICROFLUIDIC DEVICE

The resolution of a microscope refers to the smallest distance for which two point-like objects are still resolvable. If the resolution of microscopes was not limited, an infinitesimal volume within the sample would form an infinitesimal point at the image plane. Due to the wave properties of light, this is not possible. The collection optics (mainly the objective) have finite apertures which produce a diffraction pattern. The image of a point within the sample thus becomes spatially

extended at the detector. For a uniformly illuminated circular aperture, which is essentially the case here, the transverse profile of the diffraction pattern is the Airy function[143,146]. The smaller the aperture (or more precisely the smaller the numerical aperture (NA)), the wider the imaged spot is. Consequently, the images of two points that are too close within the sample will overlap at the detector so they will not be individually resolved. The 3D diffraction pattern associated with the light emanating from an infinitesimal volume within the sample is called the point spread function (PSF). Note that it is typically reported with respect to the object scale even if the PSF is formed at the image plane. The theoretical lateral (X and Y) resolution of a microscope is often defined as the distance between the zero-order peak of the PSF and the first minimum in the lateral direction. The axial (Z) resolution is expressed similarly. These definitions are based on the Rayleigh criterion. In practice, the analysis of the effective resolution is complexified by the excitation geometry and the use of pinholes, but the general ideas apply nevertheless[146]. In particular, the achievable contrast directly affects the resolvability of two closely spaced point-like objects and thus it affects the usable resolution. For instance, the presence of significant out-of-focus light in a widefield microscope strongly limits one's ability to use the theoretically available resolution, in contrast to a confocal microscope.

The theoretical diffraction-limited lateral resolutions of a wide-field microscope can be estimated by the following equation[143]:

$$r_{lateral\_wf} \approx 0.6\frac{\lambda}{NA} \tag{13}$$

where λ is the wavelength of the source. The numerical aperture is defined as $NA = nsin(\upsilon)$, where n is the refractive index of the immersion medium and υ is the half angle of the objective's acceptance light cone. Using a common NA = 0.6 water immersed objective operated with green light ($\lambda \sim 0.5\ \mu m$), the theoretical optimal lateral resolution of a wide-field microscope is on the order of 0.5 µm, well below the typical width and length of adhered cells. Consequently, even if the resolution is lower than the above estimate in practice, it is fully sufficient to resolve the cellular morphology. Along with the elements discussed in section 1.3.1, this makes the phase contrast microscope well suited to study the lateral morphology of living cells cultured on a flat surface within the microfluidic devices. Due to the lack of specificity and poor effective axial resolution of this microscopy technique, it is not always suitable however for imaging some sub-cellular components.

The theoretical diffraction-limited lateral and axial resolutions of a confocal microscope (with an optimally selected pinhole size) can be estimated by the following equations[143]:

$$r_{lateral\_conf} \approx 0.4 \frac{\lambda}{NA} \quad (14)$$

$$r_{axial\_conf} \approx 1.4 \frac{n\lambda}{NA^2} \quad (15)$$

Using a 1 NA water immersed objective operated with green light, the theoretical optimal lateral and axial resolutions are on the order of 0.2 µm and 0.8 µm, respectively. The full width at half maximum (FWHM) of the PSF's zero-order peak is similar (within 20%) to the resolution as defined above[147]. Experimentally, the PSF (and thus the resolution) of fluorescence microscopes is often determined by measuring the profiles of fluorescent beads which diameters are significantly smaller than the resolution. The lateral and axial resolutions are then directly determined (upon deconvolution) from the FWHMs of the corresponding measured profiles.

When imaging structures having dimensions as small as a few microns or less (such as the FAs and the F-actin, both imaged in the studies presented in Chapters 3 to 5), sub-micron resolution is evidently desired laterally. Importantly, an axial resolution on the order of 1 micron is also required to isolate the plane of interest for achieving a high signal-to-background ratio. This is crucial for properly imaging fine structures and for studying with good precision the height profile of various structures in cell population. A confocal microscope is thus well suited as long as aberrations do not significantly worsen the theoretical estimates mentioned above.

Optical aberrations typically cause the experimental resolution to be lower than the above diffraction-limited estimates. Microscope objectives are designed to minimize aberrations for specific immersion media such that near-diffraction limited imaging can be achieved under optimal conditions. The presence of a layer having a different refractive index between the cells and the microscope objective negatively impacts the resolution, in particular axially. This can be attributed largely to the introduction of spherical aberrations which cause the focal volume associated with both the excitation and the fluorescence collection to be elongated axially (and to a lesser extent laterally) (Fig. 1.5). Multilayer all-PDMS devices typically introduce such a refractive index mismatched layer ($n_{water} \approx 1.33$, $n_{PMDS} \approx 1.42$)[148], strongly compromising the confocal imaging performances achieved within them. Such degradation in resolution is

quantified in Chapter 4 (section 4.3.1 and 4.3.2), and the microfabrication strategy developed to overcome this issue is presented.

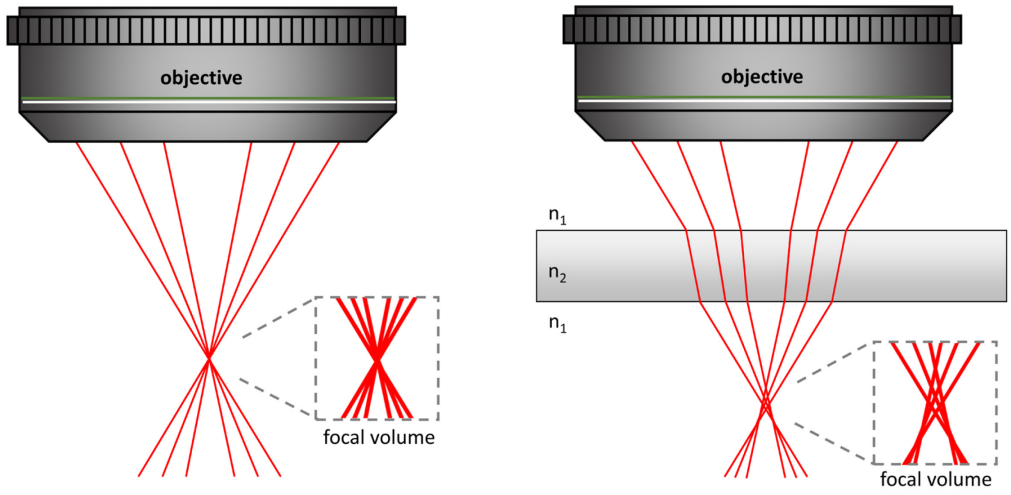

Figure 1.5 Spherical aberration. Impact of introducing of a planar slab of material between the cells and the objective of a confocal microscope. From a ray optics point of view, the objective is designed such as to converge all the incident rays towards a single point for a given immersion medium **(left)**. Similarly, the light transmitted through the detector pinhole is meant to originate from this single point also. Upon introduction of a slab of material having a mismatched refractive index, refraction causes the inner and outer rays to converge at different points. This elongates and smears out the focal volume, strongly affecting the resolution, in particular axially **(right)**.

CHAPTER 2 | CELL STRETCHING MICRODEVICE

This chapter is a summary of my contribution to the following article, together with additional technical information (note that the manuscript is not included in this thesis):

> Tremblay D., **Chagnon-Lessard, S.**, Mirzaei, M., Pelling, A.E., Godin, M. A microscale anisotropic cell stretching device for applications in mechanobiology. *Biotechnology Letters* **36,** 657-665 (2014).

The main advance discussed in this article is of a technical nature; it presents the design and characterization of a cell stretching device mimicking the cells' microenvironment by producing biologically relevant strains. The present chapter focuses on the methodology and techniques that I have employed both for my contribution to this article and for the subsequent work presented in Chapter 3 to 5.

The initial device design and fabrication strategies published in *Tremblay et al*.[44] were conceived by Dr. Godin, Dr. Mirzaei, and Dr. Tremblay. Sections 2.2 and 2.3 briefly presents this design and its working principle, as well as the standard microfabrication strategies we employed. Dr. Tremblay and I both fabricated a large number of microdevices to carry out the experiments of this paper. One proof-of-concept experiment (performed by Dr. Tremblay) is included in the paper (but not showed in this chapter). Importantly, the article also demonstrates the technical capabilities of the device[44]. This work represents most of my contribution to the article and is summarized in sections 2.4 and 2.5 of this chapter. The experimental control system that I have assembled to perform the device characterization experiments is first briefly discussed (section 2.4). Section 2.5 presents the strain calibration curves of the ε_{xx} and ε_{yy} components as well as a map of the membrane strain amplitude. This section also includes details of the methodology that I have employed to obtained these results, including data acquisition, extraction and processing. I have also performed the work (experiments and analysis) related to the attenuation of the Poisson ratio effect in the central region of the stretched membrane. The resulting strain calibration curves are presented in section 2.5. They show that the effect of the Poisson ratio can be greatly compensated by programming a specific stretching pattern by activating both the X and Y axes simultaneously.

Following the publication of the paper by *Tremblay et al*.[44], I modified the initial device design to improve its efficiency and capabilities such as to enable the studies presented in the

Chapter 3 to 5. Section 2.6 presents this modified design, while the details of its fabrication and imaging capabilities are given in Chapter 4.

2.1 EXPERIMENTAL TOOLS TO ASSESS CELLULAR MECHANICAL PROPERTIES

A rapidly growing body of work shows that cellular responses to mechanical stimuli constitute regulatory mechanisms of many fundamental biological functions[1,13,56,149,150]. Better understanding these mechanisms can uncover the cause of certain human pathologies since many are related to defects in mechanotransduction[4,5]. The development of a cell stretching device reproducing in vivo strains more accurately is part of this effort by filling a technology gap.

To mechanically stimulate and probe cells and their microscopic components, many experimental tools have been developed with resolution ranging from microns to picometers[25,29]. To name a few, they include atomic force microscopy (AFM), Brillouin spectroscopy, optical stretchers, and magnetic/optical tweezers that enable precise manipulations and/or mechanical quantifications of diverse biostructures[104]. Common difficulties encountered during this type of measurements are: i) the influence of the experimental tool itself on the mechanical state of the specimen under study, ii) low throughput due to the complex sample preparation or tool utilization, and iii) some tools require to expose cells to condition that are far from physiological.

It is relevant here to consider the case of optical stretchers, which enable controlled deformation of suspended cells. In this method, the micromanipulation of a cell or another dielectric material allows for precise determination of its viscoelastic properties[151]. The photons of two slightly divergent laser beams coming from opposite directions transfer momentum to the surface of the object, generating surface forces. The net force on the object is zero, but the surface forces are additive, leading to cell stretching along the beam axis[152]. While cells in optical stretching experiments are easily characterized over their whole body, they have to be suspended in solution which represents an unusual condition for most cell types.

The motivations for using microfluidic stretchers have been outlined in Chapter 1. Above all, their small scale can naturally give rise to complex, biologically relevant non-uniform strain-fields[45]. The benefits of using microfluidics also include the potential for performing high-throughput screening experiments while using low reagent quantities, the ability to integrate multiple on-chip functions, and lower risk of contamination. Various strategies are currently

employed to cyclically or statically stretch adhered cells in microdevices[153]: piezoelectric actuations, electromagnetic actuation, and pneumatic actuation. Piezoelectric actuation can generate a broad range of stretching amplitudes with high precision[154]. However, this stretching strategy generally requires a direct contact with cells, thus limiting its versatility. Electromagnetic actuation methods employ controlled electromagnetic motors to stretch the cells' substrate[155]. It offers high stretching precision with a relatively simple setup. The disadvantages include overheating and potential contamination that originate from the lubrification. Finally, pneumatic actuation is particularly simple, it can be integrated at low costs, and it generally involves no contact of potential actuator-related contaminants with the cells or the media [11,153,156]. Precise calibration is required to ensure that the applied pressure results in the desired strain amplitude for every device. In this context, the degree of uniformity among the devices' performance is critical. Therefore, well-developed and precise microfabrication protocols were elaborated in this work to ensure consistency.

The devices presented in this chapter builds upon previously reported pneumatic-based microstretchers developed by Huh *et al*.[11], Kim et al.[157], and Huang *et al*[158]. In contrast to previous designs, however, our microstretcher can impose changing and time-varying non-uniform strain fields with independent bi-axial control. This advance enables to better mimic the complexity occurring in vivo.

2.2 WORKING PRINCIPLE AND FIRST DESIGN

The microfluidic stretcher which we developed consists of a multi-layer PDMS device. It includes a suspended 10 µm thick deformable membrane on which the cells are cultured. This membrane is sandwiched between two thicker layers which exhibit precise patterns forming chambers and channels (Fig. 2.1a,b). Cells are seeded via microfluidic channels which are connected to the cell chamber. To stretch the cells, low pressure is applied cyclically to one or multiple vacuum chambers (typically a sinusoidal waveform is applied synchronously to two opposite vacuum chambers). The working principle is presented in Fig. 2.1c,d, which shows schematics and pictures of the relaxed and stretched states. Upon application of partial vacuum in the chambers, the walls are deformed inward which pulls on the thin membrane, hence stretching the adhered cells. A similar working principle was employed in the previous designs from which our device was inspired, as well as in our second design which will be discussed in section 2.6 and in Chapter 4.

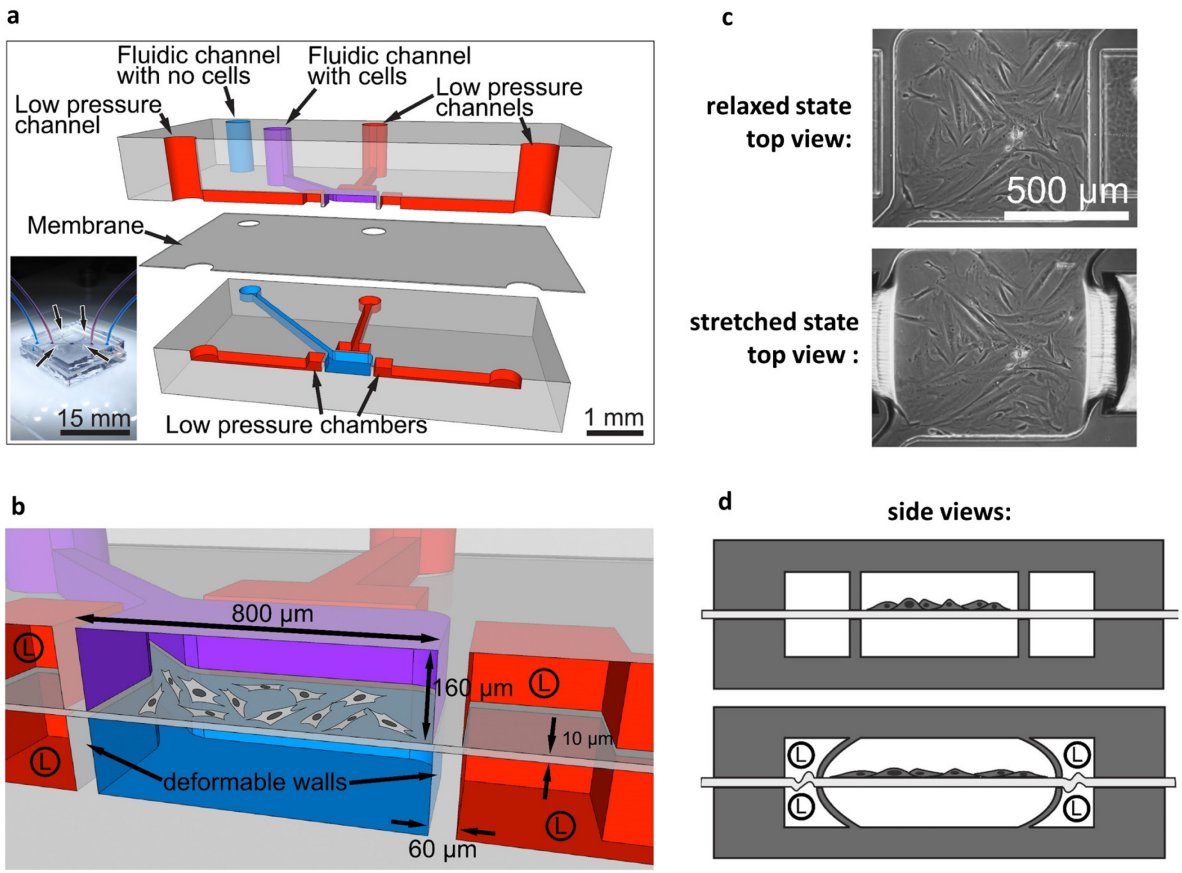

Figure 2.1 Microfluidic cell stretcher design and working principle. a,b) Cross-section presenting the three PDMS layers forming the device. Low pressure is applied to the red channels to deform the thin walls in which the membrane (10 µm thick) is anchored. The four vacuum chambers (circled ''L'' indicates low pressure) allows to stretch independently the four sides of the square cell chamber (800 mm x 800 mm). A picture of an assembled device (inset of **a)**) exhibits the microfluidic tubes allowing cell seeding (top channel in red) and media flowing (bottom channel in blue) to equilibrate pressure. **c)** Representative top view images of the membrane before and after vacuum activation (in two oppositely-located vacuum pumps). The adhered cells are human fibroblasts. **d)** The working principle is depicted via schematics of the side view, in both the relaxed and stretched states. Adapted from[44].

2.3 MICROFABRICATION

The microstretcher described above is fabricated with standard lithography and PDMS replication procedures. The key steps are briefly described below. For the most part, the modified microstretcher described in section 2.6 and in Chapter 4 utilizes the same fabrication steps, except for a few additional procedures which is outlined therein.

As mentioned previously, the microstretchers are made entirely of PDMS, a rubber-like biocompatible elastomeric polymer essentially transparent in the visible region[159]. The bottom and top layers of the device are produced by casting PDMS into master molds that are fabricated by proximity photolithography. Robust fabrication methodology insured high platform reproducibility. Precise protocols were elaborated, for example to achieve consistent master mold features and PDMS shrinkage.

2.3.1 MASTER MOLD FABRICATION

First, the patterns are designed in a graphics software and printed to scale (CAD/Art Services, Inc) onto a transparent sheet of plastic. This photomask is used as a pattern generator during the master mold fabrication. A magnified view of the photomask used to produce the modified microstretcher is shown in Fig. 4.6a of Chapter 4.

The master mold is composed of two layers: a polished silicon wafer which acts as an ultra-flat substrate, and a photosensitive polymer which forms the features. The master mold fabrication begins with thorough chemical wet cleaning and baking in order to remove contaminants and adsorbed water[160]. Contaminants can be detrimental in various ways, including with respect to pattern quality and adherence. A spin coater is then employed to spread one (or multiple) uniform layer(s) of permanent epoxy-based negative photoresist (MicroChem, SU-8) onto the silicon wafer. Evaporation of most of the solvent is then achieved by a baking step called soft-bake. A mask aligner is utilized to bring the resist-covered wafer in contact with the photomask and expose the assembly under UV light. This results in cross-linking of the unmasked photoresist regions, rendering them insoluble. Optimal exposure parameters are required to obtain vertical side walls[161]. It is interesting to note that the high reflectivity of the silicon wafer results in the creation of a standing wave due to the interference of the incident and reflected light during exposure[162]. Post-exposure baking promotes diffusion of photo-generated molecules in order to smooth out potentially undesired cross-linking modulations. During the development process, the prescribed solvent etches away the soluble (non-exposed) regions, while the stable cross-linked (exposed) regions are left intact. It is worth noting that although passive immersion is typically prescribed, we recently found that the deep and narrow trenches in our design are much better developed by attaching the master to a stirring bar (400 rpm). A final baking step, the hard bake, hardens the resist, reduces surface cracks, and helps with overall feature adhesion.

Finally, silanization of the master mold is performed in a vacuum chamber to deposit an antiadhesive layer to facilitate the eventual PDMS unmolding. Fig. 2.2 summarizes the steps described above.

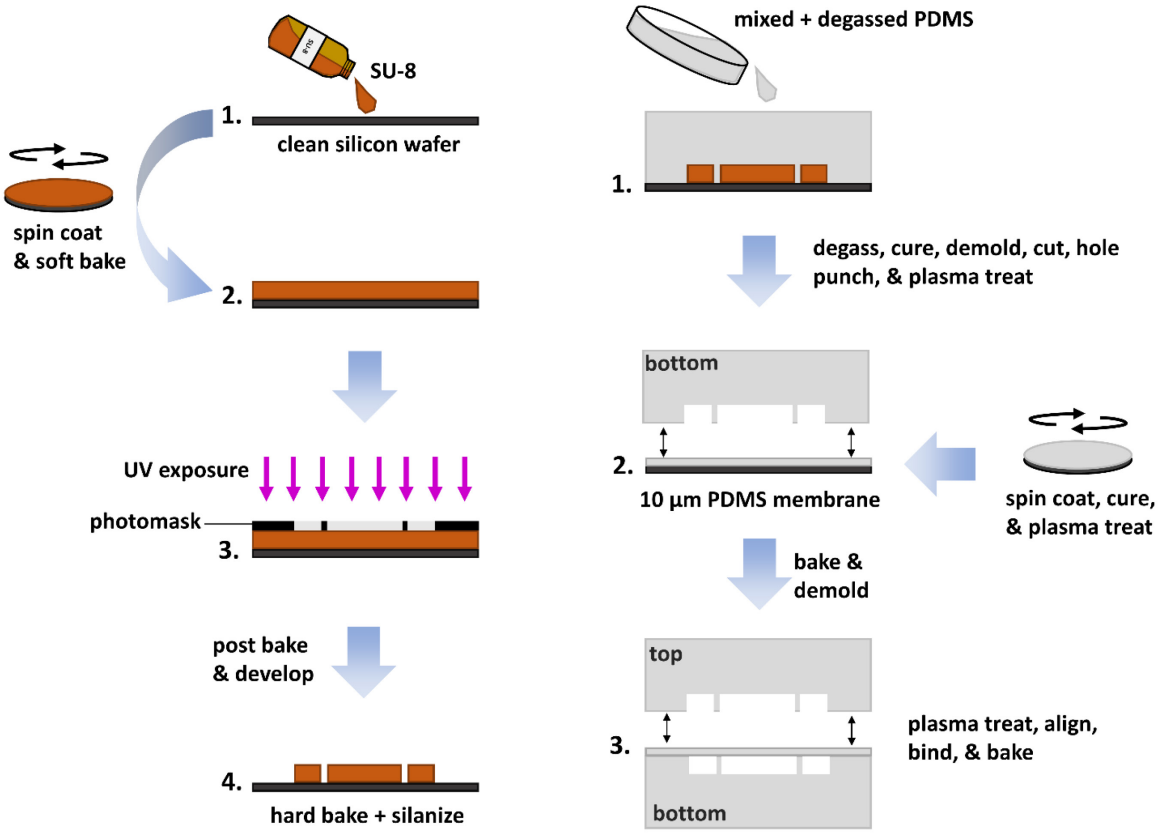

Figure 2.2 Fabrication of the microstretcher. Main steps to produce the master mold **(left)** and the PDMS microfluidic device **(right)**.

2.3.2 Molding of the top and bottom layers, membrane fabrication, and device assembly

PDMS molding is now outlined. After standard mixing and degassing steps, uncured PDMS is poured over the SU-8 master mold. It is then further degassed (air removal) prior to being thermally cured. Demolding, cutting, and hole punching complete the preparation of the top and bottom layers of the device prior to assembly.

The 10 µm thick membrane (which will eventually serve as the stretchable cell substrate) is prepared by spin coating uncured PDMS (mixed with fluorescent microspheres, see section 2.5.1) onto a cleaned, salinized silicon wafer. After curing, the membrane is plasma treated,

together with the bottom layer, in order to render their surface chemistry suitable for strong bond formation[160]. Namely, oxygen plasma treatment turns a fraction of the methyl groups (CH_3; low reactivity) into hydroxyl groups (OH; high reactivity) on the PDMS surfaces. After permanently bounding the membrane and the bottom layer, strategic membrane holes are perforated. Finally, further plasma treatments and the use of an alignment system insure strong adhesion and precise positioning of the top layer onto the membrane-bottom layer.

2.4 EXPERIMENTAL CONTROL SYSTEM

The major components of the experimental control system employed to operate the microstretchers are schematically depicted in Fig. 2.3. There are two principal functionalities: regulation of the rate of fluid flow in the microfluidic system and control of the strain pattern generated on the membrane. A home-made labview program[†] is used to the control pressure regulators and vacuum controllers, as well as to read the vacuum sensors via data acquisition cards (DAQs). Various circuit elements (not shown) are included to provide accurate voltage levels and ensure stability of these apparatuses. The precise control of the flow rate via pressure regulators permits cleaning operations, membrane functionalization, cell loading, drug and media loading, cell fixing, and staining. These procedures are usually performed under a phase contrast microscope, while the cyclic stretching experiments are run inside an incubator (a commercial instrument or portable home-made version when time-lapsed microscopy is needed). The pressure within the vacuum chambers is precisely controlled (and monitored) in order to achieve the desired membrane strain direction, amplitude, waveform frequency and shape, etc.

[†] Adapted from the initial version written by D. Tremblay.

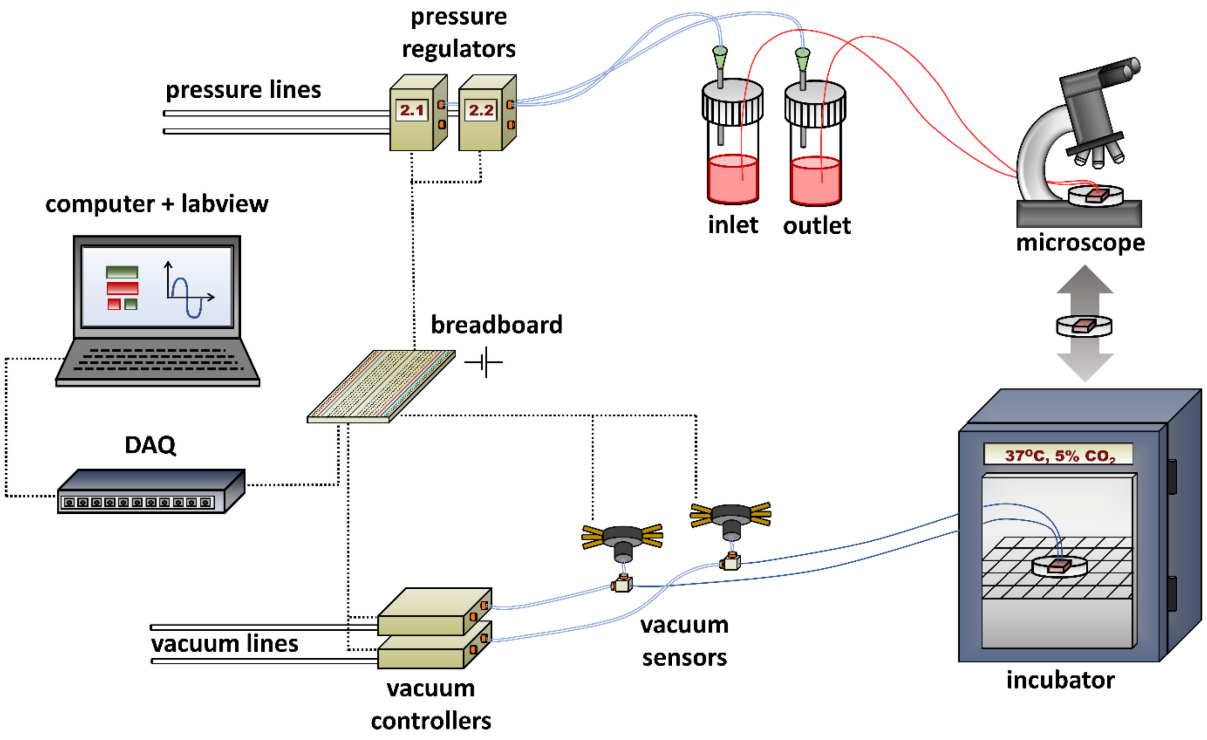

Figure 2.3 Experimental control system to operate the microstretcher. The top branch controls the rate of the fluid flow in the microfluidic channels. The bottom branch controls the pressure applied to the vacuum chambers to stretch the membrane. The experiment preparation is usually carried out under a microscope while the experiment itself is run inside the incubator for optimal temperature, humidity, and ambient gas composition.

2.5 CALIBRATION OF THE MEMBRANE STRAIN FIELD

The strategy adopted to extract the membrane strain field consists in tracking the displacements of embedded fluorescence beads upon a complete stretched cycle.

2.5.1 EXPERIMENTAL METHOD

Water-suspended beads (FluoSpheres 200 nm, Invitrogen) are first re-suspended in isopropanol using standard vortex, centrifuging, and sedimentation procedures. The beads are incorporated in the PDMS curing agent using a vortex, prior to adding and mixing the monomers. This mixture is used to fabricate the membrane, which is then integrated to other layers such as to form a complete device as outline in section 2.3.2. The experimental control system described in section 2.4 is employed to stretch the membrane while the bead positions are monitored using an epifluorescence microscope (10X objective). Ten frames are acquired as the system is programmed to evolve stepwise from the unstretched (relaxed) state to the fully stretched state.

2.5.2 IMAGE ANALYSIS

The bead displacements are extracted from the experimental series of images in order to apply the strain equations (11) and (12) provided in Chapter 1. A standard image analysis program, Image J (general purpose Particle Tracker tool), was first tested. While it was possible to find settings enabling the successful monitoring of a large fraction of the bead displacements, a non-negligible number of errors systematically prevented the accurate construction of the strain maps. The main issues encountered resulted from the bead-to-bead intensity variations, the frequent occurrence of multiple beads in close proximity, and the slight changes in bead intensity profiles from one image to the next. These factors resulted in the loss or artificial separation of certain particles upon threshold application (even if local thresholding was applied), and more generally they resulted in tracking errors. A custom bead-tracking program, integrated to the subsequent strain calculations, was written in Matlab to tailor the analysis to the specificities of our experimental data. In particular, it benefits from using gaussian fits as well as a large number of carefully optimized bead identification and bead tracking criteria.

A representative map of extracted bead paths is shown in Fig. 2.4, for X-stretching. In addition to the dominant horizontal displacement, we note a small vertical component despite the fact that only the horizontal pumps are activated. Orthogonal compression upon uniaxial stretching is typical of deformable membranes. It is characterized by the Poisson ratio ($-\varepsilon_{\mathrm{lateral}}/\varepsilon_{\mathrm{axial}}$)[163], which is known to greatly influence the orientation of certain cell types[142]. For strains below 45%, the Poisson ratio of (unconstrained) PDMS is reported to be approximately 0.5[159,164]. The interpolated horizontal displacement map averaged over 5 devices is also shown in Fig. 2.4. Using such maps, the strain field can be directly calculated from equations (11) and (12). Additional details about the strain map calculation are given in sections 3.3.1 and 3.3.6.

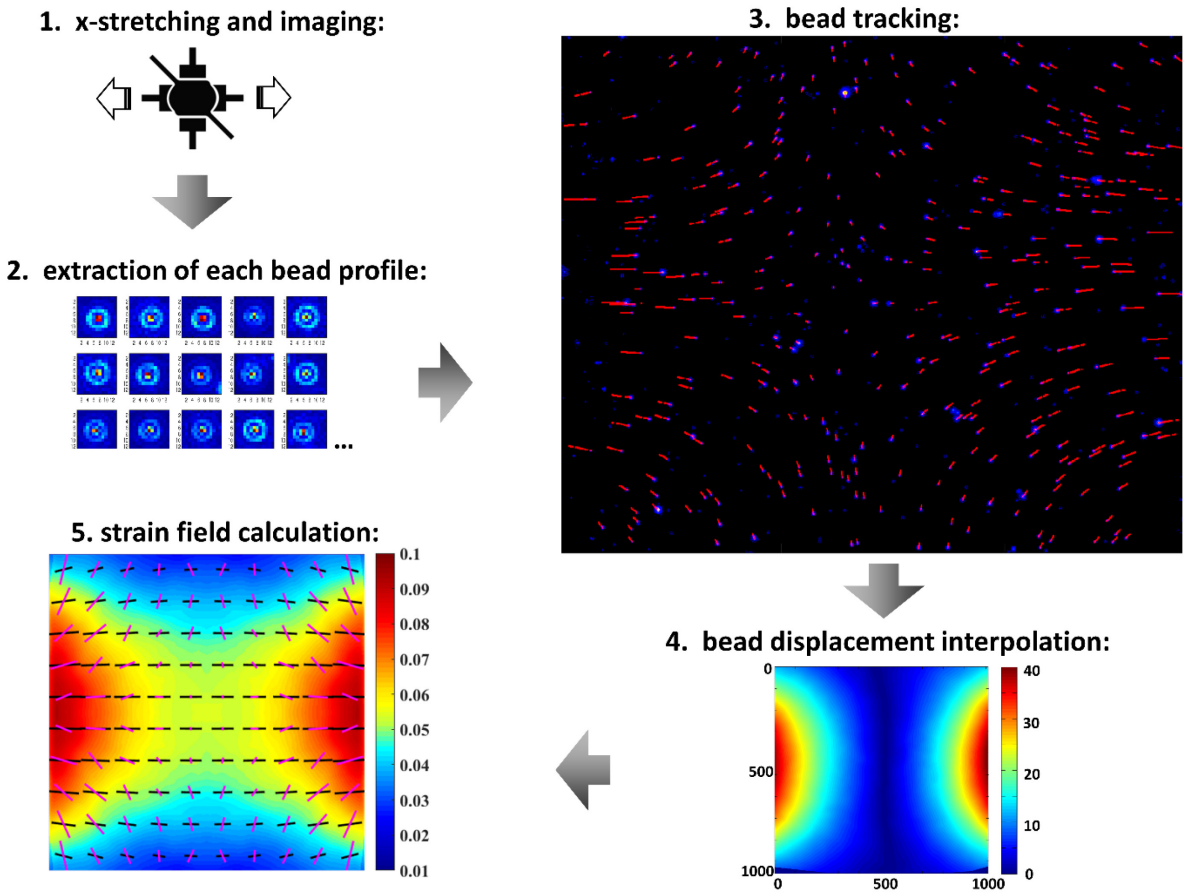

Figure 2.4 Method for calculating the strain field. 1) The cell microstretcher's membrane is stretched using the desired vacuum chambers while the beads are imaged using a fluorescence microscope. **2)** Each bead profile, in every frame, is characterized using a gaussian fit to facilitate the particle identification during tracking. **3)** Using a series of criteria, the displacement of each bead is monitored from the relaxed to the fully stretched states. The fluorescent beads are shown in blue and their displacements in red. **4)** From the collection of paths obtained in **3)**, interpolation and averaging allow to get a full map of bead displacements (only the X-displacement map is shown here). **5)** The complete strain field can then be calculated. The principal strain amplitude $\varepsilon_1(x,y)$ is represented here by the colormap. The black lines show the local direction and amplitude of the maximum principal strain, while the pink lines show the local direction and amplitude of the strain gradient.

2.5.3 CALIBRATION CURVES

Fig. 2.5 shows the near-linear relationship obtained between the pressure applied to the vacuum chambers and the average strain in the central region of the membrane, upon synchronized activation of the left and right pumps. Varying the air pressure with a given waveform thus translates into a membrane strain of similar waveform, thus facilitating the control of the strain modulation. It is also interesting to note that our device can greatly attenuate the orthogonal

compression resulting from uniaxial stretching in cases where purely uniaxial deformations are wanted. This is enabled by our independently controlled bi-axial design. Explicitly, it is accomplished by activating slightly the orthogonal vacuum pumps in order to compensate for the orthogonal compression generated by the principal stretching (Fig. 2.5). While this capability is useful in various context, we did not pursue this avenue since our primary interest is to study cell behavior in a strain field that mimics the complexity occurring in vivo.

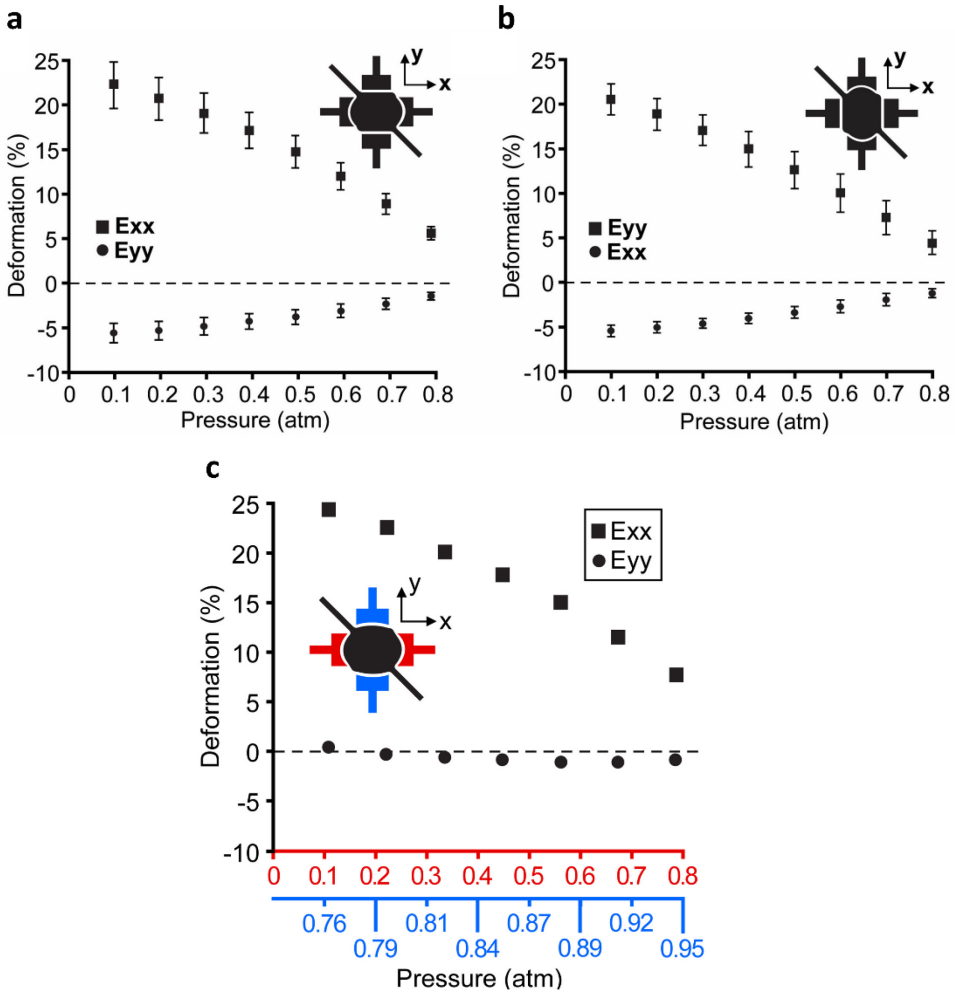

Figure 2.5 Calibration of the average membrane strain amplitudes (ε_{xx} and ε_{yy} components). The averaged area is limited to the central ~ 20%. The deformation of the PDMS membrane is displayed as a function of the pressure applied to the low-pressure chambers, for horizontal stretching in **a)** and vertical stretching in **b)**. The average non-zero orthogonal compression in this region is determined by the PDMS' Poisson ratio and the specific geometry of the system. This orthogonal compression can be almost completely eliminated by slightly activating the low-pressure chambers that are orthogonal to the principal stretching direction. In **c)**, the principal stretching direction is horizontal (red x-axis) and the orthogonal stretching direction to compensate the compression is vertical (blue x-axis). Adapted from[44].

2.6 DEVICE DESIGN MODIFICATIONS

The first version of the device enabled successful proof-of-concept experiments and set the ground for the following studies. However, various issues were encountered in subsequent work, limiting our ability to perform comprehensive biological investigations. Depending on the specificities of the biological system under study, using a permanently closed microfluidic device can introduce various difficulties. Upon seeding, two factors often result in the premature abortion of the experiment. First, it is difficult to achieve a precise cell density and uniform spreading. Second, the occurrence of clogging is frequent when a high cell density is required. Cell fixing and staining are also prone to be compromised in a purely microfluidic device. Reasons include the very large number of steps required, the need for precise and uniform exposure to the solutions, and the unavoidable occurrence of non-uniform shear stresses. Overall, the experimental data throughput achieved with our first design was relatively low in practice, in particular considering the small size of the cell chamber and the fact that experiments were done individually. Finally, while suitable for phase contrast microscopy, the presence of a PDMS layer in the optical path reduces significantly the resolution achievable in a confocal microscope. This is explained and characterized in Chapter 4.

The challenges and shortcomings described above led to the modification of the initial design. The development of this improved platform was required to perform the studies described in the following three chapters of this thesis. Below is a summary of the design modifications implemented to achieve higher experimental throughput and better imaging capabilities:

- *Ability to switch from a close- to an open-top device*: The principal improvement consists in modifying the cell chamber geometry by extending its height such as to leave a thin layer (~200 µm) of PDMS as a top sealant (Fig. 2.6). This membrane can be removed with tweezers at any point during the experiments: at the beginning for complex cell seeding procedures, or rather just before cell staining/imaging to decrease the non-uniformity of the shear stress on the cells and to increase the imaging resolution. This design modification results in increased adaptability of the device such that it can be tailored to meet specific experimental requirements. Additional details on the strategies developed to resolve the associated fabrication challenges are given in Chapter 4.

- *Scaling up the cell chamber size:* The area where the cells are cultured and stretched is increased by a factor 4.
- *Implementation of an array:* 4 microstretchers are integrated into a single chip. The photomask design of the top PDMS layer is presented in Fig. 4.6 of Chapter 4.

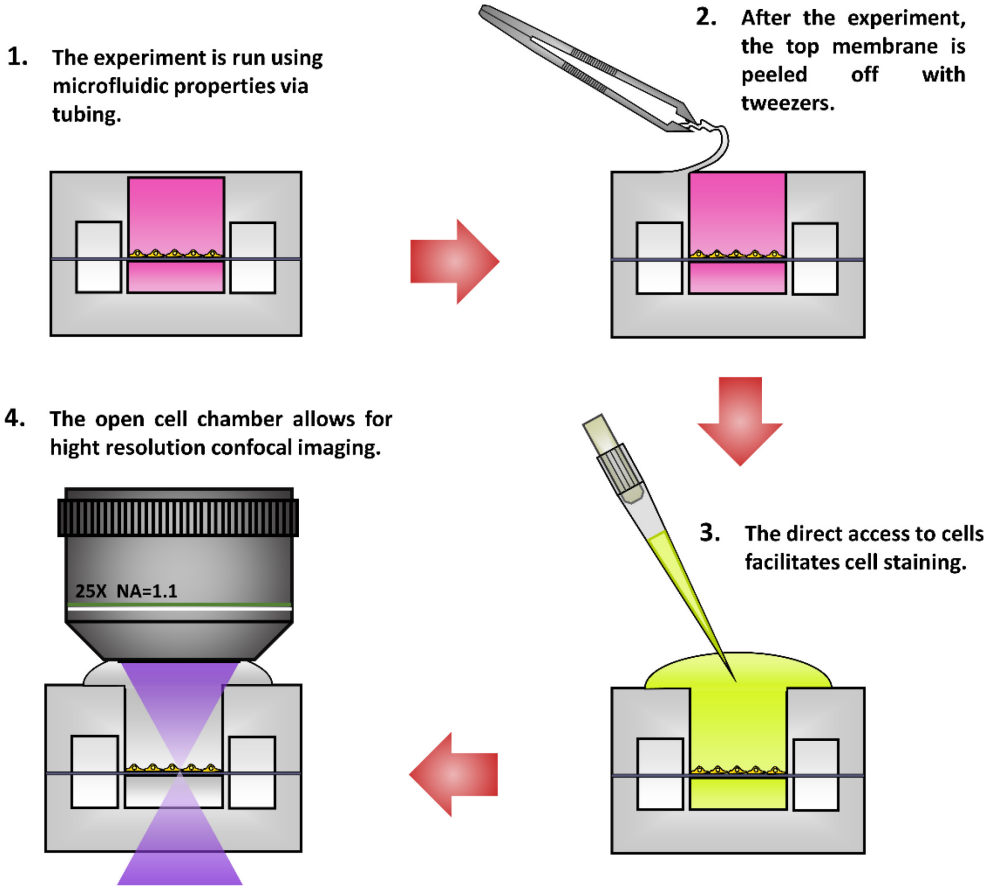

Figure 2.6 Adaptability of the modified design. Note that the device can be made open-top at any step along the course of the experiments, including in step 1), in order to facilitate complex cell seeding procedures.

CHAPTER 3 | CELLULAR ORIENTATION IS GUIDED BY STRAIN GRADIENTS

Manuscript published in *Integrative biology* on May 23rd 2017. The supplementary information is presented in Appendix A. Reproduced with the permission from:

Chagnon-Lessard, S., Jean-Ruel, H., Godin, M., Pelling, A.E. Cellular orientation is guided by strain gradients. *Integrative Biology* **9**, 607-618 (2017).

Motivation/objective: Having fully characterized and optimized the microstretcher, we apply its complex non-uniform strain field to human fibroblasts in cyclic stretching experiments. A point-by-point analysis of the cellular response as a function of the local strain allows to understand and decouple the effect of different strain components on the cell behavior.

3.1 ABSTRACT

The strain-induced reorientation response of cyclically stretched cells has been well characterized in uniform strain fields. In the present study, we comprehensively analyze the behavior of human fibroblasts subjected to a highly non-uniform strain field within a polydimethylsiloxane microdevice. Our results indicate that the strain gradient amplitude and direction regulate cell reorientation through a coordinated gradient avoidance response. We provide evidence that strain gradient is a physical cue that can guide cell organization. Specifically, our work suggests that cells are able to pinpoint the location under the cell of multiple physical cues and integrate this information (strain and strain gradient amplitudes and directions), resulting in a coordinated response. To gain insight into the underlying mechanosensing processes, we studied focal adhesion reorganization and the effect of modulating myosin-II contractility. The extracted focal adhesion orientation distributions are similar to those obtained for the cell bodies, and their density is increased by the presence of stretching forces. Moreover, it was found that the myosin-II activity promoter calyculin-A has little effect on the cellular response, while the inhibitor blebbistatin suppresses cell and focal adhesion alignment and reduces focal adhesion density.

These results confirm that similar internal structures involved in sensing and responding to strain direction and amplitude are also key players in strain gradient mechanosensing and avoidance.

3.2 INTRODUCTION

A rapidly growing body of evidence has established that mechanical forces and force gradients can act as key drivers of biological processes at the molecular, cellular, and organismal scales[13,149,150,165–167]. The web of interactions between the cell and its microenvironment involves a complex interplay between mechanical forces and biochemical signals. These interactions are made possible by the cell's ability to sense external mechanical cues, transduce them into intracellular biochemical signals, and generate short and long-term responses that orchestrate crucial cellular functions. Such mechanisms have been reported to be involved in the regulation of a variety of cellular functions such as cell migration, division, apoptosis, differentiation, and gene expression[56].

Another relevant example, which has become a case study for mechanosensitivity and response, is cell reorientation under cyclic stretching. Such stretching is experienced by cells in vivo during many processes including the pumping of the heart, the contraction of the muscles, and the expansion of the lungs. Through tissue matrix deformations and cytoskeleton-adhesion interfaces, many cell types are thus cyclically stretched, including human fibroblast[12]. It has been shown in numerous studies that adherent cells subject to cyclic uniaxial strain via a deformable extracellular matrix reorient themselves approximately perpendicularly to the strain direction to a degree that depends on the strain amplitude[30,34–41,44,68]. This was observed for frequencies above ~0.1 Hz, although the characteristic time of the response was found to be frequency dependent[34]. Over the last few decades, different models and refinements have been proposed to describe cellular reorientation and explain the underlying mechanisms behind this phenomenon[35,36,142,168–171]. It is also well established that the cytoskeletal and FA dynamics are central to this process, as they form the contractile and mechanosensing machinery. Specifically, the disruption of contractile activity can lead to the inhibition of cellular alignment[172–174]. Nevertheless, a complete understanding of the mechanism by which applied physical forces influence the FA structures and the cytoskeletal remodeling, individually and as concerted dynamics, has yet to be reached[59,175–177].

Simple strain fields can be approximated as being uniform, i.e. with a constant strain amplitude as well as a non-varying strain direction. In contrast, in complex non-uniform strain fields, the strain amplitude and potentially the strain direction vary spatially. This gives rise to a strain gradient field, also described by a specific gradient amplitude and gradient direction at each spatial location. In the majority of cases, advancements in the field have been achieved by using simplified substrate strain fields[30,34–40]. More recently, various other studies have employed ingeniously designed macro-devices with stretchable membranes that generate non-uniform strain amplitudes, both in the context of static and cycling stretching[41–43,139,178–183]. In a few cases[41–43], this approach allowed for the successful analysis of cell reorientation (among other responses) as a function of the strain amplitude over a single non-uniformly stretched membrane. In most cases, the strain field is examined with reference to the average principal strain direction, taken as the x- or y-axis, therefore ignoring local variations in strain direction. Moreover, the strain gradients that arise in non-uniform and complex strain fields are rarely considered. Importantly, in all of these studies, strain gradient dependence was not reported in the context of cell reorientation.

While simple systems generating uniaxial stretching have the benefit of isolating specific mechanical cues, they do not reproduce the complexity and the non-uniformity of the strain fields occurring in vivo[179,184,185]. Moreover, the strain gradients in the body span multiple orders of magnitude (~10^0-10^2 % mm^{-1})[139] and are oriented along multiple directions with respect to the principal strain. Importantly, it is known that cells are able to sense chemical gradients[186] as well as substrate stiffness gradients[187], which were both demonstrated in the context of preferential cell migration. Therefore, we hypothesize that the strain gradient plays a key role in the phenomenon of cellular reorientation in non-uniform strain fields. Such a finding would imply that cells are able to sense multiple components of a complex strain field (amplitude and direction of the principle strain and strain gradient) and integrate these diverse mechanical cues in their response.

Here, we present a PDMS stretching microdevice (an earlier version of which was reported previously [44]) that allows for the generation of a highly non-uniform strain field across the membrane surface, non-uniform principal strain directions, and non-uniform gradients. The necessity for a microdevice arises from the need for generating significant strain gradient amplitudes on the cellular scale while maintaining a maximum strain amplitude of approximately

10%. This falls in the amplitude range known to induce cell alignment following cyclic stretching[35,36,142]. Therefore, the design of our microdevice allows us to mimic complex in vivo physical forces that can play a critical role in cell biology.

Comprehensive analysis of human foreskin fibroblast (HFF) cell reorientation under cyclic stretching in the device employed in this study indicates that the final orientation of the cells is determined by both the strain and the strain gradient fields experienced by the cells individually. We found a strong correlation between the strain amplitude and the degree of cell normal alignment with respect to the principal strain direction (i.e. the degree to which the elongation axis of the cells aligns perpendicularly to the principal strain direction). More importantly, we were able to clearly demonstrate a similar correlation between the strain gradient amplitude and the degree of cell normal alignment with respect to the maximum principal strain gradient direction. To further investigate this cellular behavior under cyclic non-uniform anisotropic strain, we examined the influence of the myosin-II activity on the cell reorientation as well as on the FA density and orientation. Under our experimental conditions, we discovered that the effect of the stretching force alone leads to a slight increase in FA density, while their orientation follows the direction of cell elongation. We also show that myosin-II contractility is a major player of the phenomenon of cell sensitivity to strain gradients arising in complex cyclic strain fields.

3.3 RESULTS

3.3.1 DESCRIPTION OF THE MICRODEVICE'S NON-UNIFORM ANISOTROPIC STRAIN

In order to produce biologically relevant strain gradients with directions that are decoupled from those of the strains, we developed a PDMS stretching microdevice. A schematic of this device is presented in Fig. A.1 (Appendix A), and details of its fabrication, working principle, and thorough characterization are provided in section 3.6 and in the Appendix A. At any position on the membrane, the direction and the amplitude of the maximum principal strain $\boldsymbol{\varepsilon_1}(x,y)$ (maximum stretch) were extracted. The non-uniformity of the maximum principal strain gives rise to a gradient, $\nabla\varepsilon_1(x,y)$, which can also be described by an amplitude and a direction. This amplitude represents the local rate of change of the maximum principal strain amplitude, and its direction points toward that of greatest change. Fig. 3.1 provides a visual guide to the key parameters involved in the cell orientation analysis. The underlying color map of Fig. 3.1a is that of the maximum principal strain amplitude profile $\varepsilon_1(x,y)$. In Fig. 3.1b, the lengths and directions of the

blue lines represent the maximum principal strain vector $\boldsymbol{\varepsilon_1}(x,y)$, amplitudes and directions respectively (Fig. 3.1b). ε_1 is maximal near the top and bottom vacuum pumps (not shown) and is relatively constant in the central region. The red lines represent the amplitudes and directions of the gradient $\nabla\varepsilon_1(x,y)$. The gradient directions are orthogonal to the lines of strain equi-amplitude (color lines in the amplitude map). It should be noted that the effect of the gradient on the cellular reorientation is most likely to be observed where the gradient amplitude is large while the strain amplitude is low, such as near the corners.

The complex strain field generated by this device enables the differentiation between the cellular response induced by the strain field and that induced by the strain gradient field. Many previous studies have employed a largely uniform and anisotropic strain, which allowed them to report the data on a fixed axis[30,35–40]. In our case, the non-uniformity of the field requires a different analysis method. Since the maximum principal strain direction varies, the cell orientation angle with respect to a single arbitrary axis are inappropriate if cells from different locations on the membrane are to be included in the same analysis. This is especially important when the gradient direction is considered in the description of cell orientation. In the sections that follow, the orientation of the cell normal is computed against either the local maximum strain orientation or against an empirical model that we have developed that considers both the local strain and its gradient. The definitions of the different angles used in the analysis are summarized in Fig. 3.1c.

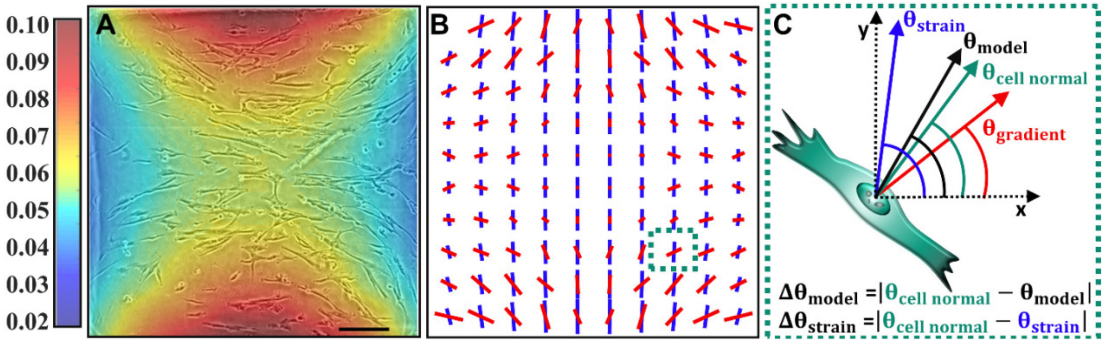

Figure 3.1 Description of the non-uniform anisotropic strain field and of the angle definitions. a) Color map of the experimentally determined maximum principal strain amplitude $\varepsilon_1(x,y)$ across the 1.6 mm wide square membrane. A phase contrast image of adhered HFF cells on the microdevice membrane is overlaid on the strain map. The cells have been subjected to 11 hours of vertical cyclic stretching at 1 Hz. They do not simply reorient away from the strain direction (mainly vertical as seen in **b)** but they rather largely follow lines of equal strain amplitude. Note that the presented area is cropped slightly to exclude the potential edge effects (8% wide on each side). The scale bar is 350 μm. **b)** A representation of the amplitude and direction of the maximum

principal strain (blue lines) and its gradient (red lines) is displayed. **c)** Scheme of a fictional cell located in the bottom right corner of the device (dotted square shown in **b)** presenting the definitions of the angles used in the analysis. The angles $\Delta\theta_{\mathrm{model}}$ and $\Delta\theta_{\mathrm{strain}}$ are used to construct the reorientation histograms. Note that the relative weight of $\theta_{\mathrm{gradient}}$ and θ_{strain} to obtain θ_{model} depends on their relative amplitude, as explained in the main text.

3.3.2 CELL REORIENTATION DEPENDS ON BOTH THE STRAIN AND THE STRAIN GRADIENT FIELDS

Multiple experiments were performed to investigate the reorientation behavior of HFF cells. Fig. 3.1a shows a representative image of adhered cells on the membrane embedded in the microdevice after 11 hours of cyclic stretching with the non-uniform strain field. The cells were initially randomly oriented (not shown), and after cyclic stretching they were approximately perpendicular to the maximum strain direction in the region of constant strain (central region). Interestingly, outside of the central region, the cell orientations approximately followed the underlying color map, which represents the principal strain amplitude profile. More specifically, they appeared to align preferentially along lines of equal strain amplitude. In other words, they seemed aligned perpendicularly to the strain gradient direction, especially in the region of strong gradient amplitude (rapid change of color).

Fig. 3.2a-c (excluding the inset of a) present the histograms of the angle differences between the cell normal directions and the principal strain directions ($\Delta\theta_{\mathrm{strain}}$) considering three different regions of the membrane. The full membrane surface is examined in Fig.3.2a while only the regions of high strain amplitude (> 7%) are analyzed in Fig. 3.2b, which correspond to the vacuum pump neighboring regions (orange and red regions in Fig. 3.1a). The histogram of Fig. 3.2a confirms that the cells largely reoriented perpendicularly to the strain direction and the larger degree of alignment observed in Fig.3.2b shows that this reorientation is sensitive to the strain amplitude. In contrast, Fig. 3.2c considers regions of simultaneously high gradient amplitude (> 7% mm^{-1}) and low strain amplitude (< 5%) (green and turquoise regions near the corners of Fig. 3.1a). Under these conditions, a decrease in cell normal alignment with the strain direction is observed, suggesting that this description is incomplete. In particular, in these regions, the cell normal directions seem to depart from the principal strain directions and align partly with the gradient directions. It should be noted that in our device, the principal strain and gradient directions are largely decoupled, allowing this observation.

In an attempt to describe the cell reorientation under such a complex strain field, a simple empirical model was used. Building on our results and recurrent observation that cells seem to align largely with equal strain amplitude lines, we incorporate the following ideas: i) cellular avoidance of stretching (strain) in regions of strong applied strain amplitude and ii) cellular avoidance of strain gradient in regions of strong applied gradient amplitude (identified in this paper). To take into account these effects, we consider the simplest empirical model possible, namely a linear combination of $\theta_{\mathrm{strain}}(\mathrm{x},\mathrm{y})$ and $\theta_{\mathrm{gradient}}(\mathrm{x},\mathrm{y})$ weighted by the strain amplitude $\varepsilon_1(\mathrm{x},\mathrm{y})$ and the strain gradient amplitudes $|\nabla\varepsilon_1(\mathrm{x},\mathrm{y})|$, respectively. To investigate our data, the following equation is thus suggested to express the preferential orientation of the cell normals:

$$\theta_{\mathrm{model}} = \alpha\left[\varepsilon_1\theta_{\mathrm{strain}} + \beta|\nabla\varepsilon_1|\theta_{\mathrm{gradient}}\right] \quad (16)$$

where $\alpha = (\beta|\nabla\varepsilon_1| + \varepsilon_1)^{-1}$is the normalization factor including the weighting parameter β. Fig. 3.2d presents the histogram of the angle differences $\Delta\theta_{\mathrm{model}}$ (differences between $\theta_{\mathrm{cell\ normal}}(\mathrm{x},\mathrm{y})$ and $\theta_{\mathrm{model}}(\mathrm{x},\mathrm{y})$), considering again the regions of high gradient and low strain amplitudes (same areas as in Fig. 3.2c). The parameter β was optimized here (and kept constant for all subsequent analysis) by minimizing the mean squares $\sum_{n=1}^{N}\Delta\theta_{\mathrm{model}}{}_n^2/\mathrm{N}$, considering the data from six distinct stretching experiments. Importantly, the optimal β value remains similar (within ~ 13%) whether we consider the full membrane or the regions of interest in 2D. Interestingly, while the model provides a slight improvement over the full membrane (Fig. 3.2a inset), it is not comparable to the excellent improvement obtained from Fig. 3.2c to Fig. 3.2d. The reason is that the gradient is relatively low over a large portion of the membrane, where the strain is thus dominant, resulting in a dilution of the gradient effect. In the regions where the gradient effect is most important (Fig. 3.2c,d), the experimental and "predicted" orientations are in good agreement only when the model is considered. It is interesting to note that for the regions considered in Fig. 3.2d, the average contributions of the strain and strain gradient (considering the optimal β value) are respectively 63% and 37%. This confirms the significance of the effect of the strain gradient on the cellular reorientation in our strain field. Finally, for Fig. 3.2a-d, the controls were randomly oriented.

3.3.3 CELL ALIGNMENT WITH THE GRADIENT DIRECTION DEPENDS ON THE GRADIENT AMPLITUDE

We now further assess the dependence of the cell reorientation on the strain gradient in order to test its accuracy. First, Fig. 3.3a indicates that as the strain amplitude $\varepsilon_1(\mathrm{x},\mathrm{y})$ increases, the mean

cell normal direction increasingly aligns with the principal strain direction (showed by a decreasing $\Delta\theta_{\mathrm{strain}}$value). A similar relationship for the strain gradient is successfully reported in Fig. 3.3b. It indicates that as the strain gradient amplitude $|\nabla\varepsilon_1(\mathrm{x},\mathrm{y})|$ increases, the mean cell normal direction increasingly aligns with the gradient direction (showed by a decreasing $\Delta\theta_{\mathrm{gradient}}$ value). To verify that the latter dependency cannot be attributed to a correlation between the strain and the strain gradient fields, two additional relationships were extracted. First, the mean $\Delta\theta_{\mathrm{strain}}$ was plotted as a function of the gradient amplitude$|\nabla\varepsilon_1(\mathrm{x},\mathrm{y})|$ (Fig. 3.3c). Second, the average angle difference between the strain and the gradient directions, $<\theta_{\mathrm{strain}}-\theta_{\mathrm{gradient}}>$, was also plotted as a function of the gradient amplitude (Fig. 3.3c inset). In both cases, the unambiguous trend observed in Fig. 3.3b is not reproduced, indicating the genuine role of the gradient. In other words, the increased alignment of the cell normal with the strain gradient direction observed in Fig. 3.3b cannot be explained by the relationship between θ_{strain} and $\theta_{\mathrm{gradient}}$. Importantly, for strain gradient amplitudes greater than ~2% mm^{-1}, the mean $\Delta\theta_{\mathrm{gradient}}$ in Fig. 3.3b is systematically lower ("better") than $<\theta_{\mathrm{strain}}-\theta_{\mathrm{gradient}}>$ (Fig. 3.3c inset). To our knowledge, this is the first reported demonstration of cell alignment with the underlying strain gradient.

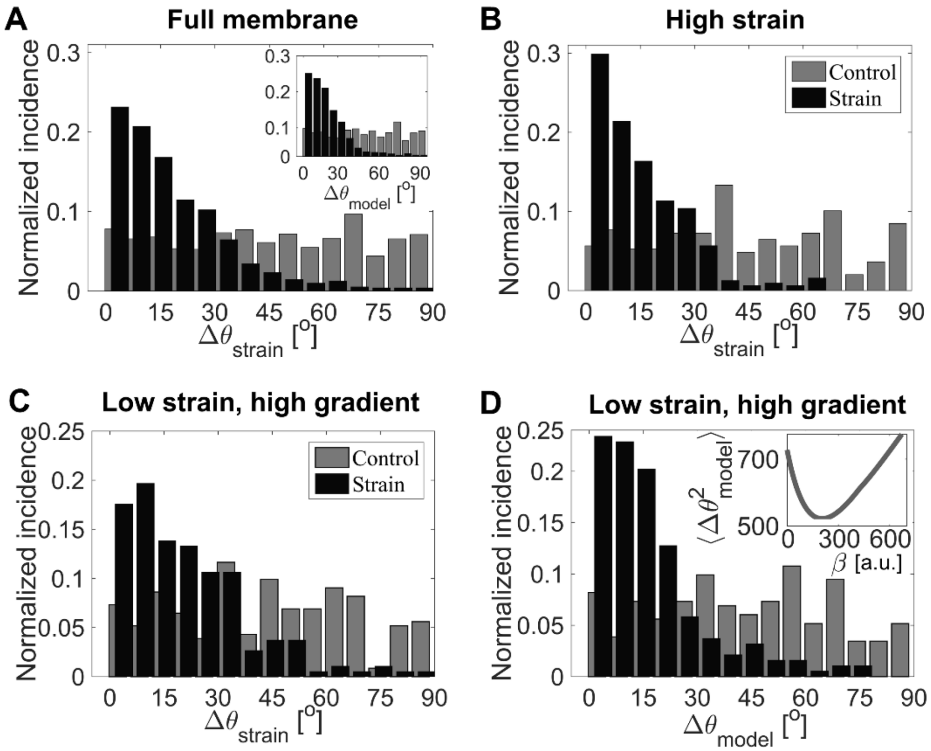

Figure 3.2 Reorientation analysis of the HFF cells after 11 hours of cyclic stretching. Normalized incidence histograms of $\Delta\theta_{strain}$ (**a)** to **c)**) and $\Delta\theta_{model}$ (**d)**, and inset of **a)**) for both unstretched controls and stretched experiments. All the cells are included in **a)** (main figure and inset), only the cells located in the regions of high strain amplitude (> 7%) are included in **b)**, and only cells located in the regions of simultaneously high gradient amplitude (> 7% mm^{-1}) and low strain amplitude (<5%) are included in **c, d)**. It should be emphasized that for all the histograms, the cell normal angles are not reported with respect to the fixed x-axis, but rather with respect to the underlying maximum principal strain directions or to the empirical model directions, as specified. The inset of **d)** shows the optimization curve of the β value via mean square minimization of the $\Delta\theta_{model}$ values. Each histogram comprises the combination of 6 unstretched control experiments as well as the combination of 6 cyclically stretched experiments. The number of cells analyzed in each histogram is n_{strain}=1078 and $n_{control}$=1244 for **a)**, n_{strain}=132 and $n_{control}$=200 for **b)**, n_{strain}=181 and $n_{control}$=187 for **c,d)**. Fig. A.2 of the Appendix A explicitly shows the different regions used to generate Fig. 3.2a-d, and table A.1 summarizes the number of cells analyzed in each case for both the control and stretched experiments.

3.3.4 MYOSIN-II ACTIVITY INHIBITION SUPPRESSES CELL ALIGNMENT WHILE ITS PROMOTION DOES NOT IMPACT THE FINAL REORIENTATION

To assess how myosin-II activity affects the orientation response of HFF cells in a non-uniformly strained microenvironment, experiments were performed in which calA or blebbistatin treatments were applied immediately before activating the substrate cyclic stretching [174,188,189]. Fig. 3.4a shows that upon stimulation of myosin-II contractility through inhibition of myosin light chain phosphatase (calA), the cells reoriented in a similar fashion to their untreated counterparts

(DMSO, strain, Fig. 3.2a, inset), with no significant difference. Conversely, the inhibition of myosin-II contractility largely prevented stretch-induced alignment under cyclic stretching, as shown by the near-random distribution of cell orientations displayed in Fig. 3.4b. It should be reiterated that the weighting parameter β employed in the orientation analysis of Fig. 3.4 was not re-optimized. However, it is very interesting to note that an optimization of the β value on the calA-treated cells of Fig. 3.4a would result in a β value that defers by only ~ 8%.

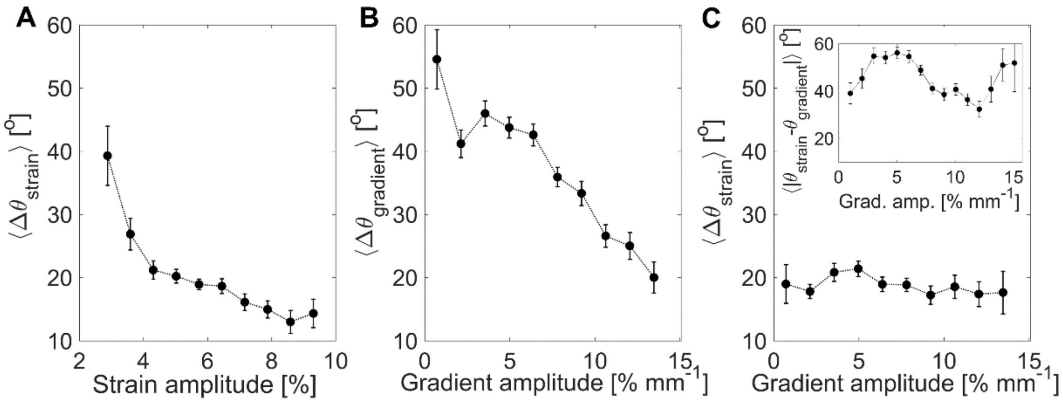

Figure 3.3 Dependence of the cell reorientation direction on the strain amplitude and strain gradient amplitude. The data were binned in equal amplitude range sizes and the error bars represent the standard error of the mean within each bin. **a)** Mean angle difference between the experimental cell normal orientation and the principal strain direction as a function of the strain amplitude. **b)** Mean angle difference between the experimental cell normal orientation and the strain gradient direction as a function of the strain gradient amplitude. **c)** Mean angle difference between the experimental cell normal orientation and the principal strain direction as a function of the strain gradient amplitude. The inset shows the average angle difference between the strain and the gradient directions as a function of the gradient amplitude. The number of cells analyzed is n=1078.

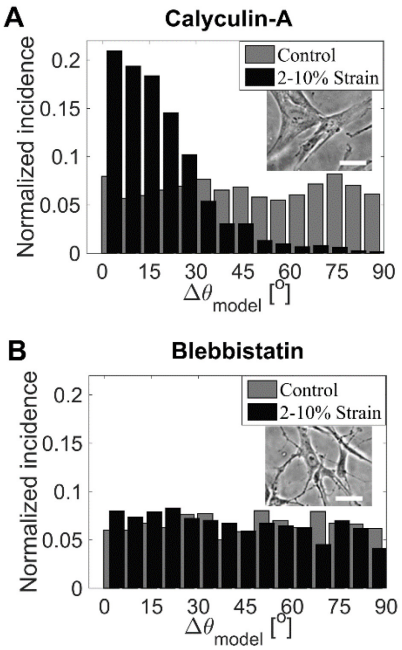

Figure 3.4 Effect of myosin-II activity on HFF reorientation after 11 hours of cyclic stretching. Normalized incidence histograms of $\Delta\theta_{\mathrm{model}}$ for cells treated with calA (2 nM) in **a)** and blebbistatin (10 μM) in **b)**. Each histogram comprises the combination of 6 unstretched control experiments as well as the combination of 6 cyclically stretched experiments. The number of cells analyzed in each histogram is n_{strain}=1231 and $n_{control}$=1255 for **a)**, and n_{strain}=1319 and $n_{control}$=1091 for **b)**. The insets diplay phase constrast images of representative cells from the corresponding experiments. Scale bars are 100 μm.

3.3.5 FOCAL ADHESIONS REORIENT ALONG THE CELL ELONGATION DIRECTION UNDER CYCLIC STRETCHING AND THEIR REORGANIZATION IS MYOSIN-II DEPENDENT.

To gain insight on the cellular reorientation mechanism, the behavior of the FA complexes was also assessed since they sense and transmit to the cell the physical signals from the extracellular matrix. Fluorescence images of a representative stretch-induced reoriented cell inside a microdevice are displayed in Fig. 3.5e-f. It can be seen that the actin filaments were largely aligned with the cell elongation direction, as expected [39,142,177]. This qualitative observation applied to all untreated and calA-treated cells, but not to those treated with blebbistatin, in which case the alignment was less obvious. The FA protein vinculin, shown in Fig. 3.5f, also exhibited strong alignment with the cell direction. This is quantitatively assessed in Fig. 3.5a, in which the FA normals are seen to predominantly follow θ_{model} directions, in accordance with the cell elongation directions (Fig. 3.2a, inset). An equivalent FA orientation behavior was observed for the cells with increased myosin-II contraction (calA, Fig. 3.5b), but little preferential alignment was found in the case of those with decreased contractility (blebbistatin, Fig. 3.5c). Interestingly,

this is also reflected in the FA density (Fig. 3.5d). In comparison to the untreated cells, there was a significant loss of FAs in blebbistatin-treated cells, but not in those treated with calA. Finally, in all cases, the FA density was slightly strain-dependent; more specifically the applied stretching forces appeared to promote FA assembly.

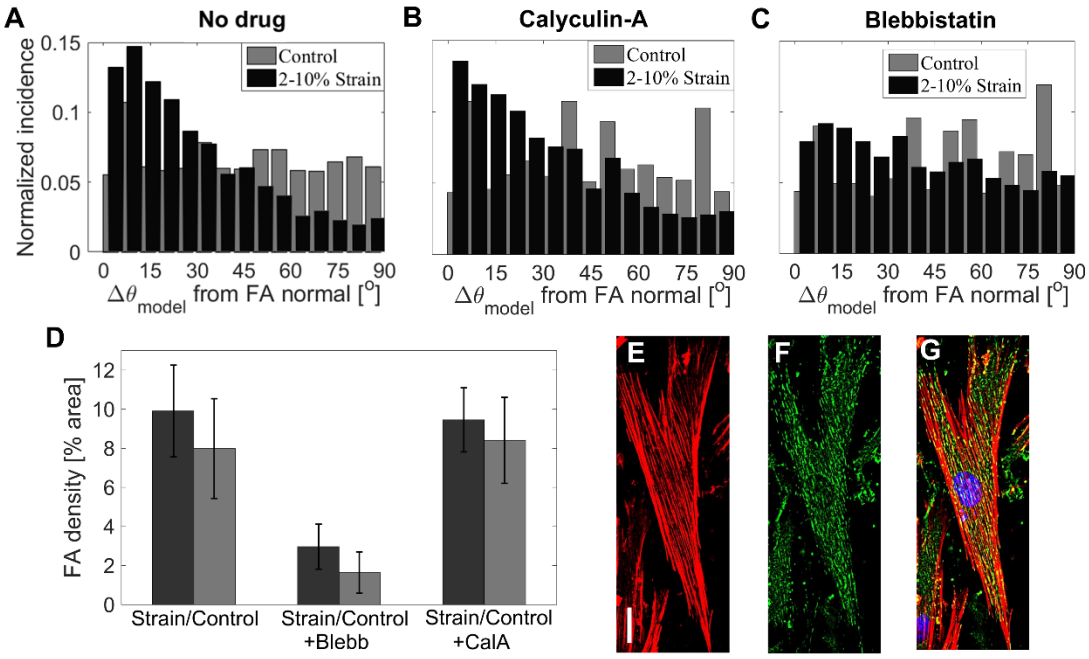

Figure 3.5 FA reorganization after 11 hours of cyclic stretching. Normalized incidence histograms of the angle difference between each FA normal and the direction θ_{model}, for cells without treatment in **a)**, with calA in **b)**, and with blebbistatin in **c)**. **d)** Average FA densities among the cells under six different cases (the error bars represent the standard deviation). Statistical differences were found between strain and control experiments for all 3 treatments, as well as between treatments (unpaired t-tests, $p < 0.05$), except between calA and DMSO (unpaired t-tests, $p > 0.05$). The number of FAs analyzed in each histogram is n_{strain}=7568 (61 cells) and $n_{control}$=2607 (35 cells) for the drug-free condition in **a,d)**, n_{strain}=5164 (71 cells) and $n_{control}$=4119 (44 cells) for the calA condition in **b, d)**, and finally n_{strain}=1904 (62 cells) and $n_{control}$=889 (29 cells) for the blebbistatin condition in **c, d)**. Table A.2 of the Appendix A specifies the number of FAs analyzed in each case for both the control and stretched experiments. **e,f)** Immunofluorescence images of a HFF cell following 11 hours of cyclic stretching along the x-axis (1 Hz) on the fibronectin-coated PDMS membrane embedded in the microdevice. Immediately after the stretching process, the cells were fixed and stained for actin filaments (red) in **e,g)**, vinculin (green) in **f,g)**, and DNA (blue) in **g)**. The images from the laser scanning confocal microscope were post-processed with ImageJ to perform the z-projection, background removal, and contrast enhancement. The scale bar is 25 μm.

3.4 DISCUSSION

3.4.1 CELLS AVOID LARGE POSITIVE AXIAL STRAINS

Our results show that in the region of constant strain amplitude and direction (central region, see Fig. A.2, Appendix A), the cells reoriented approximately perpendicularly to the stretching direction, which is in general agreement with a large body of work performed mainly with uniform strain amplitude devices[30,34–39,44,68]. Theoretical models have been proposed to describe the reorientation response of cells to cyclic stretching. For high frequency stretching (~1 Hz) and moderate strain amplitudes (~5-15 %), different experiments and models suggest several possible preferential orientations. Various studies corroborate models in which the preferential cell orientation is the minimum absolute strain direction, i.e. the direction minimizing length changes along the major cell body axis[10,17,19]. Building upon previous work[68], Kaunas *et al.* proposed a model with this predicted preferential orientation, based on the premise that the disassembly rate of the stress fibers should be the smallest along this direction[190]. Considering a simplified model where FAs are treated as catch bonds destabilized by cyclic stretching, Chen *et al*. arrived at similar conclusions with respect to the preferential orientation[171]. On the other hand, Safran and De developed a comprehensive model based on effective free energy considerations and in which cells are treated as force dipoles[169]. Their model is adaptable to allow for two possible preferential orientations: minimum absolute strain direction or minimum stress direction. In the latter case, the corresponding preferential orientation is perpendicular to the maximum principal strain direction, rather than along the minimal absolute strain direction. Based on empirical observations, Neidlinger-Wilke et al. had also proposed previously that cells should preferentially reorient along this direction[36] (even if this requires undergoing axial compression), and several experimental studies corroborate such alternative predictions[30,37–39]. Finally, Livne et al. recently proposed a model based on dissipative relaxation of stored elastic energy which was highly successful in explaining their experimental results[142]. Importantly, since uniaxial stretching of a deformable membrane generally results in orthogonal compression, the non-zero Poisson ratio greatly impacts the predicted preferential orientation in many of the models noted above. In our case, the membrane's Poisson ratio was approximately 0.5 and so was the actual ratio of X-compression over Y-stretching in the central portion of the membrane. The resulting minimum absolute strain direction (zero-strain direction) is 35^{o} with respect to the x-axis, which is not the preferential orientation we observed (see Fig. A.3 (right) of the Appendix A). The preferential orientation predicted by the model of Livne et al. is ~30^{o}, which is also markedly different from

what we observed. We rather observed that the fraction of cells subjected to an approximately uniform strain field in our device preferentially oriented themselves perpendicularly (0^o) to the maximum principal strain direction. Interpreted from the point of view of the model by Safran and De[169], our results thus suggest that HFF cells stretched in our device preferentially align along the minimal stress direction rather than that of the zero strain. The lack of consensus concerning the exact preferential orientation under uniform strain field suggests a dependence on the cell type and experimental conditions. Finally, we note that in general, the broadness of the observed orientation distributions in cyclic stretching experiments can be attributed to stochastic contributions associated with the statistical nature of the chemical reactions involved in the mechanosensing process and variations in the cell population[118,169].

The extent of cell alignment in our experiments was found to increase with the amplitude of the strain (Fig. 3.3a), as reported previously for human fibroblasts[36,118] and for other cell types[35,41,191]. A feature of this relationship identified in previous studies is the presence of a strain amplitude threshold, under which no significant alignment is observed. It was reported to be ~4 % for human fibroblasts[36]. This behavior is in qualitative agreement with our data, although Fig. 3.3a suggests a slightly lower threshold. A more precise threshold analysis would not be relevant here because of the strain gradient interplay.

3.4.2 CELLS SEEK TO AVOID STRAIN GRADIENT

The cell reorientation behavior in a non-uniform strain field has been investigated previously, but other studies failed to show a dependence upon the strain gradient. This can be explained by the low gradient amplitudes applied, the gradient direction being systematically along that of the strain, or the absence of comprehensive analyses of cellular reorientation with respect to the strain gradient field. In our case, the successful observation of this effect was made possible by the combination of biologically relevant strain gradient amplitudes (0 to 14% mm^{-1}) and the complex strain field geometry at a scale similar to cell sizes in which the strain and the gradient directions are decoupled. Importantly, as shown above (Fig. 3.1a, 3.2d, and 3.3b), in regions of large gradient amplitudes, cells tended to align perpendicularly to the gradient direction. This observation suggests that cells respond to the gradient to avoid being subjected to different strain amplitudes throughout its different adhesion sites. This apparent avoidance of the strain gradient is analogous to the previously established avoidance of length increases (or changes) during cyclic

stretching. Interestingly, cell reorientation is dependent on the strain gradient amplitude and the strain amplitude, respectively shown in Fig. 3.3b and 3.3a. These relationships are reflected in the choice of the simple empirical model.

It is worth mentioning previously reported observations enabled by different devices producing non-uniform strain fields. In particular, the use of uniaxial devices allowed the generation of membrane strain gradients, which were used to demonstrate the influence of the strain amplitude under static stretching[42,43]. However, in these cases, the strain gradient was oriented along the stretching direction, preventing investigation of its influence on cell orientation. In other instances, radially deformable membranes producing radial strain gradients showed that under cyclic stretching, cells orient themselves perpendicularly to the principal strain direction[179] and the alteration of mRNA expression is strain amplitude dependent[139,181]. Interestingly, while no gradient-dependent reorientation was observed, likely due to the device's radial symmetry, gradient-dependent mRNA expression was observed (which is compatible with our results). Also relevant to the present study, Morita *et al.* studied human bone marrow mesenchymal stem cell reorientation in a non-uniform cyclic strain field[41]. The strain gradient was on the order of 0.5 $\%mm^{-1}$, and it was mainly in the stretching direction. They methodically analyzed the potential dependence of the cell reorientation on the strain gradient but found none under their conditions. Finally, Ohashi *et al*. employed a cyclically stretched membrane exhibiting a very large gradient (200% mm^{-1}) in the stretching direction to study stress fiber formation[180]. Interestingly, it was found that variations in the local development of intracellular stress fibers are associated with variations in applied strain amplitude underneath this cell (local response).

It must be noted that the cell alignment response to strain gradient found in our study is distinct by its non-local manifestation. In general, the capacity for a body to sense a strain gradient requires it to spatially locate and compare different strain amplitudes. Although speculative, we hypothesize that the global cellular response to strain gradient implies that cells are be able to pinpoint this information at each adhesion site, and coordinate these signals (strain amplitude, strain direction, and location under the cell) to determine optimal alignment. In this context, the cell exhibits a coordinated and integrated global response that is partially based on the spatial variation in strain amplitudes sensed locally in different cell areas. This is particularly easy to observe in our device because at the scale of a single cell, both the gradient and strain directions are relatively constant, only the strain amplitude varies significantly.

3.4.3 CONTRACTILITY IS CENTRAL IN THE CYCLIC STRETCHED-INDUCED CELL ALIGNMENT

FA analysis and drug treatment experiments were also performed in this study. The prestress condition and actomyosin contractility are directly involved in cell reorientation[168,174,192]. Therefore, reagents affecting the actomyosin cytoskeleton are most likely to strongly impact stretch-induced cellular reorientation[173]. Two such reagents are calA and blebbistatin, which promote[188] and inhibit[174,189] contractility through the modulation of myosin-II activity, respectively. Our observation is similar to that of Zhao *et al.*[174] who reported a high degree of perpendicular reorientation among the calA-treated fibroblast cell population. In their case, this response was faster than without the pharmacological treatment, but their trends converged after several hours. In our case, after 11 hours of stretching, the reorientation responses of the calA-treated cells and the untreated cells were not significantly different. It was also previously reported that a sufficient concentration of blebbistatin largely suppresses the reorientation of 3T3 fibroblasts cells and stress fibers under cyclic stretching[173,174]. This behavior, involving stress fiber tension reduction, is in qualitative agreement with our results, which supports the notion that contractility is central to cellular reorientation.

3.4.4 THE REORIENTATION OF FAS IS PRIMARILY DRIVEN BY INTERNAL FORCES UNDER OUR CONDITIONS

The cell machinery enabling the sensing and transduction of extracellular mechanical cues comprises not only the cytoskeletal network but also the FAs; the two are intrinsically connected[59,176]. The investigation of FA density and orientation under cyclic stretching, following a change in myosin-II activity, can provide insight on their roles in cellular reorientation. Our results show that the FAs mostly reorient perpendicularly to the strain direction upon cyclic stretching, in agreement with previously reported studies[170,177,193]. As well, we quantitatively show that FAs align parallel to the actin stress fibers, since the later mostly follow cell orientation, as expected[142,194]. On a broader level, it was proposed that the FAs elongate by growing in the direction of a pulling force[195]. This suggests that in our experiment, the primary forces driving FA reorganization are internal (rather than substrate stretch); i.e. they are mainly associated with actin assembly and actomyosin contraction.

3.4.5 CONTRACTILITY AFFECTS FA DENSITY AND REORIENTATION BEHAVIOR

We found that under cyclic stretching, the inhibition of cell contractility via blebbistatin treatment resulted in the inhibition of FA alignment and a significant reduction in FA density. The blebbistatin-induced loss of FA density is in agreement with a previously reported study[176]. Our results further suggest the strong dependence of the FA fate on the actin-induced forces. Moreover, we observe a small – but statistically significant – effect of the substrate strain itself on the FA density following 11 hours of cyclic stretching (for all three contractility conditions). In contrast, a larger increase in FA density, induced by stretching, has been reported for other cell types when studied on different time scales[196–198]. Furthermore, calA (without stretching) was previously shown to increase FA density but only on a short time scale[199]. This is in contrast with the absence of significant difference in FA density observed here between the calA-treated and non-treated cells, when studied over our much longer time scale (11 hours). Overall, our results highlight the fact that FAs are not only implicated in the mechanosensing process, but their behavior is also an integral part of the mechanoresponse.

3.4.6 POTENTIAL MECHANISMS INVOLVED IN STRAIN GRADIENT SENSING

Forces acting on the ECM-integrin-cytoskeleton complex are believed to be sensed via numerous mechanisms[2]. In the context of uniform strains, it has been shown that forces exerted by the ECM on the cell can promote cytoskeleton and FA assembly and reorganization. The exact mechanisms for tension-mediated FA maturation upon mechanical stimulation are not fully understood, but they are known to involve diverse protein recruitment and integrin clustering[200]. A specific example may include the reinforcement of the integrin-actin linkage by unfolding specific talin domains via stretching, thus allowing vinculin binding[201]. This mechanism was recently revealed to be involved in force transmission and transduction in the context of substrate stiffness sensing through the actin-talin-integrin-fibronectin clutch[49,202]. Stabilization of integrin adhesions through the vinculin recruitment induced by myosin-dependent tension has also been shown via FAK and SRC-mediated phosphorylation of paxillin[200]. More recently, in fibronectin-based microenvironments, mechanosensing is believed to involve α_V-class integrins which were shown to play a role in the structural cell adaptation to forces[203]. Interestingly, the expression of $\alpha_V\beta_3$ was specifically shown to be upregulated in cyclically stretched in endothelial cells[198]. Moreover, $\alpha_5\beta_1$ was demonstrated to enable force generation and the cooperation of the latter with α_V-class integrins was shown to enable rigidity sensing[203]. We note that the mechanosensing machinery

enabling strain sensing bears similarities with that associated with stiffness sensing. Importantly, in both cases, stiffness- or stretching-induced signal transduction cascades activate the RHO-ROCK pathways which in turns regulate the myosin light chain phosphorylation and thus enable tension and traction force generation via the actomyosin cytoskeleton[2].

Through the above molecular mechanisms, cells are able to probe and respond to the spatial profile of the ECM stiffness, possibly at the scale of the individual FAs[204] and thus with micron precision. This enables cells to sense stiffness gradient and undergo gradient-guided migration (durotaxis)[187,205]. In a similar way, it was previously shown that cells are sensitive to the underlying strain profile at the sub-cellular scale[180], and thus again possibly at the scale of individual FAs. Although our data suggest that the preferential alignment of the FAs is affected by both the strain and the strain gradient properties of the ECM, it is difficult to know if the latter behavior results from the direct guidance of the ECM external force onto the FAs individually, or if it rather results from the action of the internal cytoskeleton tension adapting to the external strain gradient.

We speculate that the exact underlying mechanisms that ultimately govern strain-gradient sensing and avoidance are likely highly similar to the pathways identified above. However, we note that these pathways are highly dependent on the cell type, ECM and stretching conditions. Therefore, it is currently beyond the scope of this study to attempt to generalize a specific mechanism. Following the logic of Tse and Engler[205] in the context of stiffness gradient sensing, we suggest that the strain gradient sensing process involves the creation intracellular signaling gradients such as gradients of RHO-ROCK activity. Another possibility would be a gradient of talin-mediated force transmission resulting from spatial variations in the duty cycles of vinculin-binding site exposition across the cell, directly correlating with different stretching amplitudes. We hypothesize that such signaling gradients, together with direct variation of force imposed across the cell, result in increased cytoskeleton tension gradients within the cell. This will be explored in future work utilizing the framework we have now presented and established in this study. It is well established that cells seek to maintain mechanical homeostasis under changing ECM properties[2]. Therefore, gradient avoidance suggests that cell homeostasis also includes a certain degree of spatial tension uniformity across the cytoskeleton, possibly at the expense of deviating from the preferential orientation determined by the average strain direction.

3.5 CONCLUSION

In summary, cyclic stretching experiments under diverse conditions were performed in micro-fabricated devices exhibiting a unique highly non-uniform strain field. These experiments revealed that fibroblast cells seek to avoid strain gradients similarly to the way they avoid stretching. The degrees of these avoidances are shown to depend on the strain gradient amplitude and the strain amplitude respectively. Importantly, by identifying the strain gradient as a subtle mechanical cue, our results demonstrate that cells can integrate diverse physical signals simultaneously and exhibit a coordinated response. Furthermore, we demonstrated that under non-uniform strain field, human fibroblast FAs also reorient in a similar fashion to the cells, and that their density is affected by stretching forces. Finally, myosin-II contractility was shown to impact FA and cell reorientations, since its inhibition prevented the alignments of both and yielded a reduced FA density.

Our work reveals that strain gradients are mechanical cues capable of influencing and modulating global cellular organization and orientation. This opens a new line of investigation regarding the role of the strain gradient in regulating certain cell functions and how this regulation can be compromised by cell or cell matrix defects. This study paves the way to a better understanding of certain in vivo pathologies which may lead to new pharmaceutical approaches, in addition to providing new insights on the fundamental interactions between the cells and their microenvironment.

3.6 MATERIALS AND METHODS

3.6.1 MICRODEVICE GEOMETRY AND FABRICATION

The cells were immobilized on a thin suspended PDMS (Sylgard184, Ellsworth Adhesives Canada Corporation, Stoney Creek ON, Canada) membrane and cyclically stretched within microdevices which have a modified design similar to the one we previously reported[44]. The chip size and geometry allow for high strain gradient amplitudes (from 0 to 14 $\%mm^{-1}$) to be generated on the membrane, while keeping the strain amplitude relatively low (from 2 to 10%, see Fig. 3.1a,b). The unique strain field pattern was achieved by stretching a 1.6 mm x 1.6 mm x 10 µm membrane with four fixed boundaries, using 4 vacuum chambers, all embedded in the PDMS chip. The action of the vacuum chambers deforms the cell chamber side walls (120 µm thick) in which the membrane is anchored, allowing the stretching motions. The device comprises three layers

consisting in a suspended membrane inserted between the micro-patterned top and bottom parts. The membrane's stiffness is estimated to 0.5 MPa based on previously characterized PDMS substrates prepared under similar conditions to ours[206,207]. Additional fabrication details are provided in the Appendix A (see Fig. A.1).

3.6.2 MEMBRANE STRAIN FIELD CALCULATION

The non-uniform nature of the strain field requires a detailed point-by-point characterization to accurately analyze the cell reorientation based on the local field applied to each cell. Fluorescent beads (FluoSpheres, 200 nm, Invitrogen, CA, USA) were incorporated in the floating 10 µm thick membrane for precise strain field characterization. The full stretching motion of the substrate was divided in 10 frames (by applying different pressure in the vacuum chambers) and imaged with an EPI fluorescence microscope. The beads displacements were tracked with a homemade Matlab program in which the Green strain matrix elements were subsequently calculated for each initial bead position. From these, two principal strain directions and amplitudes can be extracted. In such coordinate systems, the shear strain is zero. First, the maximum principal strain $\boldsymbol{\varepsilon_1}(x,y)$ is associated with the direction of maximum stretch at a given membrane position. Second, the minimum principal strain $\boldsymbol{\varepsilon_2}(x,y)$ (with direction that is orthogonal to that of $\boldsymbol{\varepsilon_1}(x,y)$), is associated with the direction of minimum stretch (or maximal compression in the case of negative $\boldsymbol{\varepsilon_2}$). Note that $\boldsymbol{\varepsilon_1}(x,y)$ is of primary interest here since it largely dominates $\boldsymbol{\varepsilon_2}(x,y)$ across the membrane. The gradient of $\varepsilon_1(x,y)$ was then calculated to produce the gradient amplitude $|\nabla\varepsilon_1(x,y)|$ and gradient angle $\theta_{\mathrm{gradient}}(x,y)$ maps (see Fig. 1 b). Additional details on the strain calculations are provided in the Appendix A.

3.6.3 EXPERIMENTAL PROCEDURES

The assembled microdevices were air-plasma treated (Glow Research, Tempe, AZ, USA) for 5 minutes at 70 W prior to sterilization with 70% ethanol for 5 minutes. After flushing the ethanol with autoclaved phosphate buffered saline (PBS) solution, the membrane was functionalized for 4 hours at 37°C with a solution of fibronectin 10 µg/ml of HEPES-buffered salt solution (HBSS; 20 mM HEPES at pH 7.4, 120 mM NaCl, 5.3 mM KCl, 0.8 mM $MgSO_4$, 1.8 mM $CaCl_2$ and 11.1 mM glucose). A solution of suspended cells in the culture medium with a density of $5x10^4$ cells/ml was injected into the 5.2 µl device's cell chamber. The devices containing the cells were left in a standard incubator for 15 hours to let the cells attach and spread on the fibronectin-coated

membrane to achieve a cell density of ~ 200 cells/chamber (chamber size: 1.6x1.6 mm^2). The well adhered cells were then cyclically stretched for 11 hours at 1 Hz by activating the vacuum pumps while keeping the microdevice in the incubator during the whole experiment. No significant cell loss was observed upon stretching activation. The stretching time of 11 hours was chosen to be well above the characteristic time for the strain-induced reorientation of fibroblasts under our conditions[34] and the stretching frequency was chosen for its physiological relevance[12,208–210]. Cell density only changed slightly during the 11 hours of stretching. Importantly, the cell density of control and strain experiments were highly similar, ensuring that the observed differences are fully attributed to the strain field (no contribution from cell density discrepancy). The maximum strain amplitude field varies from 2% to 10% across the membrane, as depicted in Fig. 3.1a. A homemade Labview program controlled the maximum amplitude and frequency of the sinusoidal stretching wave form.

3.6.4 CELL PREPARATION AND DRUG TREATMENT

HFF cells (American Type Culture Collection (ATCC), Manassas, VA, USA) were cultured in Dulbecco's Modified Eagle's Medium (DMEM) supplemented with 10% fetal bovine serum (FBS) and 1% streptomycin/penicillin (Hyclone Laboratories, Logan, UT, USA). All cells were maintained at 37°C and 5% CO_2 in a standard incubator. The drugs (Sigma Aldrich, St. Louis, MO, USA) used were stored in dimethyl sulfoxide (DMSO) stock solutions and were added to the cells immediately before starting the stretching process. DMSO with the same final concentration (0.1%) was also added to the control experiments that were ran without pharmacological treatment. The drug treatments were applied to cells for the entire time of the experiments (11 hours). The final concentration of calA (2 nM) was based on previous studies[199,211,212] and by considering the long duration of the treatment (11 hours). More specifically, it was selected to avoid cell detachment from the substrate and rapid morphology changes (rounding) caused by the increased myosin-II contraction[213,214]. The final blebbistatin concentration (10µM) was chosen to enable relevant comparisons with related studies[177,212,215].

3.6.5 CELL FIXING, IMMUNOFLUORESCENCE STRAINING, AND IMAGING

Immediately after the 11 hours stretching process, the cells were fixed with 3.5% paraformaldehyde (PFA) and permeabilized and permeabilized with 0.5% TritonX-100. The cells enclosed in the microdevice were then kept in a cold PBS solution and imaged with a Nikon TiE inverted phase

contrast EPI microscope with a long working distance 10x objective in order to acquire the cell orientation data. Actin filaments were then stained with Phalloidin conjugated to Alexa Fluor 546 (Invitrogen) and the DNA with DAPI (Invitrogen). A monoclonal mouse anti-vinculin antibody and a rabbit anti-mouse IgG secondary antibody conjugated to Alexa Fluor 488 (Invitrogen) were used to stain vinculin. The details of the immunofluorescence staining protocols have been published previously[216,217]. These protocols have been adapted to suit the microdevice environment (see Appendix A for details). An upright laser scanning multiphoton confocal microscope with a long working distance 25x objective (NA=1.1) was employed to image the actin fibers, the nuclei, and the vinculin proteins.

3.6.6 CELL ORIENTATION AND FA ANALYSIS

The phase contrast images of the cells and the fluorescent images of the FAs were post-processed in ImageJ. The fluorescence images were first z-projected. To correct for background noise, a Fast Fourier Transform bandpass filter was applied to the phase contrast images, while the subtract background tool was employed for the fluorescent images. In both cases, binary images were then obtained from the adaptive threshold plugin which optimally captures the cell and FA morphologies despite the non-homogenous images intensities. Finally, the analyze particles tool was used for the extraction of the cell and FA positions, sizes, and orientations. More precisely, elliptical fits of the objects were performed and the determination of their major axis provided the cell and FA orientations.

A homemade Matlab program was developed to carry out the analysis. The cells and FAs located within 8% of the edges of the devices were excluded to discard edge effects. The orientation of each cell (or FA) was compared to the local strain parameters. More precisely, we computed the angle difference between the cell (or FA) normal and either the maximum principal strain angle or the model angle. The equation of the latter, which is presented in the Results section (equation (16)), includes the weighting parameter β. All the analysis was performed with the same β value after its initial optimization with the data set of Fig. 3.2d. To construct the histograms, the angles were converted to a 0 to 90^{o} range.

3.7 ACKNOWLEDGMENTS

This work was supported by individual Natural Sciences and Engineering Research Council (NSERC) Discovery Grants to M.G. and A.E.P. S.C-L. was supported by NSERC Postgraduate Scholarships-

Doctoral (PGS D). M.G. acknowledges support from the Ontario Ministry of Research and Innovation, and the Canada Foundation for Innovation (CFI). A.E.P. gratefully acknowledges generous support from the Canada Research Chairs (CRC) program.

CHAPTER 4 | TIME DEPENDENCE OF CELLULAR RESPONSES TO DYNAMIC AND COMPLEX STRAIN FIELDS

Manuscript submitted to *Integrative Biology* on April 20th 2018. The supplementary information is presented in Appendix B.

BioRxiv preprint server: https://doi.org/10.1101/286625

Authors: **Chagnon-Lessard, S**., Godin, M., Pelling, A.E.

Motivation/objective: Two distinctive cellular responses under a complex strain field have been identified in Chapter 3. Using our multi-axial microstretcher, we impose sudden changes in stretching direction to human fibroblasts in order to understand the temporal evolution of their stretching and gradient avoidance responses. We explore how the strain history can influence the overall cell behavior.

4.1 ABSTRACT

Exposing cells to an unconventional sequence of physical cues can reveal subtleties of cellular sensing and response mechanisms. We investigated the mechanoresponse of cyclically-stretched fibroblasts under a spatially non-uniform strain field which was subjected to repeated changes in stretching directions over 55 hours. A polydimethylsiloxane microfluidic stretcher array optimized for complex staining procedures and imaging was developed to generate biologically relevant strain and strain gradient amplitudes. We demonstrated that cells can successfully reorient themselves repeatedly, as the main cyclical stretching direction is consecutively switched between two perpendicular directions every 11 hours. Importantly, from one reorientation to the next, the extent to which cells reorient themselves perpendicularly to the local strain direction progressively decreases, while their tendency to align perpendicularly to the strain gradient direction tends to increase. We demonstrate that these results are consistent with our finding that cellular responses to strains and strain gradients occur on two distinct time scales, the latter being slower. Overall, our results reveal the absence of major irreversible cellular changes that compromise the ability to sense and reorient to changing strain directions under the conditions of this experiment. On the other hand, we show how the history of strain field dynamics can

influence the cellular realignment behavior, due to the interplay of complex time-dependent responses.

4.2 INTRODUCTION

The use of lab-on-a-chip[218,219] strategies allows mimicking complex in vivo physical cues and thus can facilitate the study of cellular behaviors in specific microenvironments. Cells in living organisms are constantly subjected to various mechanical forces such as compression and stretching (mechanical strains) due, for example, to muscle contractions, fluid pressure, pumping of the heart, and breathing. Such mechanical signals are known to be involved in the regulation of many fundamental biological processes such as cell migration, division, differentiation, and apoptosis[13,57,149,150]. Another example extensively studied to further our understanding of mechanotransduction processes is the cellular reorientation induced by cyclic stretching. More specifically, cyclically stretched cells were shown to exhibit elongation[118,220], alignment perpendicular to the stretching direction[26,30,34–36,39,142], and more recently fibroblasts were also demonstrated to exhibit strain gradient avoidance[45].

In vivo microenvironments are known to impose an array of time-dependent mechanical strains on cellular systems. For example, some studies have highlighted the role of complex mechanoresponse pathways related to embryonic development, or in articular cartilage development and degeneration. In these cases, not only are the mechanical forces known to play a key role[51,221,222], but they can be non-uniform and rapidly changing. There are also contexts in which the stiffness is perturbed locally, thus inducing strain gradients, for instance following the insertion of coronary artery stents[179]. In general, the complex microenvironment in which cells evolve in vivo gives rise to non-uniform, time-varying, anisotropic strain fields[139,184,185,223]. Importantly, in our previous work[45], we have clearly demonstrated that cells have an ability to sense and respond to both strain and strain gradients. Yet, the large majority of previous cyclic stretching studies have focused on stretch patterns with nearly-uniform strain amplitude and direction[30,34–36,39,220]. Although the present study does not aim to directly mimic a specific in vivo condition, it investigates the effect of biologically relevant strain fields with artificial discontinuous events, considering that sudden mechanical alterations can occur in living organisms. By studying cell responses to an unconventional sequence of mechanical cues we aimed to reveal subtle aspects of their mechanosensitivity. In particular, it is poorly understood if cells would continue

to exhibit the expected reorientation response if the strain field was repeatedly altered multiple times over the course of several days. Moreover, key insights on subtle cellular mechanisms can be gained by determining whether the cellular response to strain remains constant or if it changes over time with an increasing number of reorientation events.

This work investigates the influence of alternating the stretching axis of a complex strain field on the degree of cell alignment with the strain direction, the degree of cell alignment with the strain gradient direction, and the cell morphology. Sudden changes in stretching directions are achieved by employing a biaxial device which allows independent control over perpendicular stretching directions. In this context, we developed a highly versatile polydimethylsiloxane (PDMS) microfluidics device integrating an array of stretchable membranes. In particular, it can be made open-top at any point during a given experiment to facilitate imaging, circumventing disadvantages of typical microfluidic stretchers. Specifically, it enables complex staining procedures with minimal cellular perturbations, as well as near-diffraction limited imaging.

Here, we use human foreskin fibroblasts (HFF) as a model system as we have previously shown that they are acutely sensitive to both strain and strain gradients[45], thus being ideal for exploratory work. In the present study, we demonstrate that HFF cells possess the ability to reorient themselves when the imposed strain direction is changed, retaining this ability for at least five dramatic changes in strain direction. Our comprehensive analysis shows that the orientation distribution does vary with changes in stretching direction. Namely, we observed that the cells become progressively less oriented with the strain direction and conversely their alignment with the strain gradient direction improves as the experiment progresses. Furthermore, we show that this behavior is driven by a fascinating ability of these cells to respond to two separate, but simultaneous, mechanical cues over different time scales. Such complexity exists in vivo but is not widely reflected in fundamental studies as of yet due to the relatively few number of biaxial devices which allow for the production of complex strain fields. This study clearly highlights the importance of studying cellular behaviors in increasingly complex on-chip microenvironments.

4.3 RESULTS AND DISCUSSION

4.3.1 MICROFLUIDIC STRETCHER DESIGN

Microfluidic devices offer many advantages over manual methods by enabling automated on-chip sample handling capabilities, decreasing contamination risks, reducing reagent quantities, and

enabling high fabrication reproducibility[28]. In principle, they also have the potential to enable high-throughput screening experiments. An often-overlooked advantage of microstretchers over macrostretchers in certain studies is that they naturally produce non-uniform strain fields with biologically relevant strain gradients, while maintaining the strain magnitude to desirably low levels[224] (see Appendix B). This enables the study of mechanical cues which better mimics the complexity of the cell microenvironment in vivo. However, in applications where cells need to be cultured within the chip, such as for cyclic-stretching experiments, numerous experimental challenges[225,226] (nonuniform cell seeding, clogging, apparition of air bubbles, accumulation of undesired residues, etc) often impact the reliability of the experimental approach. Microfluidic devices also have disadvantages in the context of cell immunofluorescence microscopy. The first is the inherent difficulty in performing complex and sensitive straining procedures without compromising the integrity of the cell components (due to fluid shear stress[227]). The second issue is the reduction in imaging resolution which results from the optical aberrations introduced by the presence of PDMS in the optical path[228].

To address these challenges, we built upon our previous design[44] as well as those of others[157,158] and we developed the 2x2 microstretcher array which working principle is summarized in Fig. 4.1. This new design allowed the study of ~4x200 cells per array, leading to robust measurements enabling the detection of subtle changes which could have remained unexposed without such parallelization. Cyclic stretching is achieved by using vacuum chambers that repeatedly deform the walls surrounding a suspended membrane on which cells are adhered. The throughput and ease-of-use were considerably increased by scaling it into an array and most importantly by allowing the microdevice to be easily made open-top at any point over the course of an experiment, i.e. when the microfluidic properties are no more required or beneficial. In several instances, it will be desirable to preserve the microfluidic nature of the device over the course of the actual experiment but to convert it into an open-top device before staining and imaging.

Previous pneumatic-based microfluidic stretchers were generally permanently closed[11,44,157,158]. The general approach used here consists instead in extending the cell chamber height in such a way as to leave only a thin PDMS layer to act as the top sealant. When properly fabricated, this thin layer (on the order of 200 µm thick) can be easily peeled off under a microscope with tweezers. It is worth noting that the ability to switch from a closed-top to an

open-top microfluidic device is of general interest and has been addressed previously in other contexts by using a (non-PDMS) lid[229,230]. The all-PDMS strategy that we present here is an attractive alternative due to its fabrication and utilization simplicity, as well as its robustness with respect to eliminating leakage risks. Although disadvantageous for imaging, conserving the microfluidic properties can be highly beneficial in various studies investigating the combined effect of different stimuli, for instance shear flow stress or time-varying chemical concentrations, together with the underlying substrate strain[156,231,232]. The main fabrication steps are presented in section 4.5.

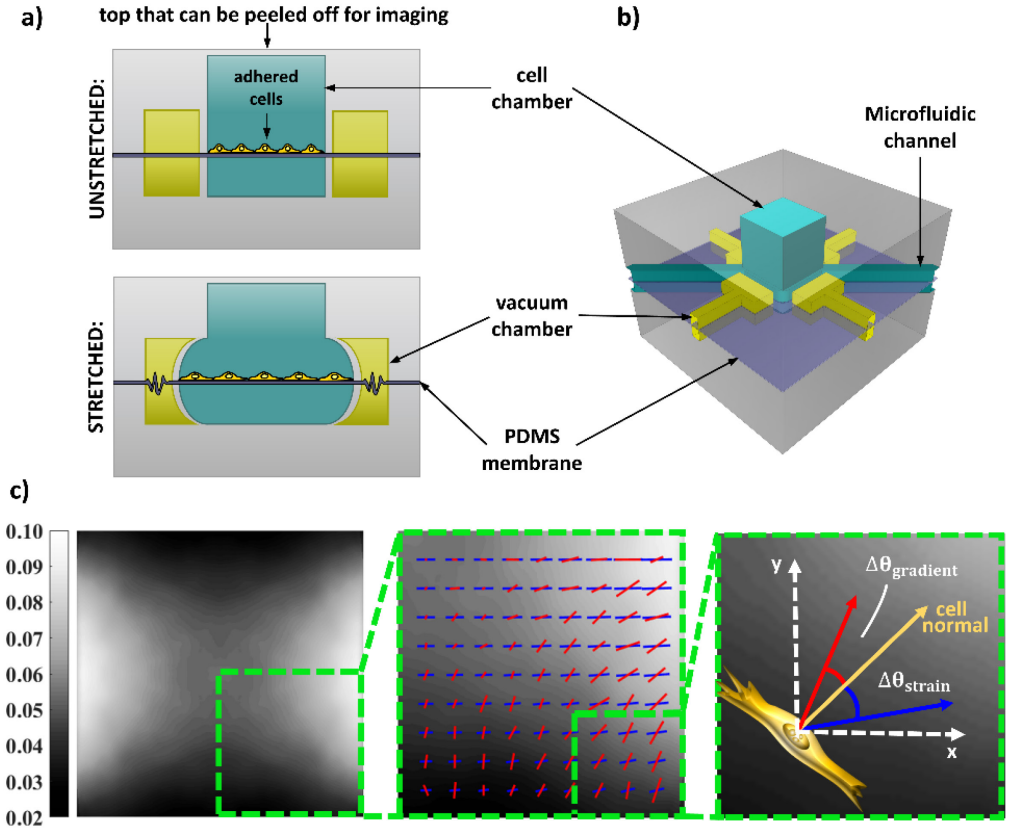

Figure 4.1 Microfluidics stretcher working principle, membrane strain field map and angle convention. a) Side view of the design presented to show the unstretched (top) and the stretched (bottom) states. The schematic is not to scale and has been adapted from previous work[224]. **b)** Three-dimensional view, partially transparent to show the design. **c)** Left: Colormap of the experimentally determined maximum principal strain amplitude $\varepsilon_1(x,y)$ for x-stretching. The full membrane is shown (1.6 mm x 1.6 mm). Middle: The bottom right corner of the membrane is zoomed such that 25% of the total area is displayed. A representation of the amplitude (line length) and direction (line orientation) of the maximum principal strain (blue lines) and its gradient (red lines) is also presented. Right: The bottom right corner is further zoomed in to depict a fictive cell (yellow) and the angle convention used throughout the article. The red arrow

represents the gradient direction and the blue is the strain direction. The angle difference between the cell normal and the gradient direction is identified as $\Delta\theta_{gradient}$ while the angle difference between the cell normal and the strain direction is given by $\Delta\theta_{strain}$.

4.3.2 STRAIN FIELD CHARACTERIZATION AND DEVICE IMAGINING PERFORMANCE

The membrane's strain field generated in the microdevice is presented in Fig. 4.1c (for X-stretching). It is based on the analysis of the fluorescent beads displacements as explained in section 4.5. Importantly, our device's geometry and scale have the advantage of naturally producing smoothly-varying strain gradients (from 0 to 14%mm^{-1}) of significant and biologically relevant magnitudes[139] while maintaining the strain amplitude relatively low (2 to 10%), i.e. also biologically relevant to optimally induce the cellular responses [35,36,142]. Moreover, our design produces a strain field for which the position dependent principal strain direction is largely decoupled from that of the gradient. This is an essential condition to properly study their respective effects.

Efforts have been put recently in developing microfabrication strategies to allow high resolution microscopy in microfluidic devices by minimizing the optical path through PDMS which is known to introduce aberrations preventing diffraction-limited imaging[228,233]. Our approach presents an effective solution for micro-stretchers. Standard all-PDMS devices usually comprise >1mm thick layers to ensure structural integrity and proper external tubing connections[44]. Fig. 4.2 demonstrates the imaging capabilities of our hybrid microdevice once it has been made open-top. The image profile of a fluorescent bead obtained within the open-top chamber is compared with that obtained when a similar bead is covered with a ~800 um thick PDMS layer inserted in the light path (Fig. 4.2a). In average, the lateral FWHM resolution degrades by (30 ± 3)% with the insertion of the PDMS layer (Fig. 4.2b). This loss of lateral resolution is in qualitative agreement with that measured by Tonin *et al.*, who used an oil-immersion objective with which they actually observed an even more detrimental effect despite testing thinner layers[228]. Importantly, the spread in the distribution of lateral FWHMs shown in Fig. 4.2b is also significantly larger in the closed-top case, rendering deconvolution-based image analysis strategies less reliable[234]. Axially, we measured an average four-fold increase of the bead's profile width (Fig. 4.2c), demonstrating a dramatic decrease in one's ability to resolve features depth-wise in closed-top PDMS devices. Finally, we note that open-top imaging is also beneficial with respect to photobleaching since lower laser excitation intensities are required (~five-fold in our case) to achieve similar peak signal

intensities. The overall deterioration in resolution (in particular axially) can be attributed primarily to the introduction of spherical aberrations which result from refractive index mismatch[235–237]. Additional explanation is provided in the Appendix B. Overall, our results show the advantage of using our design over a traditional closed-top microdevice. To illustrate the relevance of this high imaging capability in the context of cell biology, Fig. 4.2d shows the actin filaments and the FAs of an HFF cell imaged in our device via immunofluorescence staining.

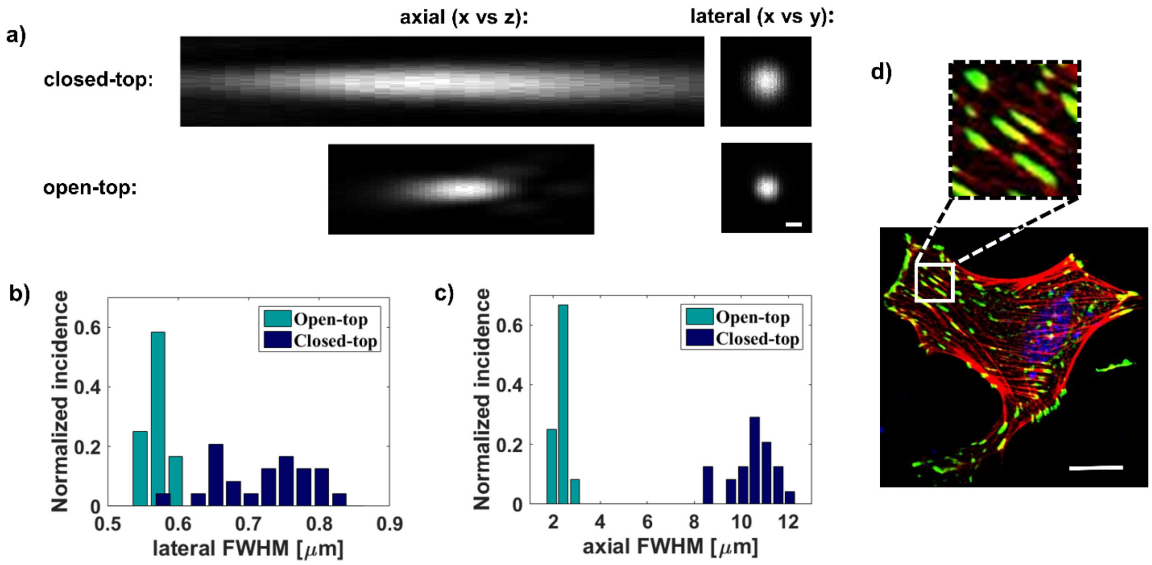

Figure 4.2 Imaging resolution improvement achieved by making the micro-stretcher open-top. a) Axial and lateral fluorescence profiles of a bead (diameter=200nm) imaged within the hybrid microstretcher made open-top and under a 800 µm thick PDMS layer. The scale bar is 500 nm. The distributions (n_{beads}=24 for each condition) of lateral **(b)** and axial **(c)** FWHMs show significant loss of resolution (and increased variations) upon the introduction of the PDMS layer in the light path. The average lateral FWHM of the bead profile is 0.57 (s.d. = 0.02 µm) in the open-top case while it is 0.72 (s.d. = 0.07 µm) in the closed-top case, translating into 0.53 (s.d. = 0.02 µm) and 0.69 (s.d. = 0.07 µm) FWHM resolutions upon deconvolution of the bead size. **d)** Immunofluorescence composite image of a HFF cell adhered on the fibronectin-coated PDMS membrane of a hybrid microstretcher made open-top. The actin filaments are shown in red, the DNA in blue, and the vinculin in green. The inset magnifies a few FAs and attached actin filaments. The scale bar is 25 µm. All the images were acquired with a laser scanning confocal microscope using a 25X objective.

4.3.3 CELL MECHANORESPONSES TO REPEATED CHANGES IN STRAIN DIRECTION

It was previously demonstrated that the reorientation response of cells subjected to two subsequent periods of cyclic stretching along perpendicular directions was qualitatively similar[44,191]. Prior to the present study, the question remained however whether the responses

are quantitatively different and whether cellular realignment can be induced a larger number of times. Moreover, in both of these previous studies, only regions of approximately uniform strain (no strain gradient) were analyzed. Fig. 4.3a-f display normalized incidence histograms of the angle difference between the experimental cell normal orientations and the X-axis following seeding, and then 5 subsequent stretching periods (11 hours each), alternating between X- and Y-stretching. It can be observed that the cells are randomly oriented following seeding, and then they successfully realign perpendicularly to the stretching directions five successive times. Since the strain direction varies across the membrane, and to ease comparison from one reorientation to the other, Fig. 4.3g-l presents the same data as Fig. 4.3a-f but the orientations are reported with respect to the local principal strain direction. Moreover, considering that lower strain amplitudes are inefficient at inducing reorientation[36,224], regions of sub-5% strain amplitude were excluded in Fig. 4.3g-l. As a result of these two considerations, a systematic narrowing is observed in the angle distributions from Fig. 4.3a-f to 4.3g-l. Interestingly, it can be seen from both sets of histograms that, although the cells do realign largely perpendicularly to the strain direction after each stretching periods, there is progressive broadening of the distributions (in Fig. 4.3, first from a to f, and then from g to l). This reveals a decrease in cell normal alignment with the principal strain direction as time progresses, and thus as the stretching direction alternates.

The evolution of the cellular orientations and morphologies was further analyzed and the results are reported in Fig. 4.4. The average angle difference between the X-axis and the experimental cell normals are displayed in Fig. 4.4a. The control is stable around 45° since the cells are randomly oriented and the data are reported between 0° and 90°. In contrast, the mean orientation of the cyclically-stretched cells with respect to the X-axis oscillates between low and high values. It is worth noting that the *means* are 20°-25° away from the *preferential* orientations (~0° for X-stretching and ~90° for Y-stretching, as seen in the histograms 4.3a-f) because of the statistical nature of the realignments[118] and the fact that the data are reported between 0° and 90° (as opposed to between 0° and 180°). Fig. 4.4b shows the average angle difference between the local principal strain directions and the experimental cell normals, in regions of high strain amplitude (> 5%). The qualitative assessment that we noted previously is confirmed in this plot: the cell normal alignment with the principal strain direction decreases progressively. The near-linear increase of mean $\Delta\theta_{strain}$ in Fig. 4.4b, corresponding to a "poorer" alignment of the cell

normals with the local strain directions, can be explained by the presence of another mechanical cue.

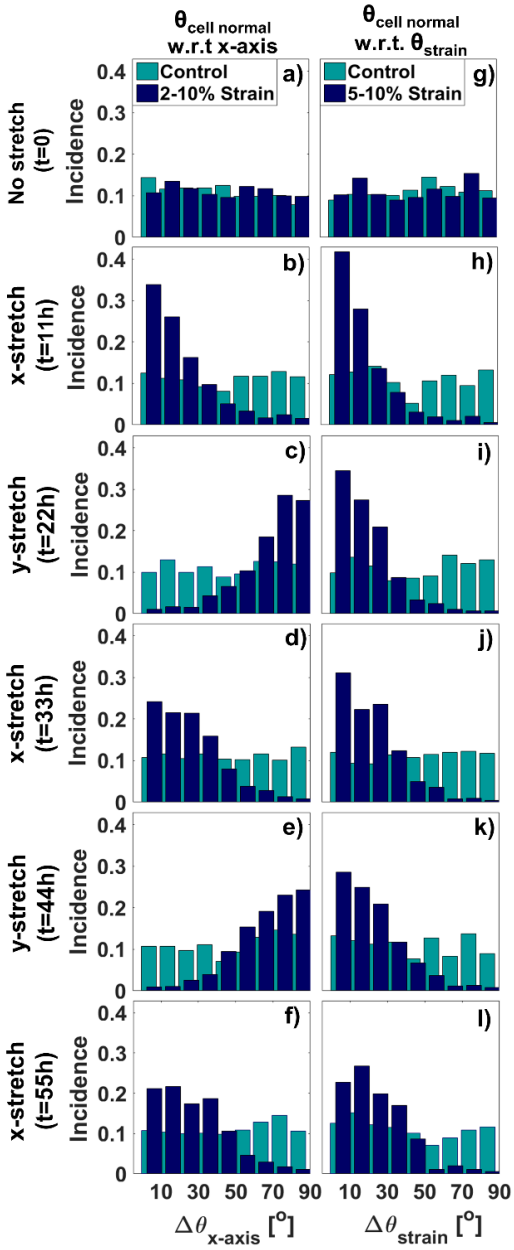

Figure 4.3 Reorientation analysis of HFF cells subjected to 5 changes in stretching direction over a period of 55 hours. a-f) Normalized incidence histograms of the angle difference between the experimental cell normals and the X-axis, considering the full membrane. **g-l)** Normalized incidence histograms of the angle difference between the experimental cell normals and the underlying maximum principal strain direction (considering the regions of high strain amplitude (> 5%)). The histograms **a)** and **g)** show the orientation distributions after 15 hours of seeding. The histograms **b-f)** and **h-g)** show the orientation distributions (of the same cells) after each of

the five-successive cyclic-stretching periods of alternating directions (each lasting 11 hours). All the histogram in comprise the combination of 6 unstretched control experiments as well as the combination of 6 cyclically stretched experiments. For **a-f)** $n_{control} \approx 1.4x10^3$ cells and $n_{strain} \approx 1.0x10^3$ cells while for **g-l)** $n_{control} \approx 8.5\ x10^2$ cells and $n_{strain} \approx 6.3x10^2$ cells.

The strain gradient has recently been identified as a genuine mechanical cue involved in the reorientation response of fibroblasts[224] and it can indeed explain the trend observed in Fig. 4.4b. The mean angle difference between the experimental cell normals and the principal strain gradient directions is displayed in Fig. 4.4c, considering the regions of larger strain gradient amplitude (> 7% mm^{-1}). Interestingly, conversely to the cell normal alignment with respect to the strain, there is a slight improvement of the cell normal alignment with respect to the local strain gradient direction, as the experiment progresses. Since the improvement of one is on the same order of magnitude as the deterioration of the other (and the two membrane regions considered overlap greatly), we speculate that these two trends result largely from an interplay between the cellular mechanoresponse to these two cues (strain and strain gradient fields).

To understand how a progressive improvement in cell normal alignment with the gradient is possible despite the drastic changes in the applied stretching direction (X or Y) imposed every 11 hours, the average local change in membrane's gradient direction is evaluated (Fig. 4.4d). In average, in the regions of large gradient amplitude considered in Fig. 4.4c, the direction of the strain gradient shifts by only ~20^o for every change in stretching direction (due to the specific geometry of the strain field). Since this angle is relatively low, the trend observed in Fig. 4.4c could be explained by the fact that cells take longer to align with the strain gradient that they do with the strain itself. Their alignment progression over each stretching period is not abolished because the gradient direction only changes by 20^o every 11 hours. In other words, they can slowly adapt even though the gradient response seems slower. In contrast, we determined from our extracted strain field that the direction of the strain shifts in average by ~ 80^o between every change in stretching direction (in the regions of large strain amplitude considered in Fig. 4.4b). This angle is relatively high and as we will explicitly demonstrate in Fig. 4.5, 11 hours is sufficient for the cells to complete the strain-induced reorientation response.

The effect of cyclic stretching on the cell morphology is examined in Fig. 4.4e where the distribution of aspect ratios is presented for non-stretched and stretched cells. It can be seen that cyclic stretching causes cell elongation, in agreement with previously reported studies[118,220]. Interestingly, we observe a narrowing of the distribution for the stretched cells. Fig. 4.4f displays

the evolution of the cell morphology over the course of the multiple reorientation experiment. Except for the first-time point (at t=0 hour), for which the control and strain data overlap, the stretched cells are systematically more elongated that the control ones. Moreover, the stretched cells' morphology appears to further evolve following the initial elongation. We observe a significant recovery of the aspect ratio from 11 to 55 hours (p = 0.016, see caption Fig. 4.4f), once again suggesting a rather complex mechanoresponse involving possibly more than one time-scale.

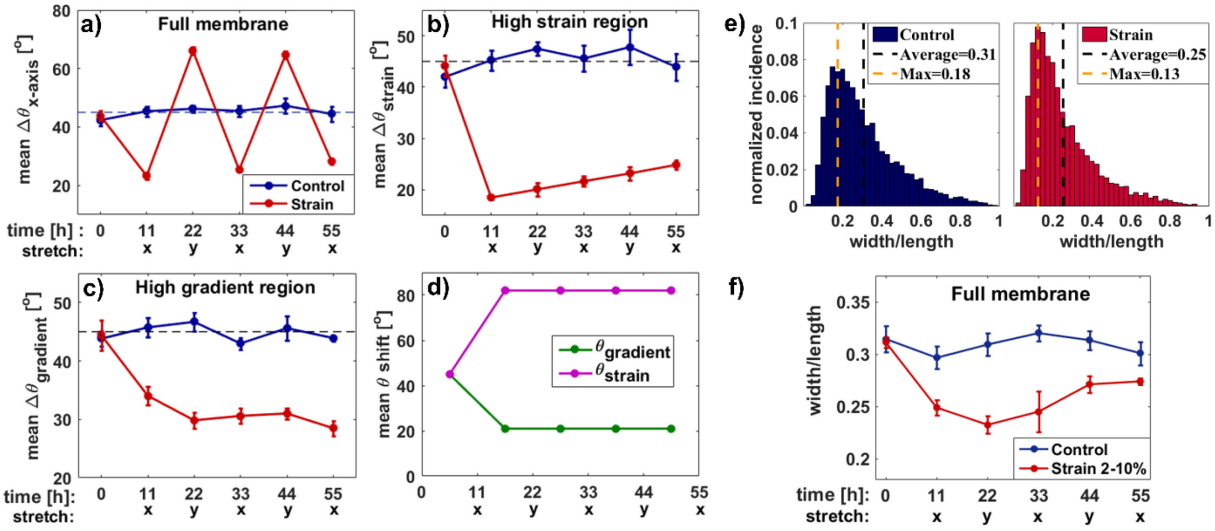

Figure 4.4 Evolution of cell orientation and elongation over the course of multiple reorientations. a) Mean angle differences between the experimental cell normals and the X-axis (mean $\Delta\theta_{x\text{-}axis}$) as a function of time (and stretching direction), considering the full membrane area. $n_{control} \approx 1.4x10^3$ cells and $n_{strain} \approx 1.0x10^3$ cells. **b)** Mean angle differences between the experimental cell normals and the principal strain directions (mean $\Delta\theta_{strain}$) as a function of time (and stretching direction), considering the regions of large strain amplitude (> 5%). $n_{control} \approx 8.5 x10^2$ cells and $n_{strain} \approx 6.3x10^2$ cells. **c)** Mean angle differences between the experimental cell normals and the principal strain gradient directions (mean $\Delta\theta_{gradient}$) as a function of time (and stretching direction), considering the regions of large strain gradient amplitude (> 7% mm^{-1}). $n_{control} \approx 6.2\ x10^2$ cells and $n_{strain} \approx 4.6x10^2$ cells. In the plots **a-c)**, the blue curves show the unstretched control experiments and the red curves show the cyclically-stretched experiments, while the doted lines show the expected mean angle for perfectly randomly oriented cells. The errors on the means in **a-c)** are systematically lower in average for the stretched cells since the alignment is consistently guided by the strain field. **d)** Mean rotation angle that the cells would need to cover (mean $\Delta\theta_{shift}$) - as a result from a change in stretching direction - if they were to perfectly align with the strain direction (green) or with the strain gradient direction (purple), in the regions of large strain amplitude and large strain gradient amplitude, respectively. Since the cells are randomly orientated before stretching, the first angle is 45°. **e)** Normalized incidence histograms of the width-over-length ratio for the unstretched control experiments (blue) and the cyclically-stretched experiments (red), with the data from the 5 successive reorientations combined together. $n_{control} \approx 6.8\ x10^3$ cells and $n_{strain} \approx 5.1x10^3$ cells. **f)** Mean width-over-length

ratio of the cells as a function of time (and stretching direction), considering the full membrane. The blue curve shows the unstretched control experiments and the red curve shows the cyclically-stretched experiments. $n_{control} \approx 1.4x10^3$ cells and $n_{strain} \approx 1.0x10^3$ cells. In plots **a-c)** and **f)**, the error bars represent the standard error of the mean within the 6 unstretched control experiments and the 6 cyclically-stretched experiments. The data points associated with 11 h and 55 h are statistically different in **a)**, **b)**, **c)**, and **f)**, with p-values of p=0.011, p=0.0004, p=0.016, and p=0.016, respectively.

4.3.4 TIME-DEPENDENT CELL RESPONSE TO MECHANICAL CUES

The characteristic cell behaviors observed in the multiple reorientation experiments (Fig. 4.3 and 4.4) suggest the presence of a dual time-scale mechanoresponse which we now seek to explicitly investigate. Fig. 4.5a presents the temporal evolution of the cell orientations over 36 hours of X-stretching (no change in stretching direction) in the region of high strain gradient amplitude (> 7% mm^{-1}). The cell alignment with the strain direction (red) and the strain gradient direction (green) are both presented by showing the mean angle difference (mean $\Delta\theta$) between the cell normal and the strain or the strain gradient directions, respectively. To quantitatively assess the temporal evolution of the cellular response to the strain field, exponential decay fits ($\Delta\theta = A[e^{-t/\tau} - 1]+45^o$) were performed resulting in time constant of τ_{strain} = [1.6 $^{\pm}$ 0.3] hours and $\tau_{gradient}$ = [5 $^{\pm}$ 1] hours. Note that the last two time points were excluded from the fits to ensure that the cell density was approximately constant (<20% change).

The mean $\Delta\theta_{strain}$ initially drops abruptly, indicating a rapid realignment response with the strain direction, which is in qualitative agreement with previous studies[34,174]. It then reaches a minimum between 10 and 20 hours, after which it undergoes a slight increase, indicating a reduced alignment (p = 0.046, see caption Fig. 4.5). As suggested above, this rise can be explained by the concurrent increase in cell alignment with the strain gradient direction (p = 0.011, see caption Fig. 4.5). Since the mean $\Delta\theta_{gradient}$ exhibits a much slower drop, the relative importance of the gradient cues with respect to that of the strain cues only becomes significant at later time points. Consequently, as the cell normal alignment with the gradient direction continues to improve after 20 hours, the alignment with the strain direction worsen.

Taken together, our results demonstrate a consistent cellular response to given mechanical cues (strain and strain gradient) despite drastic changes in strain direction, suggesting the absence of apparent major stretched-induced irreversible changes. They also reveal that the mechanoresponses associated with two different aspects of an applied strain field take place on

different time scales. This suggests that there might be subtle differences in mechanotransduction mechanisms involved in the cellular responses to strains and strain gradients. It has been suggested in a previous study that the strain gradient sensing mechanism possibly involves the creation of an intracellular biochemical gradient[224]. This could explain why the mechanoresponse of cells to the strain gradient takes place on a longer time scale. In this study, the cellular responses depend on the specific history of the mechanical cues: in the presence of non-uniform and time-varying strain fields, the interplay between cues can give rise to a complex cellular mechanoresponse with a temporal evolution that depends on previous events.

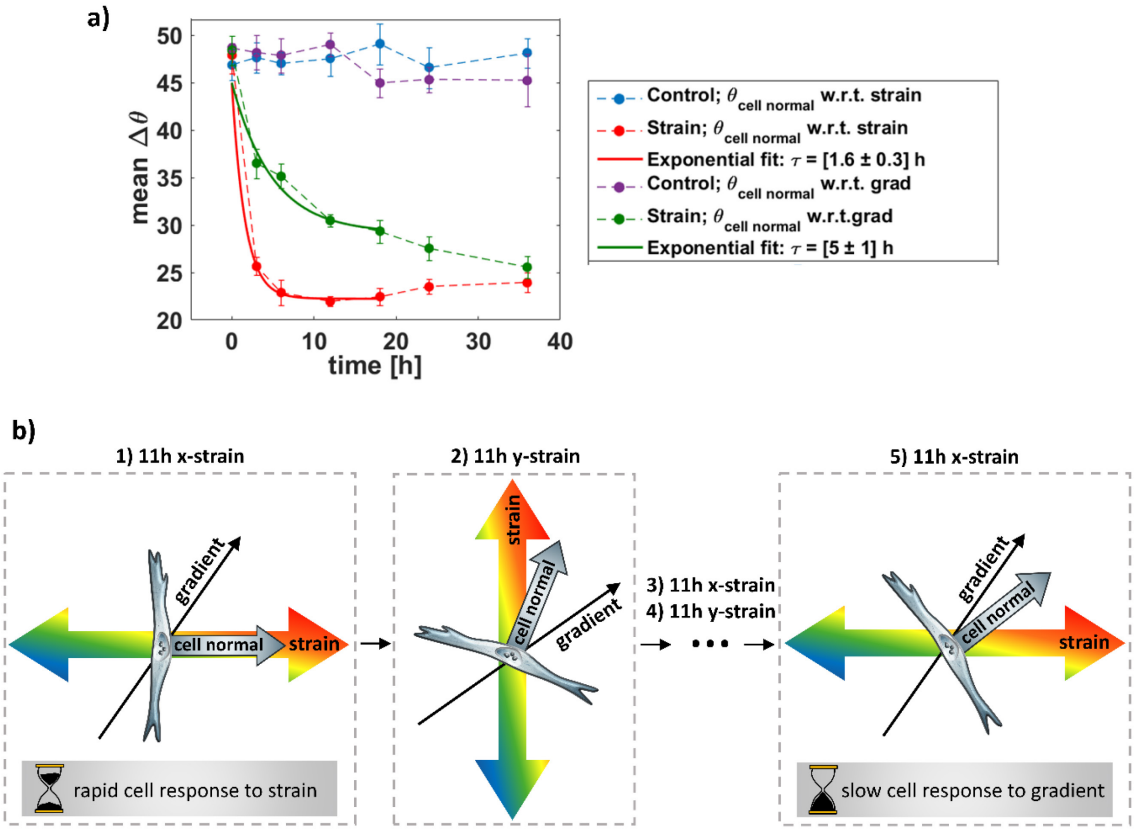

Figure 4.5 Time-scale mismatch between the strain and strain gradient responses. a) Time-dependence of the cellular response over 36 h of X-stretching. Temporal evolution of the mean angle differences between the experimental cell normals and either the strain directions (red curve) or the strain gradient directions (green curve) in the regions of large strain gradient amplitude (> 7% mm^{-1}). Exponential fits are also displayed, considering only the first 18 hours to ensure near-constant cell density (<20% change). The error bars on the experimental points represent the standard error of the mean within the 5 unstretched control experiments and the 8 cyclically-stretched experiments. The uncertainty on the exponential fits represent the standard error of the mean of the time constants extracted for the individual experiments. $n_{control} \approx 6.5 \times 10^3$ cells and $n_{strain} \approx 8.4 \times 10^3$ cells. The rise of the red curve beyond 12 h is statistically significant (p =

0.046, data of the last two time points compared to the data of the two previous points). The drop of the green curve beyond 12 h is statistically significant (p = 0.011, data of the last two time points compared to the data of the two previous points). **b)** Evolution of the cellular orientation in response to complex and varying strain field over 55 hours. 1) After 11 hours of cyclic X-stretching, the cell normal is well aligned with the principal strain direction (not with the gradient direction). 2) 11 hours after changing the stretching direction, the cell normal is mostly aligned with the strain direction, but the effect of the gradient is starting to influence the cell direction. 3-4) Over the subsequent changes of stretching direction, the cell normal continues to further align with the gradient direction and less with the strain direction. 5) 11 hours after the fifth change in stretching direction, the cell normal is approximately halfway between the gradient and the strain directions. This pattern of cellular reorientation can be explained by two elements. First, the geometry of the complex strain field is such that in average, each shift of stretching direction consist in a ~80^{o} change of principal strain and a ~20^{o} change of gradient direction. Second, the cell reorients more rapidly in response to strain than to the strain gradient.

4.4 CONCLUSION

We presented a microfluidic stretcher array developed to study the reorientation response of human fibroblasts in a non-uniform strain field subjected to repeated changes in stretching directions. Its improved capabilities and usability with respect to previous micro-stretcher designs make it a device of choice for future cyclic- or static-stretching studies aiming to investigate the effect of non-uniform strain fields. Using this device, we exposed the adaptability of cells to discontinuous mechanical cues by achieving multiple successive cellular reorientations. By demonstrating that two aspects of the strain field drive cellular responses on different time-scales, we gained further insight on the physical interaction between a cell and its microenvironment. Such strategy of exposing cells to increasingly complex in vitro environment is key to understanding the interplay of different cues and how it affects the cells' fate.

4.5 MATERIALS AND METHODS

4.5.1 MICROFLUIDIC STRETCHER DESIGN AND FABRICATION

SU-8 master fabrication. Fig. 4.6 describes the device and its general fabrication strategy. PDMS microdevices were manufactured using a replica molding approach. To fabricate the master mold, a photomask pattern (Fig. 4.6a) was transferred to negative SU-8 photoresist (Microchem, MA, USA) using standard soft lithography procedures on a silicon wafer. The thickness of the pattern (340 µm) involved the deposition of two separate layers of 2050 SU-8 (2x170 µm). Standard cleaning, pre-baking, spin coating, soft baking, UV-exposure through the photomask, post-baking, developing, and hard baking procedures were employed (consistent with manufacturer's

recommendations). Note that the design includes deep (340 µm) and narrow (120 µm) trenches between the cell chambers and the vacuum chambers (Fig. B.1, Appendix B), making conventional SU-8 development procedures insufficient. Instead, we used a more efficient strategy which is presented in the Appendix B.

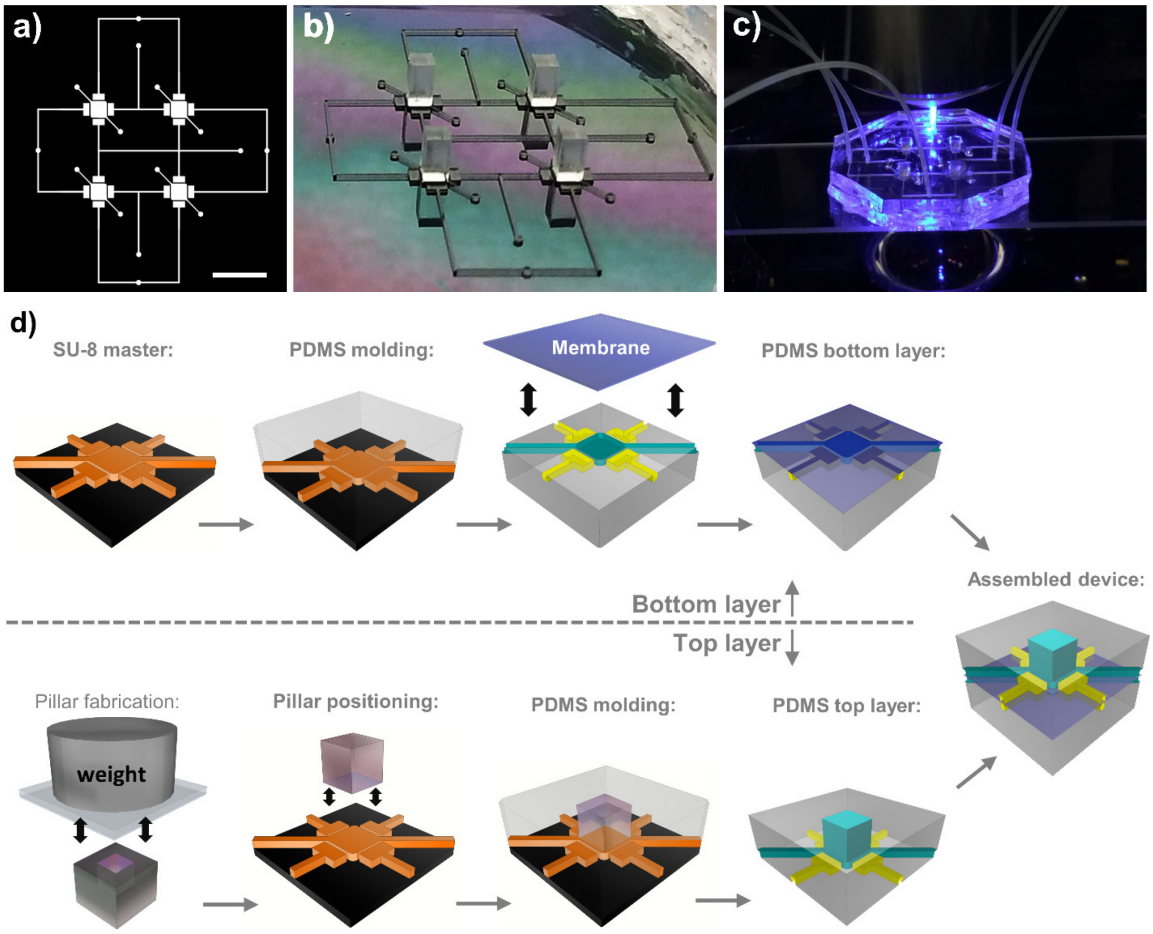

Figure 4.6 Microfluidic device and general fabrication strategy. a) Photomask of the top PDMS layer, showing the microdevice's pattern which includes the microfluidic loading channels, the vacuum pumps, and the cell chambers. The scale bar is 5 mm. **b)** Picture of the photoresist master used to mold the top layer of the device, after positioning of the PDMS pillars. **c)** Picture of the hybrid microfluidic stretcher during high resolution fluorescence imaging. **d)** Schematics of the main fabrication steps (showing one of the four cell chambers), which involve in particular the fabrication of chemically treated PDMS pillars (see Appendix B). The microfluidic device comprises three PDMS layers: two micropatterned layers and one thin (10 m) membrane, which is assembled on the PDMS bottom layer.

Augmented master combining SU-8 and PDMS for molding the top layer. To expand the design possibilities, we combine this master with movable chemically-treated PDMS sub-molds

(pillars in our case, see Appendix B for fabrication method). Specifically, the movable PDMS sub-molds are straightforwardly positioned onto the desired master features (on the cell chamber in our case), under a microscope (see Fig. 4.6b). The chemical treatment of the PDMS sub-molds prevents their polymerization with the uncured PDMS to be molded. Interestingly, it also facilitates the precise positioning of the sub-mold onto the SU-8 feature by providing an excellent balance between adhesion (to ensure that it stays in place when pouring uncured PDMS) and slipperiness (to ease fine repositioning). In practice, it is easy to achieve sub-100 µm positioning resolution with tweezers only, but higher precision tools (mask aligner or micro-positioners) can be used if greater resolution is needed. The details of the PDMS pillars fabrication method and chemical treatments are provided in the Appendix B. We note that an alternative method to achieve PDMS features of different heights would be to fabricate a multi-layers master via strategic photoresist layering and UV exposition patterning steps[238,239]. However, the SU-8 feature heights achievable (and thus PDMS open-top features) are typically limited to a few hundred microns and it becomes increasingly challenging with the number of different heights. Producing mm-thick PDMS layers is often desirable in order to ensure structural integrity upon manipulations and connection to external tubes. In contrast, the PDMS sub-mold strategy we used and outlined above has no such limitations (maximum height and number of different heights) in addition to be fast and simple, making it a method of choice for complex cell-scale device features. A summary of the other methods that we considered for the PDMS top layer fabrication is presented in Table B.1 of the Appendix B.

Device molding and assembly. The PDMS (Sylgard 184 silicone elastomer) top and bottom layers were molded using the microfabricated master described above. They were aligned and bounded using an air-plasma system (Glow Research, Tempe, AZ, USA) and a mask aligner (OAI, CA, USA). Prior to assembly, the bottom layer was bonded to a 10 µm thick PDMS membrane, which was spin coated onto a clean silicon wafer. The top layer is composed of features having two significantly different heights (~2 mm for the cell chambers, and 340 µm for other features). Uncured PDMS was then poured onto the augmented master mold described above (SU-8 features and positioned pillars) until PDMS barely covered the pillars.

4.5.2 CELL CULTURE, STRETCHING EXPERIMENTAL PROCEDURES, AND IMAGING

The cells were cultured in a standard incubator (37°C, 5% CO_2) and kept in DMEM with 10% FBS and 1% streptomycin/penicillin added (Hyclone Laboratories, Logan, UT, USA). Each microdevice was air-plasma treated (Glow Research, Tempe, AZ, USA) for 5 minutes at 70 W for hydrophilicity and to reduce the risk of trapping air bubbles. Flushing the microchannels with 70% ethanol for 5 minutes and then with autoclaved PBS solution ensured sterilization and removal of ethanol from the microdevice, respectively. Prior to cell seeding, in order to promote the cell adherence to PDMS, each membrane was functionalized via incubation for 4 hours in a solution of fibronectin 10 µg/ml of HEPES-buffered salt solution (HBSS; 20 mM HEPES at pH 7.4, 120 mM NaCl, 5.3 mM KCl, 0.8 mM $MgSO_4$, 1.8 mM $CaCl_2$ and 11.1 mM glucose). A density of adhered cells of ~300 cells/membrane was achieved by injecting a solution of culture medium with $5x10^4$ cells/ml, and using an incubation time of 15 hours. Note that two different seeding methods can be employed with our device. First, the cells can be loaded into the device's stretching chamber via the microfluidic channels using pressurized vials. Second, a micropipette can be used to directly deliver the cell solution if the PDMS layer acting like a top sealant has been peeled off beforehand (which is the case when the microfluidic properties are not required during the experiment, see section 4.4).

All the stretching experiments were carried out within the incubator to ensure optimal environmental conditions. The vacuum pumps were controlled via a Labview program creating sinusoidal stretching waveforms (2 to 10% strain amplitude across the membrane, 0.5 Hz). To acquire the cell orientation data over the course of the experiments, the cells were imaged before and between stretching periods by interrupting the cyclic stretching momentary (~10 minutes). A Nikon TiE inverted phase contrast EPI microscope (long working distance 10X objective) was employed to image the living cells within the devices. Immediately after imaging, cyclic stretching was reinitiated to continue the experiments. Fig. 4.2d was obtained in separate experiments by immunofluorescence staining and imaging the cells directly within the microfluidic device, 15 hours after seeding. Details of the staining protocols are given in the Appendix B.

4.5.3 MEMBRANE STRAIN FIELD CALCULATION

The detailed method to extract the strain field was published previously[224]. First, fluorescent beads (FluoSpheres, 200 nm, Invitrogen, CA, USA) embedded in the elastic membrane were

repeatedly imaged with an EPI fluorescence microscope as the membrane was stretched. Their displacements were then extracted with a custom Matlab script in order to calculate the maps of the Green strain matrix elements, and subsequently the maps of the maximum ($\boldsymbol{\varepsilon_1}(x,y)$) and minimum ($\boldsymbol{\varepsilon_2}(x,y)$) principal strain fields[138]. The interpolated and boxcar smoothed strain fields of 5 devices (and their mirror images, since the device is symmetrical) were averaged together to provide an accurate representation of the device population. For every position across the membrane, the maximum principal strain field is associated with the direction of maximum stretch while the minimum principal strain field is associated with the direction of minimum stretch or maximal compression. In our device, the amplitude of the former largely dominates that of the latter across the full membrane. Therefore, in the orientation analysis, the cell normals were reported with respect to the maximum principal strain direction when specified as $\Delta\theta_{strain.}$ Finally, the gradient field (of the maximum principal strain) was calculated everywhere across the membrane.

4.5.4 CELL ORIENTATION AND ELONGATION ANALYSIS

The background noise was reduced from the phase contrast images with a Fast Fourier Transform bandpass filter using ImageJ. To capture the cell morphologies, binary images were generated with the adaptive threshold plugin. The cell orientations, positions and elongations were obtained via the Analyze Particles tools of ImageJ. The analysis of the extracted cell data was achieved with a custom Matlab script. In particular, the orientation of each cell normal was reported with respect to either the X-axis ($\Delta\theta_{x\text{-}axis}$), the local strain direction ($\Delta\theta_{strain}$), or the local strain gradient direction ($\Delta\theta_{gradient}$). The cells located within 150 μm of the chamber's walls were not considered to eliminate possible edge effects. At the end of the analysis, all angles were reported between 0 and 90^o in order to produce Fig. 4.3 to 4.5.

4.5.5 STATISTICAL ANALYSIS

Statistical significances were determined using unpaired two-tailed t-test, assuming unequal variances. The number of samples and the number of independent experiments are specified in each figure. The t-test were performed by considering the averages extracted from the independent experiments (as opposed to considering every single cell orientation from all experiments). The error on the degradation of the average lateral FWHM represents the standard error on the mean.

4.6 ACKNOWLEDGEMENTS

This work was supported by individual Natural Sciences and Engineering Research Council (NSERC) Discovery Grants to M.G. and A.E.P. S.C-L. was supported by NSERC Postgraduate Scholarships-Doctoral (PGS D). M.G. acknowledges support from the Ontario Ministry of Research and Innovation, and the Canada Foundation for Innovation (CFI). A.E.P. gratefully acknowledges generous support from the Canada Research Chairs (CRC) program.

CHAPTER 5 | MECHANICAL STRAINS DRIVE NEWLY TRANSFORMED EPITHELIAL CELLS TOWARD INVASIVENESS

Manuscript in preparation. The supplementary information is presented in Appendix C.

Authors: **Chagnon-Lessard, S**., Jean-Ruel, H., Godin, M., Pelling, A.E.

Motivation/objective: Previous studies indicate that Ras^{V12}-transformed cells leave epithelial sheets in a non-cell-autonomous manner and that cytoskeletal forces play a key role in this dynamic. Having demonstrated in Chapters 3 and 4 the impact that mechanical deformations can have on the overall cell behavior and cytoskeleton, we utilize our microstretcher to assess the effect of a biologically relevant strain field on Ras^{V12}-tranformed cells co-cultured with normal epithelial cells.

5.1 ABSTRACT

Apical extrusion is an epithelial defense mechanism against transformed cells, the efficiency of which depends on the ability of the surrounding normal cells to sense and eliminate them. This cellular competition process relies on forces generated by the cells' cytoskeleton, which is known to be remodeled by external mechanical forces. How external forces affect epithelial defense and transformed cell invasion is thus of primary interest, but little is known currently. Using microfluidic stretchers, we show that biologically-relevant strains jeopardize the epithelial defense mechanisms against Ras^{V12} transformed MDCK cells. Cyclic stretching favors Ras^{V12} protrusion formation and impedes Ras^{V12} cell apical extrusion. Concurrently, it prevents the formation of strong circumferential belts of actin in Ras^{V12} cells, previously established as a primary step of apical extrusion under static conditions. Taken together, our results indicate that external forces remodel key mechanical structures differently in Ras^{V12} than in normal cells, demonstrating that Ras^{V12} cells have different sensitivity to strain. We propose that these remodeling mismatches in actin cytoskeleton and adhesion complexes change the interaction between Ras^{V12} and normal cells, steering the system toward invasiveness. Inhibition of ROCK

partially restores Ras^{V12} apical extrusion under strain, suggesting together with other evidences the implication of the Rho-ROCK pathway in the strain-induced invasive phenotype of Ras^{V12} cells.

5.2 INTRODUCTION

Although they are one of the simplest tissues present in complex multicellular organisms, epithelial mono- and bi-layers play a crucial role as first-line protection of organs and the cavities they envelop[46,240]. Epithelial cells form tight physical barriers constituting an efficient defense against pathogens and preventing the passage of other cells and macromolecules[93]. The monolayers maintain their integrity and barrier function despite continuous cell division and death (normal epithelial cell turnover). Apical extrusion is the mechanism by which a dying cell is eliminated, but this cellular process is also a part of normal cell competition [94,97,241]. Certain cells exhibiting abnormal activities, such as some oncogenic expressions, are also apically extruded, although in a death-independent manner[115,242]. The majority of human cancers result from the transformation of a single cell following alteration in its genome[111]. Mutations converting a gene belonging to the Ras family into an active oncogene is found in 20% of human tumors[243]. Ras proteins influence numerous signalling pathways, such as Rho[113,114], leading to changes in actin cytoskeleton configuration as well as, among others, cell shape, contractility, adhesion, motility, and division. Previous studies showed that H-Ras^{V12}-transformed cells can be recognised and eliminated via apical extrusion by the concerted action of the surrounding wild type (WT) cells[47,112,242]. This has been referred to as epithelial defense against cancer or transformed cells. Diversion of the extrusion direction from apical to basal extrusion is observed in certain oncogenic cells, and is a potential mechanism to initiate metastasis[115,244–246]. Although the majority of Ras^{V12} cells are apically eliminated, some rather initiate basal invasions by remaining in the monolayer and growing protrusions. In certain cancers, their prominence has been linked to invasiveness[247]. Importantly, these Ras^{V12}-transformed cellular extrusion and protrusion behaviors are only observed when surrounded by WT cells.

Mechanical forces are intrinsic to the microenvironments in which biological systems evolve[‡], and physical cues are known to regulate a variety of cellular functions [248]. In this context, understanding of the mechanical contribution to tumor initiation and development is required for a holistic comprehension of cancer biology[104,249]. Cells are constantly sensing and responding to mechanical forces and properties of the surrounding extracellular matrix (ECM)[2]. Not only do cells actively adapt their biophysical properties, but they also remodel their microenvironment. This mechanical equilibrium regulates critical cell functions involved in cancer progression such as motility, differentiation, and proliferation[109,250]. For the recognition and elimination of transformed cells, epithelial defense against transformed cells relies on many cytoskeletal proteins and cell-generated contractile forces in both normal[112] and transformed cells[100,101]. Given that external forces can remodel the cytoskeleton architecture, it raises the question whether or not external forces also regulate the Ras^{V12} cells' fate within the epithelial monolayer.

Here we used polydimethylsiloxane (PDMS) microfluidic stretchers which mimic the complexity of the strain field present in vivo to study the early stage of epithelial cancer development in a model system. We examined the extrusion process and protrusion formation in cyclically stretched Madin-Darby Canine Kidney (MDCK) H-Ras^{V12}-WT co-cultures. Considering that contractile forces generated by cells are extensively involved in Ras^{V12} apical extrusion, it is of primary interest to investigate the interplay of external mechanical forces with this process. We demonstrated that the application of external strains triggers Ras^{V12} cell basal invasion by i) significantly reducing their apical extrusion and ii) promoting protrusion formation. We explored how the Ras^{V12} and WT cellular mechanoresponses differ and found that the strain-induced perturbations to their relative cytoskeletal organization drive the Ras^{V12} cells toward an invasive phenotype.

[‡] Epithelial cell sheets throughout the body are subjected to repeated forces either via direct deformation of the organ they envelop or indirectly via tissue matrix deformation.

5.3 RESULTS

5.3.1 EXTERNAL MECHANICAL FORCES PROMOTE RAS^{V12} INVASIVENESS

To generate a biologically relevant strain field, we employed an all-PDMS pneumatic-based microfluidic stretcher which we reported previously[45]. Cells were cultured on a thin suspended membrane encased in a cell chamber. This membrane was cyclically stretched via the deformation of the cell chamber walls, upon the activation of vacuum chambers. The co-culture of MDCK H-Ras^{V12}-WT (1:75) cells was seeded on the type-I collagen-treated membrane (relaxed state), and incubated in a tetracycline-free environment until a monolayer was fully formed (10 h). Cyclic stretching (1 Hz) and Ras^{V12} expression (induced with tetracycline) were then simultaneously initiated. The systems were imaged after 24 hours of stretching. A set of automated image analysis programs was developed to precisely characterize the strain-induced changes of key cellular components throughout the co-culture. Fig. 5.1a-c present the working principle of the device and a portion of the image analysis.

We first examined the Ras^{V12} cell behavior within the WT monolayer when no strain was applied within the microfluidic device. We observed the formation of small basal protrusions and found that a significant fraction of the Ras^{V12} cells were extruding as expected[47]. Fig. 5.1e shows that their average height was above that of the surrounding WT cells (see also Appendix C, Fig. C.1). An example of an extruding cell is shown in Fig. 5.1d. To study the impact of external mechanical forces on the system, we then examined the Ras^{V12} cell behavior under cyclic stretching and we observed a dramatic effect. Firstly, the average height of the Ras^{V12} cells dropped below that of the WT cells (Fig. 5.1e), suggesting a preponderance of basal – rather than apical – extrusion. Secondly, the average size of basal protrusions increased significantly (Fig. 5.1f), indicating increased aggressiveness in our model system. A representative example of a Ras^{V12} cell growing long protrusions under cyclic stretching is shown in Fig. 5.1d. The dependence on strain amplitude of the average protrusion size and Ras^{V12} cell height indicates that the degree of invasiveness is modulated by the force amplitude (Fig. 5.1h). As the resulting variation is small in our system, data were simply grouped as either strain or static elsewhere. Overall, our results demonstrate that biologically relevant forces trigger an invasive Ras^{V12} cell phenotype and impede the monolayer's ability to eliminate transformed cells.

Pharmacological treatments were used to interfere with the mechanical stability of cells. Blebbistatin and ROCK inhibitor Y-27632, which respectively inhibit myosin II activity and actomyosin contractility, both decreased Ras^{V12} extrusion under static conditions (Fig. 5.1e). This agrees with previous observations which demonstrated the importance of ROCK in the apical extrusion process[47]. Under cyclic stretching, both blebbistatin and ROCK inhibitor significantly reduced the effects of strain on Ras^{V12} cell behavior (Fig. 5.1e,f). This indicates that myosin II activity and actomyosin contractility are involved in the increased invasiveness induced by strain. We found that inhibiting FAK with PF-573228 also decreased the effect of strain, albeit more moderately (despite having the strongest impact on cell shape (see Appendix C, Fig. C.2). FAK stabilizes the actin cytoskeleton via the ROCK pathway and regulates the central proteins of focal adhesions[251], thus playing a key role in mechanosensing and transduction[252–254]. FAK inhibition is being investigated as a new therapeutic cancer target[104,255] and has been shown to bypass some extrusion defects[245]. Interestingly, it is only when stretching is applied that we observe a reduction of Ras^{V12} invasiveness upon FAK inhibitor addition. These results show that the structural integrity of the cytoskeleton strongly affects the process by which substrate strains change the system dynamics and trigger Ras^{V12} invasive behavior.

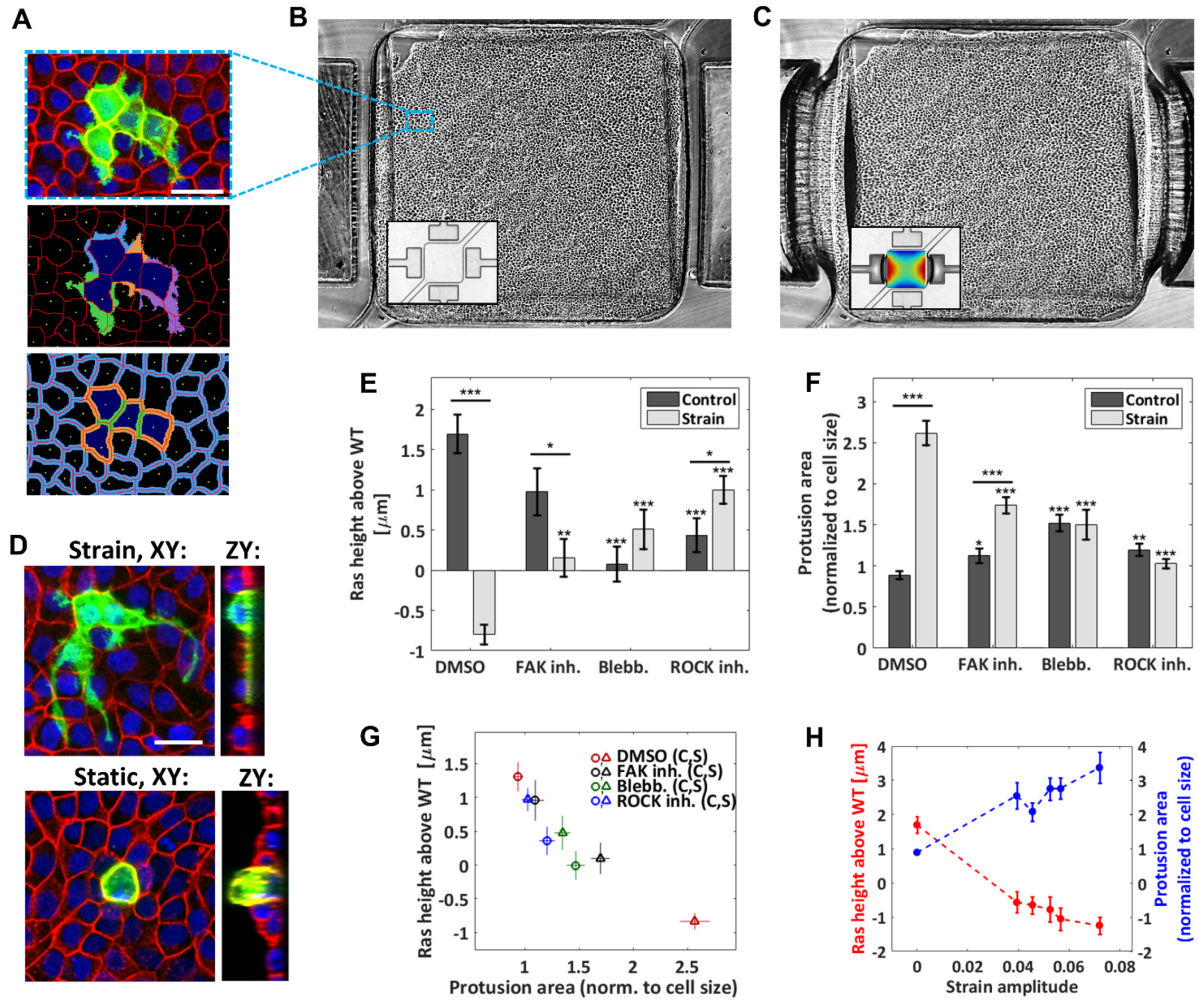

Figure 5.1 Cyclic stretching increases protrusion formation and hinders apical extrusion. a) Top: confocal image of the MDCK co-culture (Ras^{V12} and WT cells, static condition) with GFP-Ras^{V12} cells in green, actin in red, and nuclei in blue. Scale bar is 35 µm. Middle and bottom: image analysis output showing the nucleus centres (yellow), the cellular contours (red), the Ras^{V12} cell bodies (dark blue), associated protrusions (middle) and the junctional regions (bottom: Ras^{V12}-Ras^{V12} in green, Ras^{V12}-WT in orange, and WT-WT in blue). **b,c)** Monolayer grown in a PDMS pneumatic-based microfluidic stretcher in its relaxed **(b)** and stretched **(c)** states (phase contrast mode). The insets (bright field mode) show the empty device with the strain map superimposed in the stretched case (dark blue: 3%, dark red: 9%). The cell chamber width is 1.6 mm. **d)** Confocal images of GFP-Ras^{V12} transformed cells in WT monolayers 24 h after tetracycline addition followed by F-actin (red) and nuclei (blue) staining. Scale bar is 25 µm. Top: representative example of Ras^{V12} cell forming large protrusions obtained in a stretched experiment. Bottom: representative example of extruding Ras^{V12} cell obtained in a static control. **e)** Average height difference between the Ras^{V12} and WT cells for the static controls and stretched experiments. **f)** Average protrusion area relative to the cell body (i.e. excluding the protrusions) for the static controls and the stretched experiments. The drug-free case (DMSO) and three drugs were tested: FAK inhibitor, blebbistatin, and ROCK inhibitor. Data are mean ± s.e.m. *** P<0.0001, **P<0.005, *P<0.05. Stars above the individual bars relate to the corresponding DMSO condition. Stars above the horizontal

lines refer to the significance between the control and strain data. From left to right in **e,f)**, n = 234, 188, 78, 139, 268, 233, 237 and 334 cells each from 3 or 4 independent experiments. **g)** Correlation between the average Ras^{V12} cell height and the average protrusion area for the 8 conditions presented in **e,f)**. **h)** Average Ras^{V12} cell height (red) and average protrusion area (blue) as a function of the strain amplitude, for the DMSO condition. The zero-strain points correspond to the average of the control data, and the non-zero strain points were obtained by binning the data of the stretched experiments into five bins each containing an equal (37-38) number of cells.

In consideration of all conditions tested (DMSO, blebbistatin, ROCK and FAK inhibitions, each combined to both static and cyclically stretched substrates), we found a strong correlation between the average protrusion size of the Ras^{V12} cells and their average height relative to the surrounding WT cells (Fig. 5.1g). The decrease in apical extrusion is consistent with the facilitated protrusion growth of Ras^{V12} cells under strain. From a mechanistic point of view, it is more difficult for the WT cells to "squeeze out" a transformed cell which has increased adhesive contact area with the substrate, as hinted by Gudipaty *et al.*[46].

5.3.2 THE STRONG CORTICAL ACTIN BELTS AROUND RAS^{V12} CELLS VANISH UNDER STRAIN

The process by which epithelial monolayers expel dying cells to maintain their integrity is now believed to begin with the formation of a cortical contractile F-actin belt in the dying cell itself[97]. The cortical actomyosin cytoskeleton of a cell produces contractile forces that are coupled to neighboring cells via E-cadherin adhesions[101,240,256]. Specific patterns of intercellular tension are controlled in part by the cortical F-actin network. Dysregulation of this pattern of contractility at the cell-cell junctions has been shown to drive oncogenic extrusion[100,101]. An increase in cortical contractile F-actin within the Ras^{V12} cells was also found to be actively implicated in their extrusion by the surrounding WT cells[100,101]. Since these previous results indicate that cortical actin is critical in determining the fate of Ras^{V12} cells, we investigated the effects of strain on the remodeling of cortical actin throughout the co-culture. We observed, in agreement with previous studies[47,100], the presence of a strong cortical actin belt in Ras^{V12} cells under static conditions (Fig. 5.2a,b). In contrast, upon cyclic stretching (in the drug-free case), the difference in cortical actin intensities between Ras^{V12} and WT cells vanishes. Hence, when physiological mechanical forces are applied, the Ras^{V12} mutation in MDCK cells is generally not sufficient to trigger the formation of the strong cortical actin belt associated with apical extrusion. This suggests that external strains at least partially alter the extrusion mechanism by preserving uniformity among the actomyosin contractile patterns in Ras^{V12} and WT cells. Upon the addition of FAK inhibitor, blebbistatin, and ROCK inhibitor, the strain-induced alteration of the actin ratio is largely suppressed. That is, the

formation of a strong actin belt is not eliminated (Fig. 5.2b and Appendix C, Fig. C.3b). This shows that the abolition of the strong actin belt via external strains is at least partially regulated by the Rho-ROCK pathway. It also further supports the importance of the actin belt in the extrusion process, as highlighted by the strong correlation between the junctional actin intensity ratio Ras^{V12}-Ras^{V12}/WT-WT and the extruding Ras^{V12} height (Fig. 5.2c). Importantly, these results show that strain remodels the cytoskeleton differently in Ras^{V12} and WT cells, specifically at their junction, thus affecting their interaction.

5.3.3 THERE IS A RELATIVE DEPLETION OF THE E-CADHERIN ADHESIVE BELT IN RAS^{V12} CELLS UNDER STRAIN

Previous studies have shown that the loss of e-cadherin is an important step in the development of cancer[257] and that the loss of cell-cell adhesions is related to more invasive phenotypes[258,259]. For instance, activating RhoA and ROCK was found to promote cancer cell invasion via the disruption of e-cadherin adherent junctions[260]. We investigated the effects of strain on junctional e-cadherin signal intensity (Fig. 5.2f,g, C.4c and C.6 from Appendix C). We observed that strains induce changes in e-cadherin differently in WT than in Ras^{V12} cells. In the static control, the accumulation of e-cadherin at Ras^{V12}-WT (or Ras^{V12}- Ras^{V12}, see Appendix C , Fig. C.3c) interfaces is greater than that at the WT-WT interfaces. This e-cadherin intensity mismatch diminishes upon cyclic stretching. This relative depletion of the e-cadherin adhesive belt in Ras^{V12} cells is coherent with a model in which increased RhoA-ROCK activity, in our case via mechanical strains, promotes a more invasive phenotype.

5.3.4 STRAINS PROMOTE BASAL SF FORMATION IN WT CELLS BUT NOT IN RAS^{V12} CELLS

To further investigate the mechanical landscape in which Ras^{V12} cells evolve, we analyzed the basal actin network of the monolayer. Almost no basal actin stress fibers (SFs) were visible in the static DMSO control (Fig. 5.2a). In contrast, upon stretching, they were largely promoted in the WT cells as shown in Fig. 5.2a,d. Indeed, the activation of the RhoA-ROCK pathway (and the subsequent increase in myosin phosphorylation) following the application of substrate strain on cells promotes the formation of the actomyosin cytoskeleton[261]. Sahai *et al.*[90] showed that the generation of contractile forces via the Rho-ROCK pathway disrupts cell-cell junctions. From mechanical considerations, a well-developed actomyosin network exerting high tension tends to reduce cell-cell contact and adhesion strength[256,262]. This suggests that the WT-WT cell adhesion

integrity is altered by the increased actomyosin network following cyclic stretching. Since the fate of Ras^{V12} cells depends on their interaction with the surrounding WT cells, we propose that this remodeling of the monolayer facilitates the progression of Ras^{V12} protrusions, since they grow preferentially at the WT-WT interfaces (see details below).

For both the drug-free condition and the three pharmacological treatments, no significant difference in Ras^{V12} basal actin was observed between the static and stretched conditions (Fig. 5.2a,e). This significant discrepancy with WT cells further demonstrates the mismatch in strain mechanoresponsiveness between Ras^{V12} and WT cells, and is a first hint that the former appear less responsive.

5.3.5 Strain-induced cellular reorientation is different in Ras^{V12} and WT cells

To further demonstrate the strain sensitivity mismatch between Ras^{V12} and WT cells we analyzed cellular reorientation, a common signature of mechanoresponse upon cyclic-stretching. Although it is generally studied in elongated cells such as fibroblasts, it has also been observed in epithelial cells, including in MDCK cells[30,137]. Interestingly, we have found that while WT cells preferentially reorient perpendicular to the stretching direction, Ras^{V12} cells exhibit a nearly random distribution (Fig. 5.3a). These results further support the interpretation that WT cells are more mechanoresponsive to cyclic stretching than Ras^{V12} cells (in the drug-free case). This reorientation mismatch was smaller (or non-existent) upon addition of pharmacological treatments. Fig. 5.3b shows a positive correlation between the reorientation mismatch (Ras^{V12} vs WT) and the degree of Ras^{V12} cell invasiveness for the four pharmacological conditions investigated (DMSO, FAK inhibitor, blebbistatin, and ROCK inhibitor). A greater reorientation mismatch coincides with larger basal protrusions and a lower average Ras^{V12} height. While we do not suggest causality between these parameters, it is consistent with our general results showing that Ras^{V12} and WT cells have a different sensitivity to strain, which plays a key role in triggering invasiveness. Additionally, we found a lower level of basal vinculin intensity in Ras^{V12} cells than in WT cells under cyclic stretching, suggesting differences in the connections between the substrate and F-actin networks[263] (Appendix C, Fig. C.5a,c).

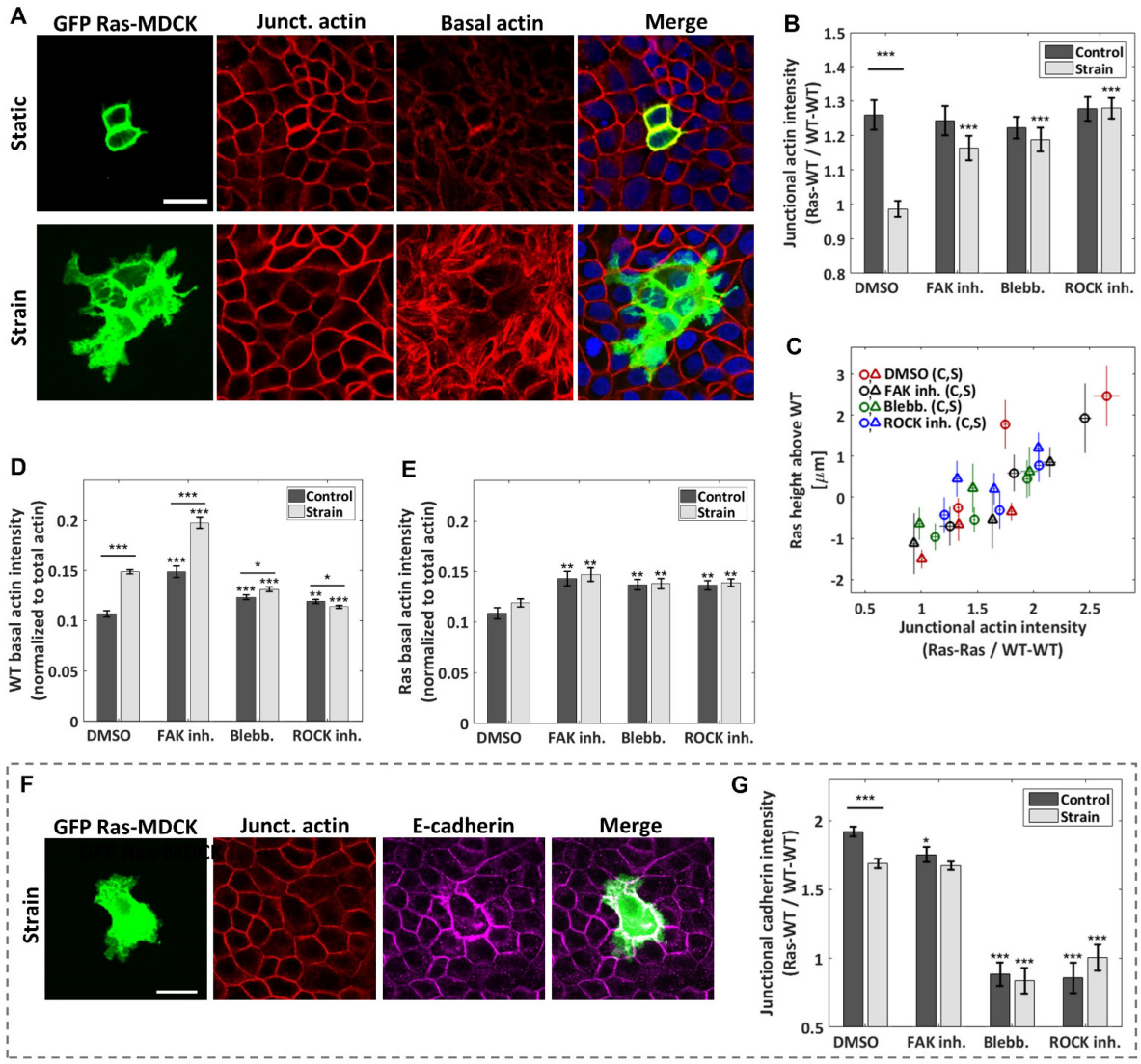

Figure 5.2 Cyclic stretching promotes actin and e-cadherin reorganization differently in WT and in Ras^{V12}-transformed cells. a) Confocal images of the Ras^{V12}-WT culture for a static control (top) and a stretched experiment (bottom). GFP-Ras^{V12} cells are in green. Junctional and basal actin images (red) were obtained as described in the *Materials and Methods* section. Scale bar is 25 µm. **b)** Ratio of the junctional actin intensity, Ras^{V12}- WT interface over WT-WT interface. **c)** Correlation between Ras^{V12} extrusion height and the junctional actin intensity ratio Ras^{V12}- Ras^{V12} over WT-WT. The data from each of the 8 conditions (DMSO and three drugs, static (c) and strain (s)) were separated in three bins each of equal number of cells. **d,e)** Average basal actin intensity of the WT **(d)** and Ras^{V12} **(e)** cells. Both are normalized to the actin intensity summed over all stacks and averaged over the full image. **f)** Representative confocal images of the Ras^{V12}-WT culture under strain showing a GFP-Ras^{V12} cell (green), junctional actin (red) and e-cadherin (magenta). Scale bar is 25 µm. **g)** Ratio of the e-cadherin junctional intensity, Ras^{V12}-WT interface over WT-WT interface. For **b,d,e,g)**, three drugs were tested in addition to the drug-free case (DMSO): FAK inhibitor, blebbistatin, and ROCK inhibitor. Data are mean ± s.e.m. *** P<0.0001, **P<0.005, *P<0.05. Stars above the individual bars relate to the corresponding DMSO control or

DMSO strain condition. Stars above the horizontal lines refer to the significance between the control and strain data. From left to right, n = 43, 48, 29, 44, 56, 56, 53, and 57 images, each from 3 to 4 independent experiments. The average ratios of each image were compiled and they were used to determine the mean and the s.e.m. of the data points reported; the total number of Ras^{V12} cells contained in each set of images is given in Fig. 5.1e,f.

5.3.6 THE SURROUNDING WT CELLS GUIDE THE RAS^{V12} PROTRUSION GROWTH DIRECTION

The ability of transformed cells to grow protrusions is known to facilitate and guide their invasion and progression[247,264,265]. We observed that the application of strain promotes protrusion formation in our model system, although it is as yet unclear what influences their growth direction. We analyzed their orientation with respect to the strain direction and found a nearly random distribution (not shown). Interestingly, we observed that protrusions grow preferentially parallel to the strain-induced basal SF network of the neighboring WT cells (Fig. 5.3d). As the driving force for protrusion growth is associated with the polymerization of localized actin filaments[264], it is possible that less resistance is encountered along that direction. Protrusion formation is thus guided at least partially by their interaction (either mechanical or chemical nature) with the surrounding WT cells, which organization is modified by strains. We also found that Ras^{V12} cell protrusions grow preferentially along WT-WT interfaces (Fig. 5.3c). This effect is particularly pronounced in thinner protrusions. The apparent facilitated protrusion progression under cyclic stretching (Fig. 5.1f) is thus consistent with the strain-induced promotion of the actomyosin contractile apparatus, demonstrated in other studies to weaken intercellular junctions[261]. These findings demonstrate that the structure of the WT monolayer modulates Ras^{V12} protrusion progression under cyclic stretching. They also suggest that the tissues comprising the microenvironement of transformed cells, and importantly the way that they are shaped by physiological forces, are critical in guiding cancer invasion.

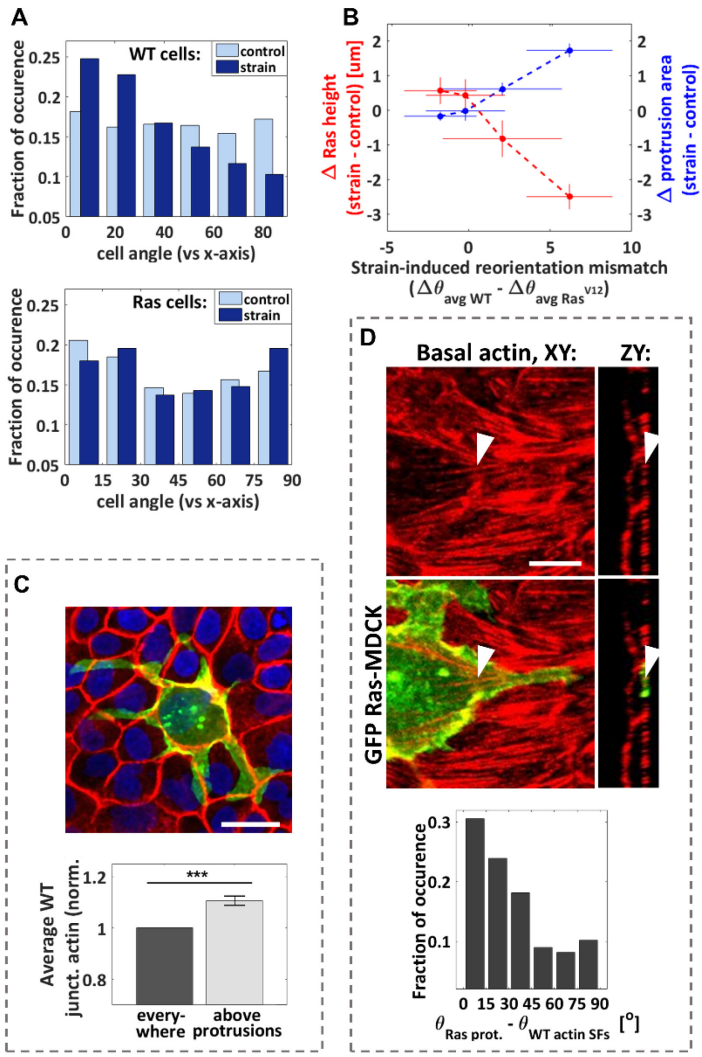

Figure 5.3 Orientation analysis. a) Cellular reorientation response to cyclic stretching. Normalized incidence histogram of the angle difference between the cell body direction and the stretching axis for the WT (top) and Ras^{V12} (bottom) cells. $n_{WT\ control}$ = 5261 cells, $n_{WT\ strain}$ = 5076 cells, $n_{Ras\ control}$ = 287 cells, and $n_{Ras\ strain}$ = 189 cells from 3 independent strain and 3 independent control experiments. **b)** Correlation between the reorientation mismatch and the strain-induced changes in average Ras^{V12} cell height and protrusion area. Each point corresponds to one pharmacological condition (DMSO, FAK inhibitor, blebbistatin, and ROCK inhibitor). The reorientation mismatch is the difference between the strain-induced reorientation of the WT cells ($\Delta\theta_{avg\ WT}$) and that of the Ras^{V12} cells ($\Delta\theta_{avg\ Ras}$), where $\Delta\theta_{avg} = \theta_{avg\ strain} - \theta_{avg\ control}$. When the mismatch is zero, the degree of cell reorientation under strain is the same for Ras^{V12} and WT cells. When it is higher than zero, the reorientation response is greater in WT cells. **c)** Top: rather extreme example of Ras^{V12} cell with protrusions growing preferentially at the WT-WT junctions. Scale bar is 11 µm. Bottom: the average WT junctional actin intensity is greater above the Ras^{V12} protrusions than it is in average elsewhere. Control and strain DMSO conditions combined together, n = 91 images (each image contained 1 to 10 Ras^{V12} cells from 1 to 4 clusters, and hundreds of WT cells) from 3 independent control and 3 independent strain experiments. Data are mean ± s.e.m., ***

P<0.0001. **d)** Top: representative confocal images of basal actin (red) and GFP-Ras^{V12} (green) showing a protrusion growing parallel to neighboring actin SFs. The arrows point at the same SF in two different views. Scale bar is 6 µm. Bottom: normalized incidence histogram of the angle difference between the protrusions and the neighboring WT actin filaments (under strain only). This analysis could not be performed for the static condition due to the scarcity of basal actin filaments in the absence of stretching. n = 190 protrusion segments from 3 independent experiments.

5.4 DISCUSSION

By introducing an external mechanical stimulus which mimics in vivo conditions, we uncoverd a greater potential for invasion of Ras^{V12}-transformed cells. The apical extrusion process is known to involve the generation and transmission of forces via the cytoskeleton and cell-cell adhesions[100,101,112]. Many studies reported that the interactions (mechanical and chemical) between WT cells and transformed epithelial cells drive apical extrusion in a non-cell-autonomous fashion[112,266,267]. The ensemble of our results reveals that substrate deformations act as a critical mechanomachinery regulator which impacts the outcome of these interactions. Strain affects key mechanical structures differently in WT and Ras^{V12} cells, including the cortical actin, e-cadherin, basal SFs, cell body orientation, vinculin, and vimentin (vimentin intensity is higher in Ras^{V12} cells than in WT cell under static condition, but this difference nearly vanishes under strain, see SI Fig. S5). Overall, our results indicate that the different sensitivity to strain of Ras^{V12} and WT cells profoundly impacts the system's dynamic, allowing cells with the Ras^{V12} mutation to invade more aggressively. Removing physiological strains by maintaining the co-culture in a static microenvironment favors elimination of the abnormal cells from the monolayer via apical extrusion (Fig. 4).

Cyclic stretching is known to induce actin cytoskeleton remodeling and increase actomyosin contractility via the activation of the Rho-ROCK signaling pathway, downstream phosphorylation of the myosin light chain kinase (MLCK), and myosin II activation[261]. It is also recognized that reorganization of the cytoskeleton is involved in the process of cancer cell invasion and metastasis[46,104,105]. A direct link has been established between the activation of the Rho signaling pathways (in particular targeting actin remodeling) and the ability of a tumor cell to initiate invasion[265,268]. RhoC and localized RhoA have been shown to play critical roles in protrusion growth[247,268]. Hence, we suggest that cyclic stretching drives the system toward Ras^{V12} invasiveness, at least partially via the Rho pathway through the activation of cytoskeleton-modifying proteins. This is further supported by our observation that pharmacological treatments

inhibiting ROCK or myosin II activity hinder the effects of strain on the system. Interestingly, while ROCK inhibition and ROCK activation (via strain) suppress apical extrusion when applied independently, their combined effects partially restore it. Since both of these conditions are known to interfere with ROCK in opposite ways, it suggests that a precise cytoskeleton mechanical configuration is required to enable apical extrusion.

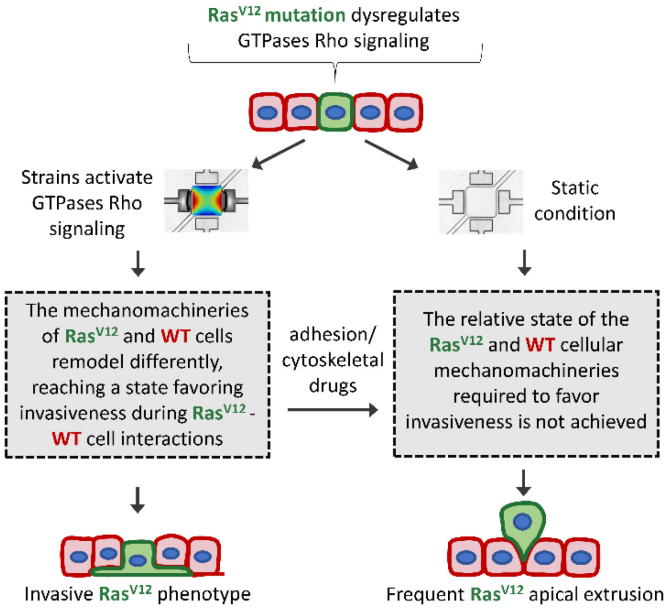

Figure 5.4 Summary of the proposed model.

The process by which transformed epithelial cells escape their primary site is not fully understood. Apical extrusion is the typical mechanism by which epithelial cell turnover takes place. In contrast, oncogenic mutations can alter this process, resulting in basal extrusion, and potentially enabling invasion and escape towards the tissue they envelop[115,244–246]. For instance, K-Ras cells (not studied here) were shown to be predominantly basally extruded via degradation of S1P, preventing the formation of the strengthened contractile belt in the surrounding WT cells[244]. S1P is also known to be required for the H-Ras apical extrusion[267]. Its binding to S1PR2 receptors in WT cells leads to filamin accumulation (a force generator) via the Rho-ROCK pathway. Here we found that although apical extrusion is preponderant in H-Ras cells under static conditions, cyclic stretching drives cell extrusion basally. In light of this, it would be relevant to study the S1P levels in the system to determine if they are involved in the mechanism by which strain promotes basal invasion. It was also proposed in the context of oncogenic expression that basal extrusion could result from the hyperactivation of Rho, which would cause the transformed

cell to contract apically where the highest concentration of actin and myosin II is observed[115]. This is consistent with what we observed in the context of cyclic stretching, but further investigation is needed to further our understanding of the mechanism governing basal extrusion of H-Ras^{V12} cell under strain.

The results described in this work were obtained using an impenetrable solid PDMS membrane as the substrate, which is different from in vivo conditions. Nevertheless, the impact of external forces on Ras^{V12} cell invasiveness is unambiguous in our model system and therefore highlights the importance of exploring in depth this avenue using in vivo models in future studies.

5.5 CONCLUSION

The capacity of epithelia to eliminate newly transformed cells via competition-like processes is a critical defense mechanism to eradicate the initial stage of carcinogenesis. Our results establish a direct link between the presence of external mechanical strains and the inability of normal epithelial cells to apically extrude Ras^{V12} transformed cells in our model system. The latter are also found to exhibit enlarged invasive protrusions upon cyclic stretching. The cytoskeleton and adhesion reorganizations which follow the application of mechanical strains are different in the Ras^{V12} transformed cells than in the surrounding normal cells. This difference in mechanical remodeling seems to favor Ras^{V12} cells in the cell competition. Better understanding of how these mechanically-induced reorganizations are orchestrated in transformed cells and in their normal neighbors could lead to the development of new cancer-preventive treatments, such as the trafficking of mechanical strain pathways. This study shows how external forces can be determinant factors in cancer cell invasion and should therefore be considered in the exploration of potential avenues for preventing the spread of cancer.

5.6 MATERIALS AND METHODS

Microfluidic device and strain characterization. A detailed description of the microfluidic device fabrication and characterization can be found in previously reported work[45]. Briefly, the PDMS (Sylgard184, Ellsworth Adhesives Canada Corporation) microfluidic stretchers were prepared using standard microfabrication techniques, including UV photolithography and soft lithography. Each device contains a thin square suspended PDMS membrane (1.6 mm x 1.6 mm x 10 µm) that is attached to four vacuum chambers (two were used here). The cyclic action of a pair of isolated vacuum chambers (sinusoidal wave form, controlled via a homemade Labview program) deforms

the walls in which the membrane is anchored, thus stretching the latter. The generated strain field pattern is biologically relevant with strain amplitudes varying from 3 to 9 % and strain gradient amplitudes varying from 0 to 12 % mm^{-1}, mimicking in vivo strain non-uniformity [139]. The strain field was locally determined by employing a point-by-point characterization method. Fluorescence beads (FluoSpheres, 200 nm, Invitrogen) were incorporated in the PDMS membrane and imaged for different stretched states (10 states) with an EPI fluorescence microscope (Nikon, Tokyo, Japan). A homemade Matlab program was generated to track the bead displacements and calculate the Green strain matrix elements. The estimated stiffness of the PDMS membrane is 0.5 MPa based on previously reported characterizations of similar PDMS substrates[206,207].

Cell lines, cell culture, and inhibitors. MDCK and MDCK-Ras^{V12} transformed epithelial cells were cultured in Dulbecco's Modified Eagle's Medium (DMEM) supplemented with 10% FBS, 50mg/ml streptomycin, and 50U/ml penicillin antibiotics (Hyclone Laboratories, Logan, UT, USA). Ras^{V12} is a stable MDCK cell line expressing in a tetracycline-inducible manner the oncogene Ras (GFP-tagged)[47]. All the cells were cultured in a standard incubator at 37°C with 5% CO_2, initially on d=100 mm tissue culture dishes (Corning) and then on the microfluidic stretcher membranes. Prior to seeding the cells into the microdevice, the PDMS membrane was air-plasma treated (Glow Research, Tempe, AZ, USA) at 70 W for 5 minutes. Sterilization and washing were performed by flowing 70% ethanol for 5 minutes followed by autoclaved phosphate buffered saline (PBS) solution for another 5 minutes. The membrane was then coated with Rat-tail collagen I (5 µg cm^{-2}, Gibco) for 4 hours and rinses with PBS. A solution of suspended cells (ratio of 1:75 Ras^{V12} to WT) was injected into the device and incubated for 10 hours to grow the monolayer. Cyclic stretching of the well-adhered co-culture was initiated immediately after Ras^{V12} activation with tetracycline (2µg/ml). The monolayer was stretched for 24 hours at 1 Hz in the incubator. Inhibition studies of focal adhesion kinase (PF-573228, 10 µM, Selleckchem Inhibitor Expert, catalogue no. S2013), Rho-kinase (Y-27632; 10 µM, Sigma, catalogue no. Y0503), and myosin-II (blebbistatin; 10 µM, Sigma, catalogue no. B0560), were achieved by exposing the cells immediately before stretching. The pharmacological treatments used were stored in dimethyl sulfoxide (DMSO) stock solutions. The drug-free experiments were supplemented with 0.1% DMSO.

Immunofluorescence Microscopy. Prior to DNA, actin, and e-cadherin staining, cells were fixed with 3.5% paraformaldehyde (15 min) and permeabilized with Triton X-100 (3 min) at 37°C. The DNA was labelled with DAPI (Invitrogen, catalogue no. D1306), the actin with phalloidin

conjugated to Alexa Fluor 546 (Invitrogen, catalogue no. A22283), and the e-cadherin with monoclonal rat anti-e-cadherin (Sigma, catalogue no. U3254) primary antibody followed by polyclonal anti-rat IgG secondary antibody conjugated CF-647 (Sigma, catalogue no. SAB4600186). Standard staining protocols were adapted to suit the microdevice environment. The details of these protocols, as well as the vimentin and vinculin staining methods, are given in the Appendix C. On-chip cell imaging was carried on with a long-distance 25x objective (NA=1.1) and an upright laser scanning multiphoton confocal microscope (Nikon A1RsiMP). The fluorescence signal of the images presented here have been optimized by adjusting the brightness/contrast settings using the program ImageJ. The despeckle function has only been used on images showing large cell components to remove salt and pepper noise. The maximum intensity z-projection of either the full stack or of a subset of slices is shown depending on the element of interest.

Data analysis. Statistical significances were determined using unpaired two-tailed Student's *t* tests, assuming unequal variances. The number of samples and the number of independent experiments are specified in each figure. The image analysis was performed using homemade Matlab programs making use of the image processing toolbox. A detailed description of the image analysis is included in the Appendix C.

5.7 ACKNOWLEDGEMENTS

This work was supported by individual Natural Sciences and Engineering Research Council (NSERC) Discovery Grants to M.G. and A.E.P. S.C-L. was supported by NSERC Postgraduate Scholarships-Doctoral (PGS D). M.G. acknowledges support from the Ontario Ministry of Research and Innovation, and the Canada Foundation for Innovation (CFI). A.E.P. gratefully acknowledges generous support from the Canada Research Chairs (CRC) program. We thank professor Yasuyuki Fujita (Hokkaido University) for providing the Ras^{V12} cell line.

CHAPTER 6 | CONCLUSION

The studies presented in this thesis highlight the importance of integrating increasingly complex physical conditions when performing cellular studies, in order to better reflect how our bodies are constructed. This was first accomplished by developing versatile microfluidic devices to implement complex physiological strains to the substrate, while retaining near diffraction-limited imaging capabilities. Secondly, these micro-engineered stretchers were employed to gain insight into the influence of mechanical forces on the organization and function of cell populations.

Our work revealed that a cell can sense if one side of its body is being more stretched than the other. We showed that the presence of strain gradients triggers the reorientation of the cell body and its actin stress fibers in such a way as to avoid discrepancies in stretching amplitude. This coordinated cellular response suggests that mechanical cues, which are transmitted to the actin network via the FAs, are processed according to their respective location and amplitude through intracellular communication. We also demonstrated that even smaller structures like FAs align in accordance with the global cell body response, rather than with the direction of the local external force applied to them. We suggested that FA alignment is guided by the feedback cues coming from the actin cytoskeleton pulling on them. Overall, this study shows how cells, far from being ensembles of independent components executing individual functions, rather exhibit a high level of organization with intricate networks of interactions. Cellular constituents are completely interdependent, making the cell an integrated whole.

In another study, we demonstrated that the history of mechanical cues can influence the apparent pattern of cellular response. Importantly, our work showed that cells can decouple the different components of a complex strain field (the strain and its gradient) and operate distinct mechanoresponses that occur on different time-scales. We suggested that the slower response to the strain gradient involves complex transduction mechanisms, potentially requiring the creation of an intracellular gradient of biochemical cues. This hypothesis can be tested in future work by monitoring the location and density of key proteins such as certain GEFs and Rho GTPases. Furthermore, future studies could also consider biochemical cell-cell communication in our non-uniform mechanical environment, to assess the potential role of the paracrine effect. Another important question remains. What are the cellular functions regulated by the strain gradients? Answering these questions might shed light onto certain pathologies caused by

mechanotransduction dysregulation. Better understanding the molecular mechanism of gradient mechanotransduction and identifying the physiological processes that it regulates could eventually lead to the development of new therapies.

In future studies, it would be of interest to build a mechanistic model to collectively explain the observations of Chapters 3 and 4. Various models predicting the cell orientation in response to uniform strains have been developed, but many of them considered the cell as a 1D object. In order to sense strain gradients, these models would likely require to be extended to 2D and consider remodeling of sub-cellular structures. For example, certain models approximate the cyclically stretched cell as a dipole[168,169]. They consider an effective free energy which is minimized when the cell (via regulation of its contractile activity) aligns such as to maintain an optimal stress component (homeostatic set point) in the adjacent matrix. To address the gradient avoidance, another internal energy term could be added to tune this homeostatic set point, in addition to extend the model to 2D. Many of the current strain models consider an amplitude threshold (that we observed to be around 3%) below which no stretching avoidance is observed. Therefore, a small deviation from the strain-determined homeostatic set point, to accommodate the gradient avoidance, would not cause a major strain-related energy penalty for the cell. In Chapter 3, one of the hypotheses that we proposed to explain gradient sensing was the creation of an intracellular gradient of signaling events. Since the local signaling activity regulates the local actin remodeling[77], we can hypothesize the creation of asymmetries in the cytoskeleton organization and density throughout the cell in the presence of a strain gradient. A previous study supporting this hypothesis has reported a gradient in the actin SFs density under strong strain gradient amplitudes[180]. Given that some existing strain models consider the elastic energy stored in the SFs[170], the new gradient model could take into account such asymmetric spatial distribution of the SFs-associated energy and minimize it. Since the internal energy terms associated with the gradient would depend strongly on the evolution of sub-cellular structures, this model could reproduce the slower gradient response observed in Chapter 4.

The last chapter of this thesis further showed the importance of integrating physical considerations to the existing landscape of cellular biochemistry research. This is crucial for understanding how cellular behaviors determine the fate of much larger systems, such as our organs or our whole body, especially in the context of human diseases. As mentioned previously, numerous currently incurable diseases result from mechanotransduction defects. The last chapter

demonstrated with a cancer cell model system that external mechanical forces can greatly promote the invasiveness of transformed cells in the early stage of development and jeopardize the defense mechanism of neighboring healthy cells. It also showed that such physical cues have profound impacts on cytoskeleton and adhesion configurations. Mechanoresponse differences between the healthy and transformed cells were shown to correlate with the extent of invasion, thus exposing the critical role of mechanotransduction dysregulation. Our results also suggest that the effect of strain on the invasion of transformed cells is driven in part by the Rho/ROCK pathway. Future research directions include testing different inhibitors to traffic this signaling pathway in order to bypass the effect of physical cues on the early stages of cancer propagation.

In the past decades, advances in microfabrication and microfluidics have enabled the development of functional platforms precisely reproducing ensembles of in vivo conditions that are critical for various biological systems. Progress in this area has led to a better understanding of many human pathologies, to drug discoveries, and to better predict the human response to drugs during preclinical assays. Our work, in particular in Chapter 5, fits in this line of research. Various improvements can be implemented to our microstretcher depending on the system under study. For example, replacing the thin elastic membrane by a 3D stretchable scaffold would allow to investigate how our results carry over from a 2D to a 3D microenvironment. Such scaffold would also allow to construct more complex biological models, for example by layering various types of tissues. Another possible research avenue is to use a porous membrane in the context of our transformed cell study. This could reveal whether or not basally invading transformed cells end up being completely basally extruded (in our model this would correspond to cells escaping towards the organ). In the future, using a wide range of cell types coming from different organs (e.g. lung, heart, intestine) and employing microenvironments better reproducing in vivo conditions (e.g. stiffness, porosity, cellular heterogeneity, matrix dimensionality) will reveal if strain-induced invasiveness is a specific response of epithelial kidney cells or if mechanical forces are a determining factor for transformed cells progression throughout the body. Finally, the current design of our microstretcher permits to study the impact of fluid shear stress gradients on the cellular behavior, due to the velocity profile of the flow in the cell chamber. It would be particularly interesting to study the combined effect of non-uniform strain and flow fields on blood vessel cells, for instance.

The aforementioned technology developments have allowed us to better understand the interplay of physics and cell biochemistry. Through different investigations, we revealed new aspects of how mechanical coupling of the ECM and the cells orchestrates cellular fate. In the same way that we were inspired by a vast number of studies in this field, we hope that other research groups will build upon our work in the ongoing quest for uncovering how force-induced cellular responses impact biological systems.

APPENDIX A – SI OF CHAPTER 3

Supplementary information for the manuscript entitled: “Cellular Orientation Is Guided by Strain Gradients” of Chapter 3.

A.1 ADDITIONAL DETAILS ON THE MICRODEVICE WORKING PRINCIPLE AND FABRICATION

As presented in Fig. A.1a, when the device is in the relaxed state, the cells are not subjected to external stretch (no strain). The sinusoidal activation of the vacuum chambers cyclically deforms the thin PDMS walls separating the vacuum chambers from the cell chamber, which in turn pull on the elastic PDMS membrane. Additional schemes of the device are presented in Fig. A.1b. The microdevice is composed of three PDMS layers, namely a thin membrane bounded between a top and a bottom pieces. They were fabricated and assembled in the following way. The membrane was made by spin coating PDMS on a silicon wafer prior to curing it. The top and the bottom parts were molded by soft lithography using PDMS on a micro-fabricated master mold. The latter was obtained through UV photolithography process, which allowed the transfer of a pattern from a printed photomask (see Fig. A.1a) onto a light sensitive SU-8 2050 negative photoresist (Microchem, MA, USA). Two photoresist layers were deposited onto a clean silicon wafer to achieve the thickness required to mold the channels (340 µm). The cell chamber was further extended to a height of 2 mm, using additional PDMS sub-molds, to facilitate direct cell access during the staining and imaging procedures, once the stretching experiments were completed. The complete fabrication procedure and description of the advantages of this technique are described in details elsewhere (article in preparation). Finally, the three separate PDMS layers (top, bottom, and membrane) underwent an air-plasma treatment prior to being aligned and assembled using a mask aligner (OAI, CA, USA).

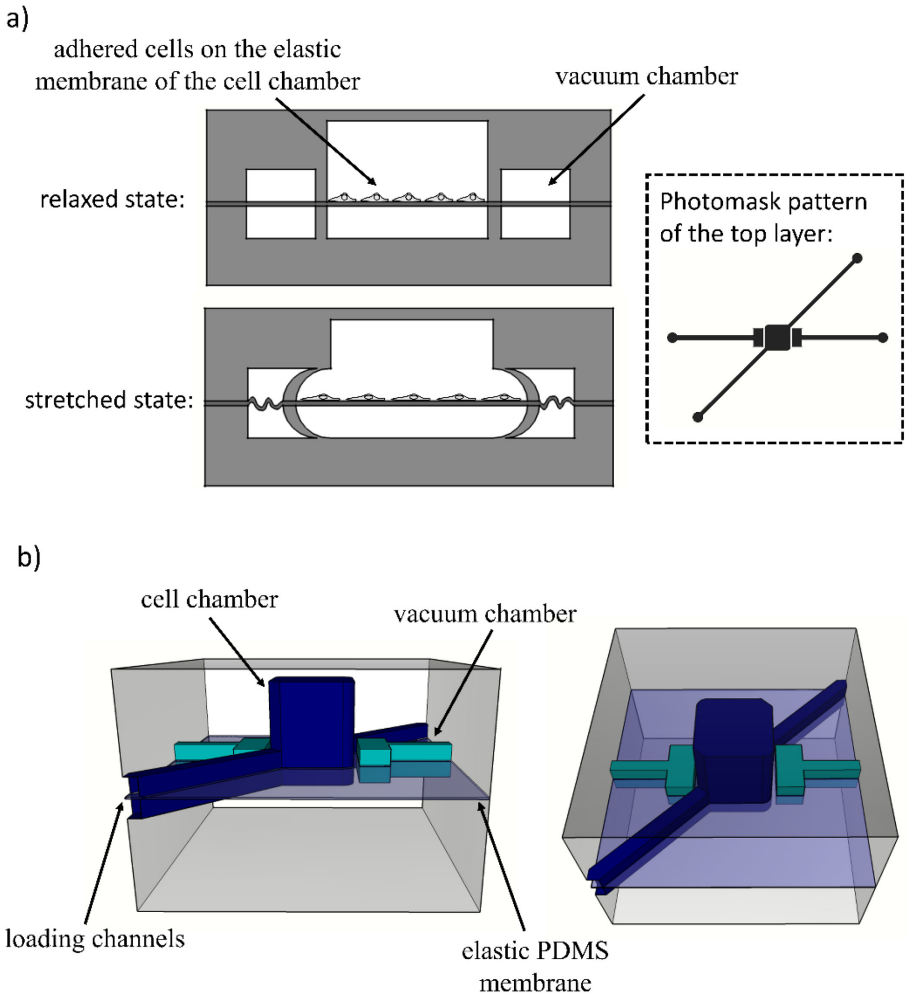

Figure A.1 Microdevice geometry. a) Left: simplified scheme of the device (cross section) demonstrating its working principle. Right: photomask pattern of the top layer. **b)** 3D schemes of the device. The dimensions of the cell chamber's membrane are 1.6 mm x 1.6 mm x 10 µm. Note that the device's cell chamber can be opened at the end of the stretching experiment to facilitate fluorescent staining and high-resolution imaging.

A.2 Addition details on the membrane strain field calculation

The beads displacements were tracked with a homemade Matlab program in which the Green strain matrix elements (ε_{xx}, ε_{yy}, and ε_{xy}) are calculated for each initial bead position. The $\varepsilon_{xx}(x, y)$, $\varepsilon_{yy}(x, y)$, and $\varepsilon_{xy}(x, y)$ fields were interpolated and boxcar smoothed throughout the membrane area (the membrane was divided into cells of ~0.6 µm^2). The extracted strain fields of five devices were averaged together, as well as with their mirror images, to provide accurate strain fields representations of the overall device collection used for the experiments. The standard deviation

of the devices characterized (averaged over the membrane surface) was approximately 9%. The maximum and the minimum principal strains $\varepsilon_1(x,y)$ and $\varepsilon_2(x.y)$ were computed by diagonalizing the position-dependent Green strain matrices. For each point of the membrane, this process allows the determination of a coordinate system for which there is no shear strain, through the extraction of the eigenvectors. The eigenvalues are calculated from the matrices and correspond to the principal strain amplitudes $\varepsilon_1(x,y)$ (maximum strain) and $\varepsilon_2(x.y)$ (minimum strain). The direction of the maximum stretch $\theta_{\mathrm{strain}}(\mathrm{x},\mathrm{y})$ at each point, which is called principal strain direction, is given by the direction of the eigenvector $\varepsilon_1(x,y)$. Finally, the gradient of $\varepsilon_1(\mathrm{x},\mathrm{y})$ was then calculated to obtain the gradient amplitude $|\nabla\varepsilon_1(\mathrm{x},\mathrm{y})|$ and gradient angle $\theta_{\mathrm{gradient}}(\mathrm{x},\mathrm{y})$ maps (see Figure 3.1b). Both $\theta_{\mathrm{gradient}}(\mathrm{x},\mathrm{y})$ and $\theta_{\mathrm{strain}}(\mathrm{x},\mathrm{y})$ were kept between 0 and 180 degrees. The strain field analysis was also performed using a homemade Matlab program.

A.3 IMMUNOFLUORESCENCE STRAINING IN A MICRODEVICE

Since the cells were contained in microdevices, two effects must be taken into account during the staining procedures. First, the fluid mixing is low in the cell chambers due to the microscale nature of the fluid volumes. Second, the loss of photons from PDMS scattering and surface reflection can weaken the fluorescent signal during the image acquisition. We found that doubling the incubation time of every straining step was sufficient to obtain good image quality. In between every step, the samples were also incubated in washing buffer (PBS solution with 5% horse serum) for 30 min.

A.4 Membrane regions, number of cells, and number of FAs analyzed in different figures of the manuscript

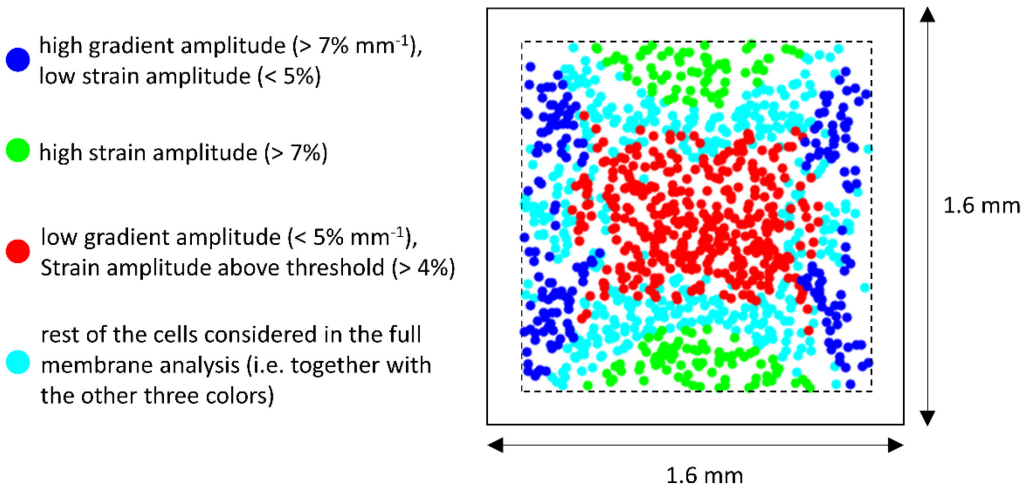

Figure A.2 Regions analyzed in the histograms displayed in Figure 3.2 of the manuscript and in Figure A.3 of the Appendix A. The location of the cells corresponding to 6 cyclically stretched experiments are superimposed together. The legend on the left specifies the strain and strain gradient amplitudes conditions associated with each color. Fig. 3.2a and Fig. A.3a were generated with the cells of all 4 colors; Fig. 3.2b was generated with the cells shown in green; Fig. 3.2c,d were generated with the cells shown in dark blue; Fig. A.3b was generated with the cells shown in red.

Pharmacological treatments	Regions of the membrane	Corresponding figures	Number of cells in varying strain field (2-10%)	Number of cells in control (0% strain)
Control (DMSO 0.1%)	Full membrane	3.2a and 3.3a-c	1078	1244
	High strain	3.2b	132	200
	High gradient, low strain	3.2c,d	181	187
	Low gradient	A.3	366	409
Blebbistatin (10µM)	Full membrane	3.4b	1319	1091
CalA (2 nM)	Full membrane	3.4a	1231	1255

Table A.1 Number of cells analyzed in different figures.

Pharmacological treatments	Regions of the membrane	Corresponding figures	Number of FAs in varying strain field (2-10%)	Number of FAs in control (0% strain)
Control (DMSO 0.1%)	Full membrane	3.5a	7568 (61 cells)	2607 (35 cells)
Blebbistatin (10µM)	Full membrane	3.5c	1904 (62 cells)	889 (29 cells)
CalA (2 nM)	Full membrane	3.5b	5164 (71 cells)	4119 (44 cells)

Table A.2 Number of FAs analyzed in different figures.

A.5 CELL ORIENTATIONS REPORTED WITH RESPECT TO THE X-AXIS

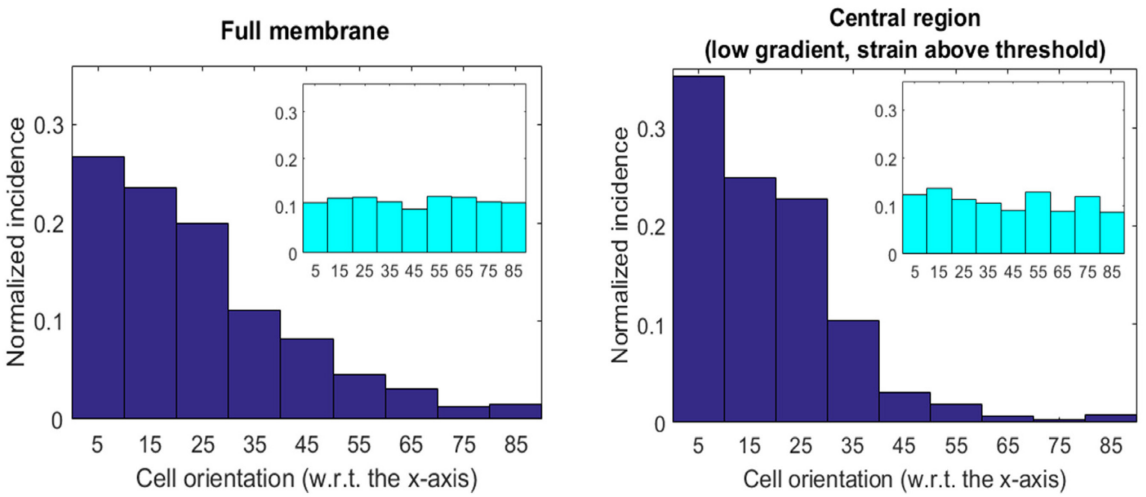

Figure A.3 Reorientation analysis of the HFF cells after 11 hours of cyclic stretching along the y-axis. Normalized incidence histograms of the cell body orientation with respect to the x-axis considering the full membrane **(left)** and the central region **(right)** (more specifically the region for which the strain gradient amplitude is lower than 5 %mm^{-1} and for which the strain amplitude is greater than 4 %). It should be emphasized that in contrast to the histograms presented in the manuscript, it is the cell body orientations which are reported, rather than the cell normals, and a unique axis is considered rather than reporting each cell with respect to its local principal strain direction. Each histogram comprises the combination of 6 unstretched control experiments (insets, shown in turquoise) as well as the combination of 6 cyclically stretched experiments (shown in dark blue).

APPENDIX B – SI OF CHAPTER 4

Supplementary information for the manuscript entitled: “Time dependence of cellular responses to dynamic and complex strain fields” of Chapter 4.

B.1 ADDITIONAL DETAILS ABOUT THE MICROFLUIDICS DEVICE

The microfluidics device was designed in such a way as to enable the simultaneous generation of biologically relevant strain and strain gradient amplitudes (varying from 2% to 10%, and from 0% mm^{-1} to 14% mm^{-1}, respectively). For a given non-uniform strain pattern, the achieved gradient amplitudes scale inversely with the device dimensions. Therefore, it would be possible to generate higher gradient amplitudes without increasing the strain amplitude (~10% being known as a cell responsive amplitude range[35,36,142]), simply by further scaling down the microdevice pattern. To study different cell mechanisms under strain gradients, microstrecher devices are thus better suited than their macro counterparts. Using arrays of cell chambers allows for high throughput fabrication and experiments, and their currently partially coupled channels could easily be re-designed for independent control if needed. Figure B.1a shows the working principle of the microstretcher. The vacuum chambers are periodically contracting and concurrently stretching the thin PDMS membrane on which cell are cultured.

B.2 PHOTORESIST DEVELOPMENT PROCEDURE FOR THE MASTER MOLD FABRICATION

Clean, uniform, and fully developed photoresist trenches could not be obtained by using manual shaking (or ultra-sonic bath) of the solution during the development process. We used a simple, efficient, and low-cost strategy to overcome difficulties associated with the thickness of the SU-8 layers (see figure B.1b). We simply attached the master mold wafer to a stirring bar and immersed it in a beaker filled with developer solution. The speed of the stirring plate was set to 400 rmp. This method was found to be gentle on fine SU-8 structures (and thus ensure features’ integrity) while creating a fast-rotational motion of the solution such as to maximize the development process.

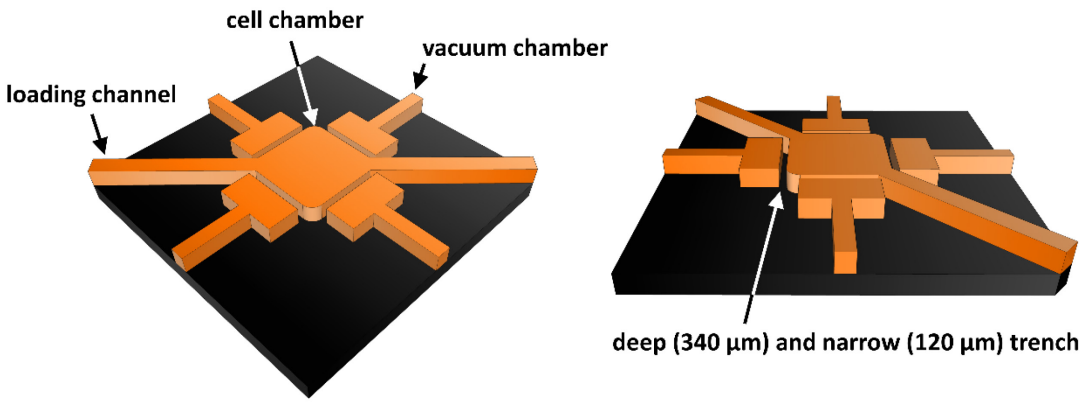

Figure B.1 Microfluidics SU-8 master mold. Representation of the SU-8 master mold (cropped view) showing the different parts of the design. The deep trenches between the cell chamber and the vacuum chambers require a special development procedure.

B.3 PDMS PILLARS FABRICATION METHOD

In order to fabricate the PDMS pillars, micro-milled aluminum molds were employed. Two important designing aspects need to be considered. First, the PDMS shrinks[269] during the curing process (with our conditions, we increased all three pillar dimensions by ~1.5% to compensate for shrinking). Second, it is advantageous to include error margins to loosen the centering/positioning requirements onto the SU-8 features of the master (we decreased the pillar depth and width by ~10%). To fabricate the PDMS pillars from the aluminum mold, uncured PDMS was simply poured into them and then degassed in a vacuum chamber. To ensure the production of pillars having all six surfaces flat, the top surface of the mold was then closed. A non-frosted acetate sheet was positioned directly onto the uncured PDMS (to facilitate demolding) after which a glass slide and a 500 g weight were placed on top of the acetate sheet to ensure a flat surface and to expelled extra PDMS, respectively (see Figure 4.6d). After curing and demolding, the PDMS pillars were chemically treated to prevent them from bounding to uncured PDMS during the fabrication of the device's top layer. This chemical treatment consists in i) an air-plasma treatment (70W, 5 min), ii) two hours of soaking in methanol with 2% Trichloro(1H,1H,2H,2H-perfluorooctyl)silane (Sigma-Aldrich) and iii) one hour of heating at 100°C to ensure solvent evaporation.

B.4 ADDITIONAL DISCUSSION ON THE ADVANTAGES OF USING AN OPEN-TOP DEVICE FOR FLUORESCENCE IMAGING

In the most common cases of oil-immersed objectives or water-dipping objectives, near-diffraction limited resolution requires the refractive index (n) to be approximately constant

between the objective and the sample, namely ~1.52 or ~1.33, respectively. In both cases, the introduction of a PDMS layer (n≈1.42)[148] is thus highly detrimental. Certain water-immersion objectives have correction rings which can compensate for the introduction of glass coverslips up to 0.17 mm thick and which could partially compensate for the spherical aberrations introduced by a PDMS layer. However, the latter are generally too thick and more importantly too non-uniform in practice. Non-uniformities in the thickness or density of even a thin refractive index mismatched layer result in image deterioration[237,270]. Moreover, water-immersion objectives with correction rings are significantly more expensive than the other types mentioned above. For this reason, and because complex staining procedures strongly benefit from having an open access to the cell chamber, the alternative of using a permanently closed glass-top microstretcher, rather than an all-PDMS device with removable top, is not optimal in many contexts.

B.5 ADDITIONAL DETAILS ABOUT THE STAINING AND IMAGING PROCEDURES

The microfluidics top membrane (which acts like a lid to close the cell chamber) was peeled off prior to the performing the staining and imaging procedures. The cells were fixed using 3.5% PFA for 10 minutes and permeabilized with 0.5% TritonX-100 for 3 minutes. Phalloidin conjugated to Alexa Fluor 546 (Invitrogen) and DAPI (Invitrogen) were respectively employed to stain the actin filaments and the DNA. Vinculin was stained with a monoclonal mouse anti-vinculin antibody and a rabbit anti-mouse IgG secondary antibody conjugated to Alexa Fluor 488 (Invitrogen). Details of the staining procedures have been previously published[216,217]. Minor modifications were required to take into account the fact that cell staining is performed within the microdevices. The incubation time of every staining and washing (PBS solution with 5% horse serum) steps was doubled. This procedure was found to compensate for the low fluid mixing taking place in the cell chamber, as well as for the loss of photons arising from PDMS scattering and surface reflection during fluorescence imagining. After staining, the cells were immersed in cold PBS solution and imaged with an upright laser scanning multiphoton confocal microscope with a long working distance 25x objective (NA=1.1).

B.6 ALTERNATIVE METHODS TO FABRICATE THE TOP PDMS LAYER

Fabrication methods investigated	Pros	Cons and fabrication difficulties
3D printed mold to replace the SU-8/Si master mold	• simple • no height limitations	• typically lower resolution • material not necessarily compatible for PDMS molding
Strategic photoresist layering and UV exposition patterning	• retains high resolution	• heights achievable typically limited to a few hundred microns • increasingly challenging when the number of different heights needed augments
Fabricating two distinct SU-8 masters (in order to fabricate two distinct layers instead of one with multiple feature heights)	• can retain high resolution	• heights achievable typically limited to a few hundred microns • requires additional alignment and plasma bounding steps involving thin (easily-deformable and damageable) layers;
Post-fabrication punch-holes	• Simple and fast	• low resolution • generally limited to circular holes • compromises the layer's integrity and leaves residues on the hole's edge • no microfluidics
Post-fabrication laser ablation	• high flexibility with respect to the shape and depth ablated • high resolution possible	• requires a complex positioning and monitoring setup as well as access to an appropriate laser [PDMS is transparent over a large range of wavelengths[271]; it would require either a UV laser (<300 nm) for single-photon absorption, or a longer wavelength femtosecond laser (near-infrared or visible) for multiphoton absorption] • potential melting damages
Sub-molds (PDMS, metal, or other) glued to the SU-8 features	• no height limitations	• high possibility of damaging the mold with the introduction of glue • all glue tested had poor adhesion with the SU-8 • potential toxicity (glue residues) for the cells
Chemically-treated PDMS sub-molds positioned on the SU-8 features	• simple, cheap, and fast • high success-rate • no height limitations;	• More challenging when higher resolution (~sub-50 um) features are desired

Table B.1 Fabrication methods investigated to produce varying feature heights within a single PDMS layer.

APPENDIX C – SI OF CHAPTER 5

Supplementary information for the manuscript entitled: “Mechanical strains drive newly transformed epithelial cells toward invasiveness” of Chapter 5.

C.1 ADDITIONAL FIGURES

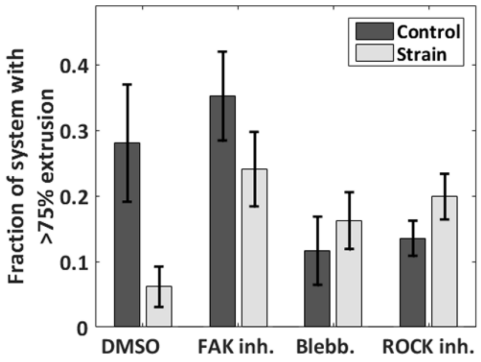

Figure C.1 Effect of mechanical strain on Ras^{V12} apical extrusion. The apical extrusion is quantified here by the fraction of the Ras^{V12} cell clusters in which at least 75% of the cells are above the average surrounding WT height. In addition to the drug-free case (DMSO), three drugs were tested: FAK inhibitor, blebbistatin, and ROCK inhibitor. From left to right: n = 234, 188, 78, 139, 268, 233, 237 and 334 cells each from 3 or 4 independent experiments. Data are mean ± s.e.m.

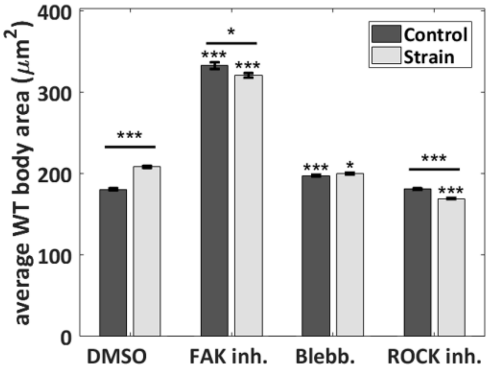

Figure C.2 Effect of mechanical strain on the WT cell body size (µm^2). In addition to the drug-free case (DMSO), three drugs were tested: FAK inhibitor, blebbistatin, and ROCK inhibitor. Data are mean ± s.e.m. *** P<0.0001, **P<0.005, *P<0.05. Stars immediately above the individual bars relate to the corresponding DMSO control or DMSO strain condition. Stars above the horizontal lines refer to the significance between the control and strain data. For each bar, n>2000 from 3 to 4 independent experiments.

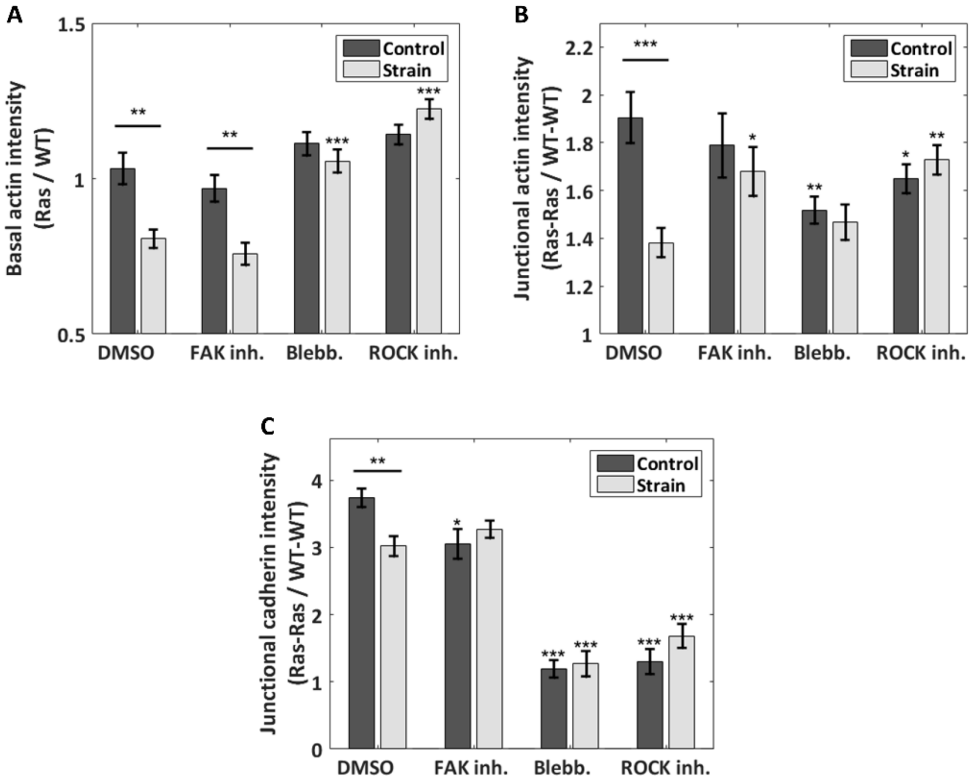

Figure C.3 Effect of mechanical strain on different actin and e-cadherin ratios. a) Ratio of the basal actin intensity, Ras^{V12}/ WT cells. **b)** Ratio of the junctional actin intensity, Ras^{V12}- Ras^{V12} interface over WT-WT interface. **c)** Ratio of the junctional e-cadherin intensity, Ras^{V12}- Ras^{V12} interface over WT-WT interface. In addition to the drug-free case (DMSO), three drugs were tested: FAK inhibitor, blebbistatin, and ROCK inhibitor. Data are mean ± s.e.m. *** P<0.0001, **P<0.005, *P<0.05. Stars immediately above the individual bars relate to the corresponding DMSO control or DMSO strain condition. Stars above the horizontal lines refer to the significance between the control and strain data. From left to right, n = 43, 48, 29, 44, 56, 56, 53, and 57 images, each from 3 to 4 independent experiments. The average ratios of each image were compiled and they were used to determine the mean and the s.e.m. of the data points reported; the total number of Ras^{V12} cells contained in each set of images is given in the caption of Fig. C.1.

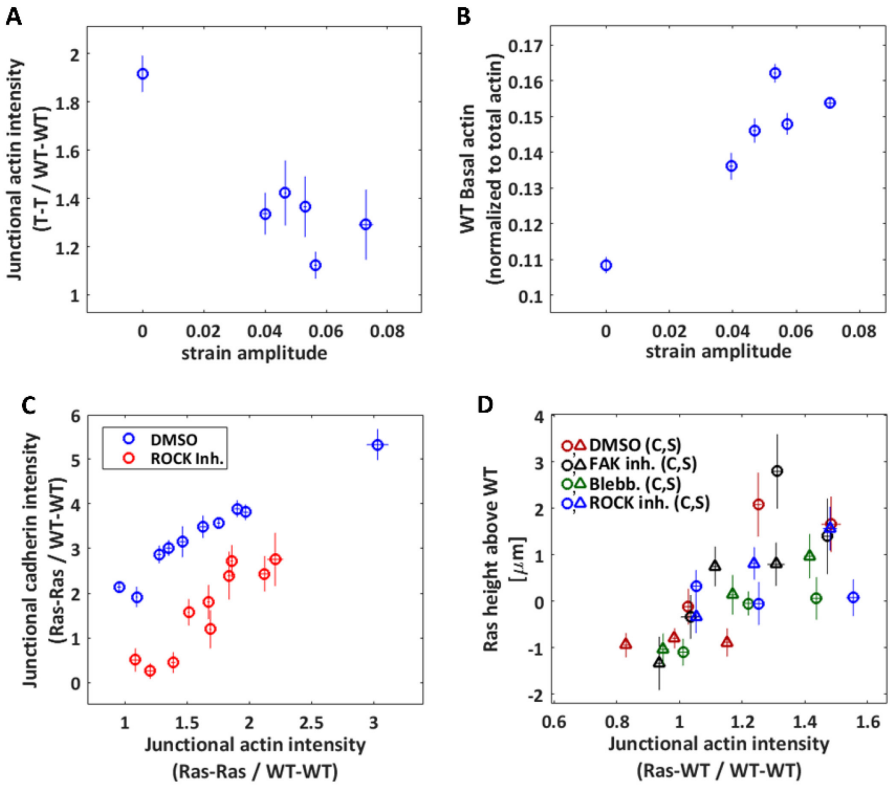

Figure C.4 Junctional intensity of different cell components. a) Junctional actin intensity, Ras^{V12}–Ras^{V12} interface over WT - WT interface, as a function of the local strain amplitude, for the DMSO (drug-free) condition. **b)** WT basal actin intensity as a function of the local strain amplitude, for the DMSO (drug-free) condition. For **a)** and **b)**, the zero-strain points correspond to the average of the control data, and the non-zero strain points were obtained by binning the data of the stretched experiments into five bins each containing an equal (37-38) number of cells. **c)** Junctional e-cadherin intensity, Ras^{V12}- Ras^{V12} interface over WT-WT interface, as a function of the junctional actin intensity, Ras^{V12}- Ras^{V12} interface over WT-WT interface, for the DMSO (drug-free) and ROCK inhibitor conditions. The points were obtained by binning the data from the control and stretching experiments each into 5 bins containing an equal number of cells (37-67). **d)** Correlation between Ras^{V12} extrusion height and the junctional actin intensity ratio of Ras^{V12}- WT interface over WT-WT interface. The data from each of the 8 conditions (DMSO and three drugs, static (c) and strain (s)) were separated in three bins each of equal number of cells (see Chapter 5 Fig. 5.1e for the number of cells analyzed). Data are mean ± s.e.m.

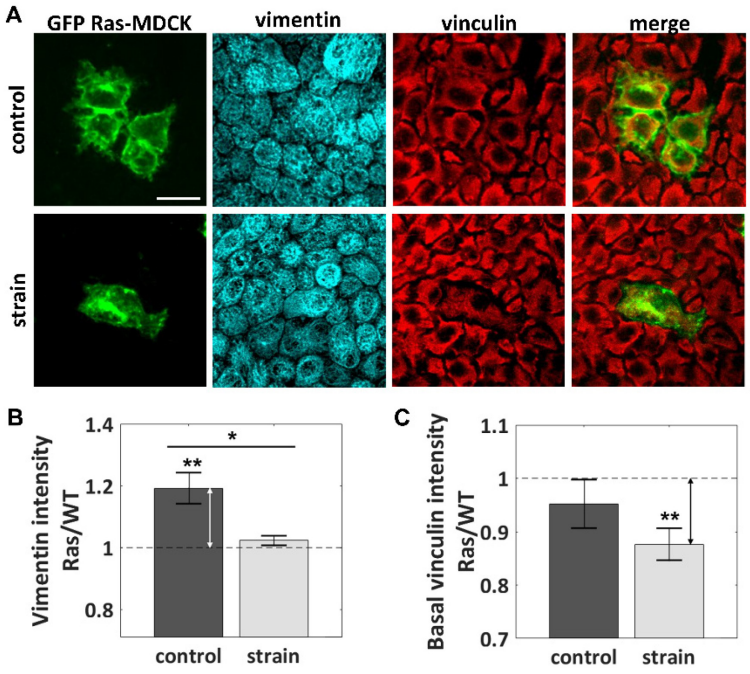

Figure C.5 Representative confocal fluorescence images of the Ras^{V12}-WT MDCK culture showing GFP-Ras^{V12} cells (green), vimentin (cyan), and basal vinculin (red) for the control and the strain DMSO conditions (a). Scale bar is 30 µm. **b)** Ratio of the vimentin intensity, Ras^{V12} cells over WT cells, for the control and the strain DMSO conditions. **c)** Ratio of the vinculin basal intensity, Ras^{V12} cells over WT cells, for the control and the strain DMSO conditions. **b,c)** Data are mean ± s.e.m. *P<0.05, **P<0.005. Stars immediately above the individual bars refer to the statistical significance between the ratio observed and a ratio of 1. Stars above the horizontal lines refer to the significance between the control and strain data. The number of control and strain images that were analyzed were $n_{control}$=16 and n_{strain}=18, each from 3 independent experiments.

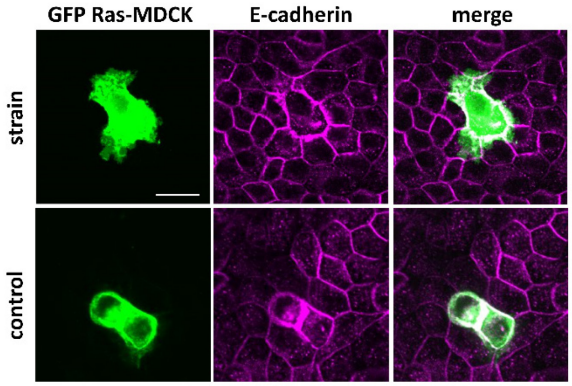

Figure C.6 Representative confocal images of the Ras^{V12}-WT culture showing a GFP-Ras^{V12} cells (green) and e-cadherin (magenta) for the control and the strain DMSO conditions. Scale bar is 25 µm.

C.2 STAINING PROCEDURES

Cell structures	Excitation λ [nm]	Fixation method	Staining method	Product ID
DNA	358	PFA or Methanol	DAPI	Invitrogen, catalogue no. D1306
Actin	546	PFA	Phalloidin conjugated to Alexa Fluor 546 (1:100 dilution for 30 min)	Invitrogen, catalogue no. A22283
E-cadherin	647	PFA	**1)** Monoclonal anti-e-cadherin primary antibody produced in rat (1:1000 dilution for 30 min) **2)** Polyclonal anti-rat IgG (H+L) secondary antibody conjugated CF-647 produced in goat (1:200 dilution for 30 min)	**1)** Sigma, catalogue no. U3254 **2)** Sigma, catalogue no. SAB4600186
Vinculin	546	Methanol	**1)** Monoclonal anti-vinculin primary antibody produced in mouse (1:200 dilution for 30 min) **2)** Anti-mouse IgG secondary antibody conjugated to Alexa Fluor 546 fluorophore produced in goat (1:200 dilution for 30 min)	**1)** Sigma, catalogue no. V9131 **2)** Invitrogen, catalogue no. A11003
Vimentin	647	Methanol	**1)** Monoclonal anti-vimentin primary antibody produced in rabbit (1:500 dilution for 30 min) **2)** Anti-Rabbit IgG (H+L) secondary antibody conjugated to Alexa Fluor Plus 647 (1:200 dilution for 30 min)	**1)** Abcam, catalogue no. AB92547 **2)** Invitrogen, catalogue no. A32733
GFP-Ras	488	PFA or Methanol	NA	NA

Table C.1 Staining procedure summary. The PFA fixation method consists in employing 3.5% paraformaldehyde for 15 min at 37°C and Triton X-100 for 3 min for permeabilization. The methanol method consists in employing 95% methanol at -20°C for 3 min. Both of these methods are followed by 3 washing steps and 15 min incubation with PBS. Furthermore, following each staining step, the cells were washed 3 times and incubated for 15 min with blocking buffer [5% horse serum (Sigma) in phosphate buffered saline (PBS)] for actin, e-cadherin, vinculin, and with PBS only for DNA and vimentin. The antibodies were diluted in blocking buffer. Following the staining procedure, the devices were filled with PBS to maintain cell hydration before imaging.

C.3 DATA PROCESSING AND ANALYSIS

For each Ras^{V12} cell, 3-dimensional fluorescence imaging was performed with a Z-step size of 1 µm. Each stack typically contained between 15 and 40 slices, depending the Ras^{V12} cell extrusion level. Automated image analysis programs were developed in Matlab, taking advantage of the image processing toolbox. First, in each image, the X-Y-Z nuclei positions were extracted, the cell contours were determined, and the Ras^{V12} cell bodies were identified. Visual inspection of each of these steps was carried out for every image, and manual corrections were performed when necessary. The majority of the subsequent analysis built upon this extraction. Specifically, the local stacks considered for the basal (-5 to -3 µm), mid-cell (-1 to +1 um), and upper-cell (>1 um) Z-slice projections were determined based on the local nuclei average height ("0-height"). The protrusion areas were determined based on the basal level GFP signal outside of the Ras^{V12} cell bodies. The height difference between the Ras^{V12} cells and the surrounding WT cells was determined from the apical maxima of the Z-profiles of the actin intensity averaged over the cell areas. The junctional regions were identified based on the extracted cell contours, considering 11 pixel (~4 µm) wide regions centered on the cell frontiers. The actin and e-cadherin channels were summed over all Z-slices for determining the average junctional intensity ratios in Fig. 5.2b,g, Fig. C.3b,c, and Fig. C.4a,c,d. The actin channel was summed over the local basal slices for determining the basal actin in Fig. 5.2d,e, Fig. C.3a , and Fig. C.4b . For Fig. 5.3b, the orientation of the protrusion segments and basal actin SFs were both determined manually on different identification sessions. This was achieved by displaying in each case only the element to be characterized in that session (to prevent any bias). To compile the histogram in Fig. 5.4d, only the WT SFs which were outside a protrusion and which approached its major axis within 4 µm or less were considered. The actin channel was summed over the local upper-cell Z-slices in Fig. 5.3c (to exclude basal SFs). The regionprops function of Matlab was used to determine the cell body area in Fig. C.2, based on the cell contour extraction. Finally, for the vinculin and vimentin analysis of Fig. C.5, the Ras^{V12} cell regions were determined based on the GFP channel alone (thus including both the protrusions and the cell bodies). The vinculin channel was summed over the local basal slices while the vimentin was summed over all Z-slices. Additional details are presented in the table C.2 (below).

Description	Example of output image (DMSO control, static state)
Convert the .nd2 stacks into a 4-dimensional Matlab array.	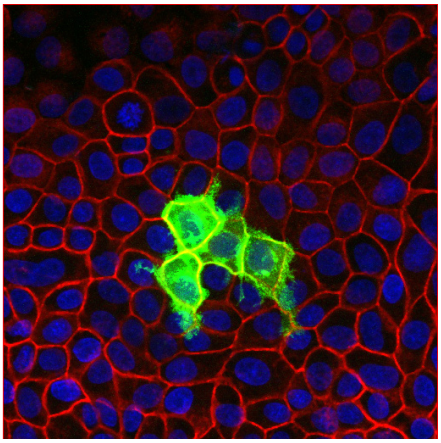 GFP-Ras^{V12} cells in green, junctional actin in red, and nuclei in blue
Extract nuclei positions (X,Y,Z): • Isolate the DAPI channel, extract binary images for each Z-slice, and determine X,Y center of the identified particles; • Go up slice-by-slice to identify and correct nuclei which were erroneously merged together into a single particle; repeat in the other direction; • Regroup nuclei identified from different Z-slices which belong to the same particle; • Determine the average X and Y positions, and find the Z position based on the Z intensity profile of a small region around the corresponding X,Y center; • Inspect image and "manually" remove or add nuclei if necessary;	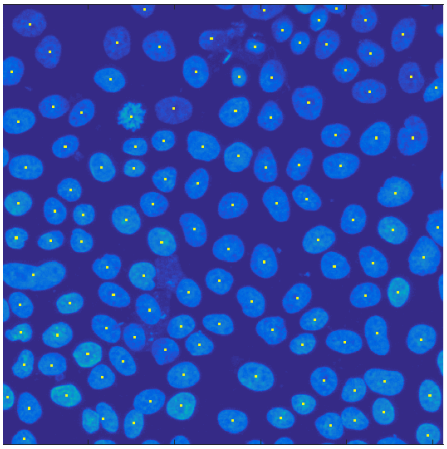 Identified nuclei shown with yellow dots
Extract cell contours: • Isolate the actin channel and extract the projection of three stacks centered on the local average nuclei height to obtain optimal cell divisions based on the junctional actin signal; • Extract binary image and perform watershed to obtain the first iteration of the cell contours; • Scan through each newly identified cell; ○ if a cell contains no nucleus, reattribute its area to neighboring cells based on the actin profile and redefine cell contours;	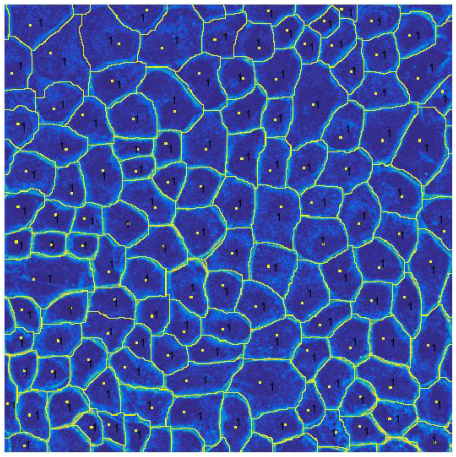 Extracted cell contours shown in yellow (overlaid on the junctional

<table>
<tr>
<td>

if a cell contains more than one nucleus, split it based on the actin profile and redefine cell contours;

Inspect image and “manually” correct cell divisions if necessary;

</td>
<td>actin signal in cyan), identified nuclei shown with yellow dots, 1 means there is 1 nucleus in the identified cell.</td>
</tr>
<tr>
<td>Determine which cell bodies are Ras^{V12} transformed cells:

Isolate the GFP channel and extract the projection of three stacks above the local average nuclei height to obtain the non-basal GFP profile (i.e. excluding the roots);
Extract binary image and determine which cells (identified in the previous step) are significantly covered by the GFP signal; these are the transformed cells;
Inspect image and “manually” correct transformed cells identification if necessary;

</td>
<td> 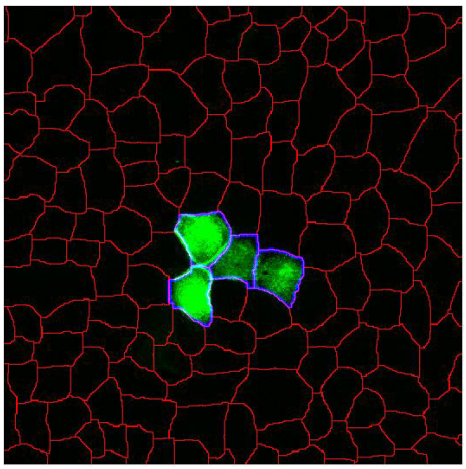
Identified cell contours in red, identified Ras^{V12} cell contours in blue</td>
</tr>
<tr>
<td>Protrusion extraction:

Isolate the GFP channel and extract the projection of the stacks 3-5 µm below the local average nuclei height to obtain the basal GFP profile, which was found to provide the optimal view of the protrusions;
Extract binary image of the basal GFP profile and compare it against the previously identified Ras^{V12} cell contours: the GFP areas falling outside the transformed Ras^{V12} cell body contours are considered to be protrusions;
Associate each protrusion section to the proper transformed cell;

</td>
<td> 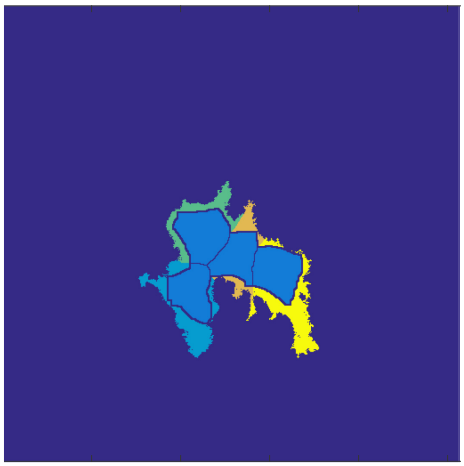
Ras^{V12} cell bodies are in light blue and their protrusions are shown in other colors.</td>
</tr>
</table>

Extraction of other parameters: • Following the identification of the nuclei heights, the cell contours, the Ras^{V12} transformed cell bodies, and the Ras^{V12} protrusions, all the other parameters can be extracted, such as: ○ Height difference between a Ras^{V12} cell and the average surrounding WT cells, based on the apical maxima of the Z-profiles of the actin intensity (averaged in X-Y over the cell areas); ○ Area of the protrusions, normalized to the area of the corresponding Ras^{V12} cell bodies; ○ WT-WT, Ras^{V12}-WT, and Ras^{V12}-Ras^{V12} junctional actin or e-cadherin intensities, using the full Z-projection (see example of junctional region identification on the right); ○ WT and Ras^{V12} basal actin and vinculin intensities, using the projection of the stacks 3 to 5 µm below the local average nuclei heights; ○ WT cell body orientations using Matlab's image processing toolbox to determine the major axis orientation;	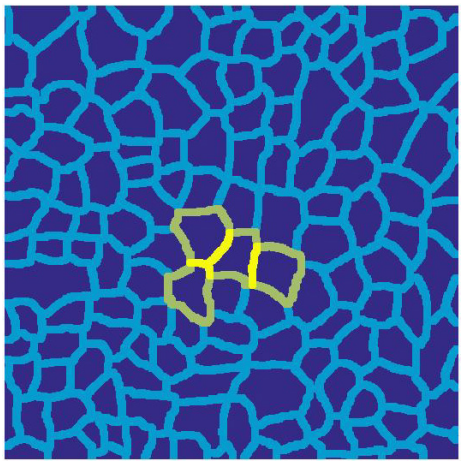 Light blue, green, and yellow regions are WT-WT, WT-Ras^{V12}, and Ras^{V12}-Ras^{V12} junctions, respectively.

Table C.2 Image analysis summary.

REFERENCES

1. Jansen, K. A. *et al.* A guide to mechanobiology: Where biology and physics meet. *Biochim. Biophys. Acta - Mol. Cell Res.* **1853,** 3043–3052 (2015).
2. Humphrey, J. D., Dufresne, E. R. & Schwartz, M. a. Mechanotransduction and extracellular matrix homeostasis. *Nat. Rev. Mol. Cell Biol.* **15,** 802–812 (2014).
3. Ingber, D. E. Cellular mechanotransduction: putting all the pieces together again. *FASEB J.* **20,** 811–827 (2006).
4. Jaalouk, D. E. & Lammerding, J. Mechanotransduction gone awry. *Nat. Rev. Mol. Cell Biol.* **10,** 63–73 (2009).
5. Ingber, D. E. Mechanobiology and diseases of mechanotransduction. *Ann. Med.* **35,** 564–577 (2003).
6. Spyropoulou, A., Karamesinis, K. & Basdra, E. K. Mechanotransduction pathways in bone pathobiology. *Biochim. Biophys. Acta - Mol. Basis Dis.* **1852,** 1700–1708 (2015).
7. Wang, J. H. C. & Thampatty, B. P. An introductory review of cell mechanobiology. *Biomech. Model. Mechanobiol.* **5,** 1–16 (2006).
8. Ohashi, K., Fujiwara, S. & Mizuno, K. Roles of the cytoskeleton, cell adhesion and rho signalling in mechanosensing and mechanotransduction. *J. Biochem.* **161,** 245–254 (2017).
9. Li, Y. S. J., Haga, J. H. & Chien, S. Molecular basis of the effects of shear stress on vascular endothelial cells. *J. Biomech.* **38,** 1949–1971 (2005).
10. Banerjee, I. *et al.* Cyclic stretch of embryonic cardiomyocytes increases proliferation, growth, and expression while repressing Tgf-β signaling. *J. Mol. Cell. Cardiol.* **79,** 133–144 (2015).
11. Huh, D., Matthews, B. D., Mammoto, A., Hsin, H. Y. & Ingber, D. E. Reconstituting Organ-Level Lung Functions on a Chip. *Science (80-.).* **328,** 1662–67 (2010).
12. Kim, E. H., Oh, N., Jun, M., Ko, K. & Park, S. Effect of cyclic stretching on cell shape and division. *BioChip J.* **9,** 306–312 (2015).
13. Vogel, V. & Sheetz, M. Local force and geometry sensing regulate cell functions. *Nat Rev Mol Cell Biol* **7,** 265–275 (2006).
14. Chalfie, M. Neurosensory mechanotransduction. *Nat. Rev. Mol. Cell Biol.* **10,** 44 (2009).
15. Mammoto, T., Mammoto, A. & Ingber, D. E. Mechanobiology and Developmental Control. *Annu. Rev. Cell Dev. Biol.* **29,** 27–61 (2013).
16. Hove, J. R. *et al.* Intracardiac fluid forces are an essential epigenetic factor for embryonic cardiogenesis. *Nature* **421,** 172–177 (2003).
17. Engler, A. J., Sen, S., Sweeney, H. L. & Discher, D. E. Matrix Elasticity Directs Stem Cell Lineage Specification. *Cell* **126,** 677–689 (2006).
18. Viswanathan, P. *et al.* 3D Surface Topology Guides Stem Cell Adhesion and Differentiation. *Biomaterials* **8,** 583–592 (2016).
19. Elsaadany, M. *et al.* Equiaxial Strain Modulates Adipose-derived Stem Cell Differentiation within 3D Biphasic Scaffolds towards Annulus Fibrosus. *Sci. Rep.* **7,** 1–14 (2017).
20. Schrank, T. P., Marcotte, G. R., West, D. W. D. & Baar, K. The Molecular Basis for Load-Induced Skeletal Muscle Hypertrophy. *Calcif Tissue Int.* **17,** 95–121 (2016).
21. Fernandes, T., Baraúna, V. G., Negrão, C. E., Phillips, M. I. & Oliveira, E. M. Aerobic exercise training promotes physiological cardiac remodeling involving a set of microRNAs. *Am. J. Physiol. Heart Circ. Physiol.* **309,** H543-52 (2015).
22. Yamada, A. K., Verlengia, R. & Bueno Junior, C. R. Mechanotransduction pathways in skeletal muscle hypertrophy. *J. Recept. Signal Transduct.* **32,** 42–44 (2012).

23. Williams, B. Mechanical influences on vascular smooth muscle cell function. *J. Hypertens.* **16,** 1921–1929 (1998).
24. Mullender, M. *et al.* Mechanotransduction of bone cells in vitro: Mechanobiology of bone tissue. *Med. Biol. Eng. Comput.* **42,** 14–21 (2004).
25. Hou, H. W. *et al.* Microfluidics for applications in cell mechanics and mechanobiology. *Cell. Mol. Bioeng.* **4,** 591–602 (2011).
26. Chiu, C., Wang, B. & Shyu, K. Effects of cyclic stretch on the molecular regulation of myocardin in rat aortic vascular smooth muscle cells. 1–12 (2013).
27. Spatz, J. M. *et al.* Sclerostin antibody inhibits skeletal deterioration due to reduced mechanical loading. *J. Bone Miner. Res.* **28,** 865–874 (2013).
28. Squires, T. M. & Quake, S. R. Microfluidics: Fluid physics at the nanoliter scale. *Rev. Mod. Phys.* **77,** 977–1026 (2005).
29. Polacheck, W. J., Li, R., Uzel, S. G. M. & Kamm, R. D. Microfluidic platforms for mechanobiology. *Lab Chip* **13,** 2252–67 (2013).
30. Abiko, H. *et al.* Rho guanine nucleotide exchange factors involved in cyclic-stretch-induced reorientation of vascular endothelial cells. *J. Cell Sci.* **128,** 1683–95 (2015).
31. Gawlak, G. *et al.* Paxillin mediates stretch-induced Rho signaling and endothelial permeability via assembly of paxillin-p42/44MAPK-GEF-H1 complex. *FASEB J* **28,** (2014).
32. Peng, F. *et al.* Mechanical stretch-induced RhoA activation is mediated by the RhoGEF Vav2 in mesangial cells. *Cell Signal.* **22,** 34–40 (2010).
33. Lessey, E. C., Guilluy, C. & Burridge, K. From mechanical force to RhoA activation. *Biochemistry* **51,** 7420–7432 (2012).
34. Jungbauer, S., Gao, H., Spatz, J. P. & Kemkemer, R. Two characteristic regimes in frequency-dependent dynamic reorientation of fibroblasts on cyclically stretched substrates. *Biophys. J.* **95,** 3470–3478 (2008).
35. Wang, H., Ip, W., Boissy, R. & Grood, E. S. Cell orientation response to cyclically deformed substrates: Experimental validation of a cell model. *J. Biomech.* **28,** 1543–1552 (1995).
36. Neidlinger-Wilke, C., Grood, E. S., Wang, J. H. C., Brand, R. A. & Claes, L. Cell alignment is induced by cyclic changes in cell length: Studies of cells grown in cyclically stretched substrates. *J. Orthop. Res.* **19,** 286–293 (2001).
37. Naruse, K., Yamada, T. & Sokabe, M. Involvement of SA channels in orienting response of cultured endothelial cells to cyclic stretch. *Am. J. Physiol.* **274,** H1532–H1538 (1998).
38. Moretti, M., Prina-Mello, A., Reid, A. J., Barron, V. & Prendergast, P. J. Endothelial cell alignment on cyclically-stretched silicone surfaces. *J. Mater. Sci. Mater. Med.* **15,** 1159–1164 (2004).
39. Kang, J. *et al.* Response of an actin filament network model under cyclic stretching through a coarse grained Monte Carlo approach. *J. Theor. Biol.* **274,** 109–119 (2011).
40. Buck, R. C. Reorientation response of cells to repeated stretch and recoil of the substratum. *Exp. Cell Res.* **127,** 470–474 (1980).
41. Morita, Y., Watanabe, S., Ju, Y. & Yamamoto, S. In Vitro Experimental Study for the Determination of Cellular Axial Strain Threshold and Preferential Axial Strain from Cell Orientation Behavior in a Non-uniform Deformation Field. *Cell Biochem. Biophys.* **67,** 1249–1259 (2013).
42. Lu, J. *et al.* Cell orientation gradients on an inverse opal substrate. *ACS Appl. Mater. Interfaces* **7,** 10091–10095 (2015).
43. Wang, L. *et al.* Patterning Cellular Alignment through Stretching Hydrogels with Programmable Strain Gradients. *ACS Appl. Mater. Interfaces* **7,** 15088–15097 (2015).
44. Tremblay, D., Chagnon-Lessard, S., Mirzaei, M., Pelling, A. E. & Godin, M. A microscale

anisotropic biaxial cell stretching device for applications in mechanobiology. *Biotechnol. Lett.* **36,** 657–665 (2014).
45. Chagnon-Lessard, S., Jean-Ruel, H., Godin, M. & Pelling, A. E. Cellular orientation is guided by strain gradients. *Integr. Biol.* **9,** 607–618 (2017).
46. Gudipaty, S. A. & Rosenblatt, J. Epithelial cell extrusion: Pathways and pathologies. *Semin. Cell Dev. Biol.* **67,** 132–140 (2017).
47. Hogan, C. *et al.* Characterization of the interface between normal and transformed epithelial cells. *Nat. Cell Biol.* **11,** 460–467 (2009).
48. Swaminathan, V. & Waterman, C. M. The molecular clutch model for mechanotransduction evolves. *Nat. Cell Biol.* **18,** 459–61 (2016).
49. Elosegui-Artola, A. *et al.* Mechanical regulation of a molecular clutch defines force transmission and transduction in response to matrix rigidity. *Nat. Cell Biol.* **18,** 540–548 (2016).
50. Reinhart-King, C. A., Dembo, M. & Hammer, D. A. Cell-cell mechanical communication through compliant substrates. *Biophys. J.* **95,** 6044–6051 (2008).
51. Adamo, L. *et al.* Biomechanical forces promote embryonic haematopoiesis. *Nature* **459,** 1131–5 (2009).
52. Marenzana, M., Wilson-Jones, N., Mudera, V. & Brown, R. A. The origins and regulation of tissue tension: Identification of collagen tension-fixation process in vitro. *Exp. Cell Res.* **312,** 423–433 (2006).
53. Cyron, C. J., Aydin, R. C. & Humphrey, J. D. A homogenized constrained mixture (and mechanical analog) model for growth and remodeling of soft tissue. *Biomech. Model. Mechanobiol.* **15,** 1389–1403 (2016).
54. Delvoye, P., Wiliquet, P., Levêque, J.-L., Nusgens, B. V. & Lapière, C. M. Measurement of Mechanical Forces Generated by Skin Fibroblasts Embedded in a Three-Dimensional Collagen Gel. *Journal of Investigative Dermatology* **97,** 898–902 (1991).
55. Wen, Q. & Janmey, P. A. Effects of non-linearity on cell-ECM interactions. *Exp. Cell Res.* **319,** 2481–2489 (2013).
56. Wang, N., Tytell, J. D. & Ingber, D. E. Mechanotransduction at a distance: mechanically coupling the extracellular matrix with the nucleus. *Nat. Rev. Mol. Cell Biol.* **10,** 75–82 (2009).
57. Ingber, D. E. Cellular mechanotransduction: putting all the pieces together again. *FASEB J.* **20,** 27 (2006).
58. Burridge, K. & Guilluy, C. Focal adhesions , stress fi bers and mechanical tension. *Exp. Cell Res.* **343,** 14–20 (2016).
59. Geiger, B., Spatz, J. P. & Bershadsky, A. D. Environmental sensing through focal adhesions. *Nat. Rev. Mol. Cell Biol.* **10,** 21–33 (2009).
60. Wang, N., Butler, J. & Ingber, D. Mechanotransduction across the cell surface and through the cytoskeleton. *Science (80-.).* **260,** 1124–1127 (1993).
61. Vincent, J. P., Fletcher, A. G. & Baena-Lopez, L. A. Mechanisms and mechanics of cell competition in epithelia. *Nat. Rev. Mol. Cell Biol.* **14,** 581–591 (2013).
62. Fletcher, D. A. & Mullins, R. D. Cell mechanics and the cytoskeleton. *Nature* **463,** 485–492 (2010).
63. Discher, D. E., Janmey, P. & Wang, Y.-L. Tissue cells feel and respond to the stiffness of their substrate. *Science* **310,** 1139–43 (2005).
64. Provenzano, P. P. & Keely, P. J. Mechanical signaling through the cytoskeleton regulates cell proliferation by coordinated focal adhesion and Rho GTPase signaling. *J. Cell Sci.* **124,** 1195–1205 (2011).

65. Paszek, M. J. *et al.* Tensional homeostasis and the malignant phenotype. *Cancer Cell* **8,** 241–254 (2005).
66. Saez, A., Buguin, A., Silberzan, P. & Ladoux, B. Is the mechanical activity of epithelial cells controlled by deformations or forces? *Biophys. J.* **89,** L52–L54 (2005).
67. Colin-Yorka, H. & Fritzsche, M. The future of traction force microscopy. *ScienceDirect* **5,** 1–5 (2018).
68. Wang, J. H. Substrate deformation determines actin cytoskeleton reorganization: A mathematical modeling and experimental study. *J. Theor. Biol.* **202,** 33–41 (2000).
69. Snider, N. T. & Omary, M. B. Post-translational modifications of intermediate filament proteins: mechanisms and functions. *Nat Rev Mol Cell Biol* **15,** 163–177 (2014).
70. Weber, G. F., Bjerke, M. A. & DeSimone, D. W. A Mechanoresponsive Cadherin-Keratin Complex Directs Polarized Protrusive Behavior and Collective Cell Migration. *Dev. Cell.* **22,** 104–115 (2012).
71. Leccia, E. *et al.* Cyclic stretch reveals a mechanical role for intermediate filaments in a desminopathic cell model. *Phys. Biol.* **10,**
72. Goldman, R. D. *et al.* Intermediate filament networks: organization and possible functions of a diverse group of cytoskeletal elements. *J. Cell Sci.* **5,** 69–97 (1986).
73. Etienne-Manneville, S. Microtubules in Cell Migration. *Annu. Rev. Cell Dev. Biol.* **29,** 471–499 (2013).
74. Hawkins, T., Mirigian, M., Selcuk Yasar, M. & Ross, J. L. Mechanics of microtubules. *J. Biomech.* **43,** 23–30 (2010).
75. Goode, B. L., Drubin, D. G. & Barnes, G. Functional cooperation between the microtubule and actin cytoskeletons. *Curr. Opin. Cell Biol.* **12,** 63–71 (2000).
76. Morioka, M. *et al.* Microtubule dynamics regulate cyclic stretch-induced cell alignment in human airway smooth muscle cells. *PLoS One* **6,** 1–9 (2011).
77. Hall, A. SMALL GTP-BINDING PROTEINS AND THE REGULATION OF THE ACTIN CYTOSKELETON. *Annu. Rev. Cell Biol.* **10,** 31–54 (1994).
78. Goode, B. L. & Eck, M. J. Mechanism and function of formins in the control of actin assembly. *Annu. Rev. Biochem.* **76,** 593–627 (2007).
79. Tseng, Y. *et al.* How actin crosslinking and bundling proteins cooperate to generate an enhanced cell mechanical response. *Biochem. Biophys. Res. Commun.* **334,** 183–192 (2005).
80. Stricker, J., Falzone, T. & Gardel, M. L. Mechanics of the F-actin Cytoskeleton. *J Biomech.* **43,** 9–14 (20010).
81. Pollard, T. D. & Borisy, G. G. Cellular motility driven by assembly and disassembly of actin filaments. *Cell* **112,** 453–465 (2003).
82. Murrell, M., Oakes, P. W., Lenz, M. & Gardel, M. L. Forcing cells into shape: The mechanics of actomyosin contractility. *Nat. Rev. Mol. Cell Biol.* **16,** 486–498 (2015).
83. Yoshigi, M., Hoffman, L. M., Jensen, C. C., Yost, H. J. & Beckerle, M. C. Mechanical force mobilizes zyxin from focal adhesions to actin filaments and regulates cytoskeletal reinforcement. *J. Cell Biol.* **171,** 209–215 (2005).
84. *Rho Gtpases: Molecular Biology In Health And Disease*. (World Scientific Publishing Company, 2017).
85. Volkers, L., Mechioukhi, Y. & Coste, B. Piezo channels: from structure to function. *Pflugers Arch.* **467,** 95–99 (2015).
86. C, G. & K, B. Nuclear mechanotransduction: forcing the nucleus to respond. *Nucleus* **6,** 19–22 (2015).
87. Kuo, J.-C., Han, X., Hsiao, C.-T., Yates, J. R. & M.Waterman, C. Analysis of the myosinII-

responsive focal adhesion proteome reveals a role for β-Pix in negative regulation of focal adhesion maturation. *Nat Cell Biol* **13,** 383–393 (2011).
88. Aelst, L. Van & D'Souza-Schorey, C. Rho GTPases and signaling networks. *Genes Dev.* **11,** 2295–2322 (1997).
89. Fukata, M. & Kaibuchi, K. Rho-family GTPases in cadherin-mediated cell — cell adhesion. *Nat. Rev. Mol. Cell Biol.* **2,** 887–897 (2001).
90. Sahai, E. & Marshall, C. J. ROCK and Dia have opposing effects on adherens junctions downstream of Rho. *Nat. Cell Biol.* **4,** (2003).
91. Burridge, K. & Wittchen, E. S. The tension mounts: Stress fibers as force-generating mechanotransducers. *J. Cell Biol.* **200,** 9–19 (2013).
92. Guilluy, C. *et al.* The Rho GEFs LARG and GEF-H1 regulate the mechanical response to force on integrins. *Nat Cell Biol* **13,** 722–727 (2011).
93. Marchiando, A. M., Graham, W. V. & Turner, J. R. Epithelial Barriers in Homeostasis and Disease. *Annu. Rev. Pathol. Mech. Dis.* **5,** 119–144 (2010).
94. Rosenblatt, J., Raff, M. C. & Cramer, L. P. An epithelial cell destined for apoptosis signals its neighbors to extrude it by an actin- and myosin-dependent mechanism. *Curr. Biol.* **11,** 1847–1857 (2001).
95. Gu, Y., Forostyan, T., Sabbadini, R. & Rosenblatt, J. Epithelial cell extrusion requires the sphingosine-1-phosphate receptor 2 pathway. *J. Cell Biol.* **193,** 667–676 (2011).
96. Slattum, G., McGee, K. M. & Rosenblatt, J. P115 RhoGEF and microtubules decide the direction apoptotic cells extrude from an epithelium. *J. Cell Biol.* **186,** 693–702 (2009).
97. Kuipers, D. *et al.* Epithelial repair is a two-stage process driven first by dying cells and then by their neighbours. *J. Cell Sci.* **127,** 1229–1241 (2014).
98. Wu, S. K. & Yap, A. S. Patterns in space: Coordinating adhesion and actomyosin contractility at E-cadherin junctions. *Cell Commun. Adhes.* **20,** 201–212 (2013).
99. Borghi, N. *et al.* E-cadherin is under constitutive actomyosin-generated tension that is increased at cell-cell contacts upon externally applied stretch. *Proc. Natl. Acad. Sci.* **109,** 12568–12573 (2012).
100. Wu, S. K., Lagendijk, A. K., Hogan, B. M., Gomez, G. A. & Yalp, A. S. Active contractility at E-cadherin junctions and its implications for cell extrusion in cancer. *Cell Cycle* **14,** 315–322 (2015).
101. Michael, M. *et al.* Cortical F-actin stabilization generates apical- lateral patterns of junctional contractility that integrate cells into ... Cortical F-actin stabilization generates apical – lateral patterns of junctional contractility that integrate cells into epithelia. *Nat. Cell Biol.* **16,** 1–15 (2014).
102. Vadlamudi, R., Adam, L., Talukder, a, Mendelsohn, J. & Kumar, R. Serine phosphorylation of paxillin by heregulin-beta1: role of p38 mitogen activated protein kinase. *Oncogene* **18,** 7253–64 (1999).
103. Hanahan, D. & Weinberg, R. A. Hallmarks of cancer: The next generation. *Cell* **144,** 646–674 (2011).
104. Kumar, S. & Weaver, V. M. Mechanics, malignancy, and metastasis: The force journey of a tumor cell. *Cancer Metastasis Rev.* **28,** 113–127 (2009).
105. Alibert, C., Goud, B. & Manneville, J. B. Are cancer cells really softer than normal cells? *Biol. Cell* **109,** 167–189 (2017).
106. Suresh, S. Biomechanics and biophysics of cancer cells. *Acta Biomater* **3,** 413–438 (2007).
107. Cross, S. E., Jin, Y. S., Rao, J. & Gimzewski, J. K. Nanomechanical analysis of cells from cancer patients. *Nat. Nanotechnol.* **2,** 780–783 (2007).
108. Shao, Z.-M., Nguyen, M. & Barsky, S. H. Human breast carcinoma desmoplasia is PDGF

initiated. *Oncogene* **19,** 4337–4345 (2000).
109. Tse, J. M. *et al.* Mechanical compression drives cancer cells toward invasive phenotype. *Proc. Natl. Acad. Sci.* **109,** 911–916 (2012).
110. Hofmann, M. *et al.* Lowering of Tumor Interstitial Fluid Pressure Reduces Tumor Cell Proliferation in a Xenograft Tumor Model. *Neoplasia* **8,** 89–95 (2006).
111. Bos, J. L. ras Oncogenes in Human Cancer : A Review ras Oncogenes in Human Cancer : A Review1. 4682–4689 (1989).
112. Kajita, M. *et al.* Filamin acts as a key regulator in epithelial defence against transformed cells. *Nat. Commun.* **5,** 1–13 (2014).
113. Xia, M. & Land, H. Tumor suppressor p53 restricts Ras stimulation of RhoA and cancer cell motility. *Nat. Struct. Mol. Biol.* **14,** 215–223 (2007).
114. Zondag, G. C. M. *et al.* Oncogenic Ras downregulates Rac activity, which leads to increased Rho activity and epithelial-mesenchymal transition. *J. Cell Biol.* **149,** 775–781 (2000).
115. Slattum, G. M. & Rosenblatt, J. Tumour cell invasion: an emerging role for basal epithelial cell extrusion. *Nat Rev Cancer* **14,** 495–501 (2014).
116. Shemesh, J. *et al.* Flow-induced stress on adherent cells in microfluidic devices. *Lab Chip* **15,** 4114–4127 (2015).
117. Kirby, B. *Micro- and Nanoscale Fluid Mechanics*. *Chemistry & …* (2010). doi:10.1017/CBO9780511760723
118. Faust, U. *et al.* Cyclic stress at mHz frequencies aligns fibroblasts in direction of zero strain. *PLoS One* **6,** e28963(1-16) (2011).
119. Booth, R., Noh, S. & Kim, H. A multiple-channel, multiple-assay platform for characterization of full-range shear stress effects on vascular endothelial cells. *Lab Chip* **14,** 1880–1890 (2014).
120. *Cells, Forces, and the microenvironment*. (Pan Stanford, 2015).
121. Gao, X. *et al.* Regulation of cell migration and osteogenic differentiation in mesenchymal stem cells under extremely low fluidic shear stress. *Biomicrofluidics* **8,** 52008 (2014).
122. Tzima, E., Pozo, M. A. del, Shattil, S. J., Chien, S. & Schwartz, M. A. Activation of integrins in endothelial cells by fluid shear stress mediates Rho-dependent cytoskeletal alignment. *EMBO J.* **20,** 4639–47 (2001).
123. Steward, R., Tambe, D., Hardin, C. C., Krishnan, R. & Fredberg, J. J. Fluid shear, intercellular stress, and endothelial cell alignment. *Am. J. Physiol. - Cell Physiol.* **308,** C657–C664 (2015).
124. Chun, M. S. & Lee, S. Flow imaging of dilute colloidal suspension in PDMS-based microfluidic chip using fluorescence microscopy. *Colloids Surfaces A Physicochem. Eng. Asp.* **267,** 86–94 (2005).
125. Vanapalli, S. A., Duits, M. H. G. & Mugele, F. Microfluidics as a functional tool for cell mechanics. *Biomicrofluidics* **3,** 12006 (2009).
126. Sia, S. K. & Whitesides, G. M. Microfluidic devices fabricated in poly(dimethylsiloxane) for biological studies. *Electrophoresis* **24,** 3563–3576 (2003).
127. Regehr, K. J. *et al.* Biological implications of polydimethylsiloxane-based microfluidic cell culture. *Lab Chip* **9,** 2132–2139 (2009).
128. Hadjiantoniou, S. V. *et al.* Physical confinement signals regulate the organization of stem cells in three dimensions. *J. R. Soc. Interface* **13,** 20160613 (2016).
129. Cox, T. R. & Erler, J. T. Remodeling and homeostasis of the extracellular matrix: implications for fibrotic diseases and cancer. *Dis. Model. Mech.* **4,** 165–178 (2011).
130. Bissell, M. J. & Radisky, D. Putting tumours in context. *Nat Rev Cancer* **1,** 46–54 (2010).
131. Chen, K. *et al.* Role of boundary conditions in determining cell alignment in response to stretch. *Proc. Natl. Acad. Sci.* **115,** 986–991 (2018).

132. Sung, K. E. *et al.* Understanding the Impact of 2D and 3D Fibroblast Cultures on In Vitro Breast Cancer Models. *PLoS One* **8,** 1–13 (2013).
133. Hu, Z., Metaxas, D. & Axel, L. In vivo strain and stress estimation of the heart left and right ventricles from MRI images. *Med. Image Anal.* **7,** 435–444 (2003).
134. Al Nazer, R., Lanovaz, J., Kawalilak, C., Johnston, J. D. & Kontulainen, S. Direct in vivo strain measurements in human bone-A systematic literature review. *J. Biomech.* **45,** 27–40 (2012).
135. Rubin, J. M. *et al.* Ultrasound Strain Measurements for Evaluating Local Pulmonary Ventilation. *Ultrasound Med. Biol.* **42,** 2525–2531 (2016).
136. Wang, J. H. C., Yang, G., Li, Z. & Shen, W. Fibroblast responses to cyclic mechanical stretching depend on cell orientation to the stretching direction. *J. Biomech.* **37,** 573–576 (2004).
137. Ueda, S., Blee, A. M., Macway, K. G., Renner, D. J. & Yamada, S. Force dependent biotinylation of myosin IIA by α-catenin tagged with a promiscuous biotin ligase. *PLoS One* **10,** 1–15 (2015).
138. Reddy, J. N. *An introduction to continuum mechanics*. (Cambridge University Press, 2007).
139. Richardson, W. J., Metz, R. P., Moreno, M. R., Wilson, E. & Moore, J. E. A Device to Study the Effects of Stretch Gradients on Cell Behavior. *J. Biomech. Eng.* **133,** 101008(1-9) (2011).
140. Li, F., Chan, C. U. & Ohl, C. D. Yield strength of human erythrocyte membranes to impulsive stretching. *Biophys. J.* **105,** 872–879 (2013).
141. Tschumperlin, D. J., Oswari, J., Margulies, a S. & Margulies, S. S. Deformation-induced injury of alveolar epithelial cells - Effect of frequency, duration, and amplitude. *Am. J. Respir. Crit. Care Med.* **162,** 357 (2000).
142. Livne, A., Bouchbinder, E. & Geiger, B. Cell reorientation under cyclic stretching. *Nat. Commun.* **5,** 3938 (2014).
143. Murphy, D. B. *Fundamentals of light microscopy and electronic imaging*. (John Wiley & Sons, 2002).
144. Popescu, G. *Quantitative Phase Imaging of Cells and Tissues*. (McGraw-Hill Education, 2011).
145. Schnell, U., Dijk, F., Sjollema, K. a & Giepmans, B. N. G. Immunolabeling artifacts and the need for live-cell imaging. *Nat. Methods* **9,** 152–158 (2012).
146. Webb, R. H. Confocal optical microscopy. *Reports Prog. Phys.* **59,** 427–471 (1996).
147. Cole, R. W., Jinadasa, T. & Brown, C. M. Measuring and interpreting point spread functions to determine confocal microscope resolution and ensure quality control. *Nat. Protoc.* **6,** 1929–1941 (2011).
148. Miller, D. C., Kempe, M. D., Kennedy, C. E. & Kurtz, S. R. Analysis of transmitted optical spectrum enabling accelerated testing of multijunction concentrating photovoltaic designs. **50,** 1–17 (2011).
149. Behrndt, M. *et al.* Forces Driving Epithelial Spreading in Zebrafish Gastrulation. *Science (80-.).* **338,** 257–260 (2012).
150. Howard, J. *Mechanics of Motor Proteins and the Cytoskeleton*. (Sinauer Associates, 2001). doi:10.1017/CBO9781107415324.004
151. Guck, J. *et al.* The optical stretcher: A novel laser tool to micromanipulate cells. *Biophys. J.* **81,** 767–784 (2001).
152. Guck, J., Ananthakrishnan, R., Moon, T., Cunningham, C. & Käs, J. Optical deformability of soft biological dielectrics. *Phys Rev Lett.* **84,** 5451–4 (2000).
153. Kamble, H., Barton, M. J., Jun, M., Park, S. & Nguyen, N.-T. Cell stretching devices as research tools: engineering and biological considerations. *Lab Chip* **16,** 3193–3203 (2016).

154. Kamotani, Y. *et al.* Individually Programmable Cell Stretching Microwell Arrays Actuated by a Braille Display. *Biomaterials* **29,** 2646–2655 (2008).
155. Neidlinger-Wilke, C., Wilke, H.-J. & Claes, L. Cyclical stretching of human osteoblasts affects proliferation and metabolism: a new experimental method and its application. *J.Orthop.Res.* **12,** 70–78 (1994).
156. Wang, Z., Samanipour, R., Koo, K.-I. & Kim, K. Organ-on-a-Chip Platforms for Drug Delivery and Cell Characterization: A Review. *Sensors Mater.* **27,** 487–506 (2015).
157. Kim, H. J., Huh, D., Hamilton, G. & Ingber, D. E. Human gut-on-a-chip inhabited by microbial flora that experiences intestinal peristalsis-like motions and flow. *Lab Chip* **12,** 2165–74 (2012).
158. Huang, Y. & Nguyen, N. T. A polymeric cell stretching device for real-time imaging with optical microscopy. *Biomed. Microdevices* **15,** 1043–1054 (2013).
159. Johnston, I. D., McCluskey, D. K., Tan, C. K. L. & Tracey, M. C. Mechanical characterization of bulk Sylgard 184 for microfluidics and microengineering. *J. Micromechanics Microengineering* **24,** (2014).
160. Sami Franssila. Introduction to Microfabrication, Second Edition - Franssila - Wiley Online Library. 1–518 (2010). doi:10.1002/9781119990413
161. Microchem. SU-8 2000 Permanent Epoxy Negative Photoresist. *Process. Guidel.* (2015). doi:10.1146/annurev.matsci.28.1.153
162. Mack, C. A. *Field guide to optical lithography*. (2006).
163. Pelleg, J. *Mechanical Properties of Materials*. *Springer* **190,** (2013).
164. H. Pritchard, R., Lava, P., Debruyne, D. & M. Terentjev, E. Precise determination of the Poisson ratio in soft materials with 2D digital image correlation. *Soft Matter* **9,** 6037 (2013).
165. Damon, B. J. *et al.* Patterns of muscular strain in the embryonic heart wall. *Dev. Dyn.* **238,** 1535–1546 (2009).
166. Heisenberg, C. P. & Bellaïche, Y. Forces in tissue morphogenesis and patterning. *Cell* **153,** 958–962 (2013).
167. Beck, B. R., Qin, Y. X., McLeod, K. J. & Otter, M. W. On the relationship between streaming potential and strain in an In vivo bone preparation. *Calcif. Tissue Int.* **71,** 335–343 (2002).
168. De, R., Zemel, A. & Safran, S. a. Dynamics of cell orientation. *Nat. Phys.* **3,** 655–659 (2007).
169. Safran, S. A. & De, R. Nonlinear dynamics of cell orientation. *Phys. Rev. E - Stat. Nonlinear, Soft Matter Phys.* **80,** 4–7 (2009).
170. Stamenović, D., Lazopoulos, K. A., Pirentis, A. & Suki, B. Mechanical stability determines stress fiber and focal adhesion orientation. *Cell. Mol. Bioeng.* **2,** 475–485 (2009).
171. Chen, B., Kemkemer, R., Deibler, M., Spatz, J. & Gao, H. Cyclic Stretch Induces Cell Reorientation on Substrates by Destabilizing Catch Bonds in Focal Adhesions. *PLoS One* **7,** e48346(1-11) (2012).
172. Wang, J. H. C., Goldschmidt-Clermont, P. & Yin, F. C. P. Contractility affects stress fiber remodeling and reorientation of endothelial cells subjected to cyclic mechanical stretching. *Ann. Biomed. Eng.* **28,** 1165–1171 (2000).
173. Goldyn, A. M., Kaiser, P., Spatz, J. P., Ballestrem, C. & Kemkemer, R. The kinetics of force-induced cell reorganization depend on microtubules and actin. *Cytoskeleton* **67,** 241–250 (2010).
174. Zhao, L., Sang, C., Yang, C. & Zhuang, F. Effects of stress fiber contractility on uniaxial stretch guiding mitosis orientation and stress fiber alignment. *J. Biomech.* **44,** 2388–2394 (2011).
175. Chen, B., Ji, B. & Gao, H. Modeling Active Mechanosensing in Cell-Matrix Interactions. *Annu. Rev. Biophys.* **44,** 1–32 (2015).

176. Wolfenson, H., Bershadsky, A., Henis, Y. I. & Geiger, B. Actomyosin-generated tension controls the molecular kinetics of focal adhesions. *J. Cell Sci.* **124,** 1425–1432 (2011).
177. Greiner, A. M., Chen, H., Spatz, J. P. & Kemkemer, R. Cyclic Tensile Strain Controls Cell Shape and Directs Actin Stress Fiber Formation and Focal Adhesion Alignment in Spreading Cells. *PLoS One* **8,** e77328(1-9) (2013).
178. Raz-Ben Aroush, D., Barlam, D. & Daniel Wagner, H. Generating an inhomogeneous stress field as a technique to study cell mechanoresponse. *Appl. Phys. Lett.* **100,** 133703(1-4) (2012).
179. Balestrini, J. L., Skorinko, J. K., Hera, A., Gaudette, G. R. & Billiar, K. L. Applying controlled non-uniform deformation for in vitro studies of cell mechanobiology. *Biomech. Model. Mechanobiol.* **9,** 329–344 (2010).
180. Ohashi, T., Masuda, M., Matsumoto, T. & Sato, M. Nonuniform strain of substrate induces local development of stress fibers in endothelial cells under uniaxial cyclic stretching. *Clin. Hemorheol. Microcirc.* **37,** 37–46 (2007).
181. Richardson, W. J., Wilson, E. & Moore, J. E. Altered phenotypic gene expression of 10T1/2 mesenchymal cells in nonuniformly stretched PEGDA hydrogels. *Am. J. Physiol. Cell Physiol.* **305,** C100-10 (2013).
182. Yung, Y. C., Vandenburgh, H. & Mooney, D. J. Cellular strain assessment tool (CSAT): Precision-controlled cyclic uniaxial tensile loading. *J. Biomech.* **42,** 178–182 (2009).
183. Morita, Y., Sato, T., Watanabe, S. & Ju, Y. Determination of Precise Optimal Cyclic Strain for Tenogenic Differentiation of Mesenchymal Stem Cells Using a Non-uniform Deformation Field. *Exp. Mech.* **55,** 635–640 (2015).
184. Nash, M. P. & Hunter, P. J. Computational mechanics of the heart. From tissue structure to ventricular function. *J. Elast.* **61,** 113–141 (2000).
185. Perchiazzi, G. *et al.* Lung regional stress and strain as a function of posture and ventilatory mode. *J. Appl. Physiol.* **110,** 1374–1383 (2011).
186. Carter, S. Principles of cell motility: the direction of cell movement and cancer invasion. *Nature* **208,** 1183 (1965).
187. Lo, C. M., Wang, H. B., Dembo, M. & Wang, Y. L. Cell movement is guided by the rigidity of the substrate. *Biophys. J.* **79,** 144–152 (2000).
188. Henson, J. H. *et al.* Actin-Based Centripetal Flow: Phosphatase Inhibition by Calyculin-A Alters Flow Pattern, Actin Organization, and Actomyosin Distribution. *Cell Motil. Cytoskeleton* **56,** 252–266 (2003).
189. Mitrossilis, D. *et al.* Single-cell response to stiffness exhibits muscle-like behavior. *Proc. Natl. Acad. Sci. U. S. A.* **106,** 18243–8 (2009).
190. Kaunas, R., Hsu, H. J. & Deguchi, S. Sarcomeric model of stretch-induced stress fiber reorganization. *Cell Health Cytoskelet.* **3,** 13–22 (2011).
191. Wang, J. H. C., Goldschmidt-Clermont, P., Wille, J. & Yin, F. C. P. Specificity of endothelial cell reorientation in response to cyclic mechanical stretching. *J. Biomech.* **34,** 1563–1572 (2001).
192. Pirentis, A. P. & Lazopoulos, K. A. On stress fibre reorientation under plane substrate stretching. *Arch. Appl. Mech.* **79,** 263–277 (2009).
193. Goldyn, A. M., Rioja, B. A., Spatz, J. P., Ballestrem, C. & Kemkemer, R. Force-induced cell polarisation is linked to RhoA-driven microtubule-independent focal-adhesion sliding. *J. Cell Sci.* **122,** 3644–51 (2009).
194. Iba, T. & Sumpio, B. E. Morphological response of human endothelial cells subjected to cyclic strain in vitro. *Microvasc. Res.* **42,** 245–254 (1991).
195. Shemesh, T., Geiger, B., Bershadsky, A. D. & Kozlov, M. M. Focal adhesions as

mechanosensors: a physical mechanism. *Proc. Natl. Acad. Sci. U. S. A.* **102,** 12383–12388 (2005).
196. Na, S. *et al.* Time-dependent changes in smooth muscle cell stiffness and focal adhesion area in response to cyclic equibiaxial stretch. *Ann. Biomed. Eng.* **36,** 369–380 (2008).
197. Huang, W., Sakamoto, N., Hanamura, K., Miyazawa, R. & Sato, M. Role of intercellular junctions in redistribution of focal adhesions and orientation of vascular endothelial cells exposed to cyclic stretching. *Cell. Mol. Bioeng.* **4,** 368–378 (2011).
198. Suzuki, M. *et al.* Up-regulation of integrin beta 3 expression by cyclic stretch in human umbilical endothelial cells. *Biochem. Biophys Commun* **239,** 372–6 (1997).
199. Peterson, L. J. *et al.* Simultaneous Stretching and Contraction of Stress Fibers In Vivo. *Mol. Biol. Cell* **15,** 3497–3508 (2004).
200. Pasapera, A. M., Schneider, I. C., Rericha, E., Schlaepfer, D. D. & Waterman, C. M. Myosin II activity regulates vinculin recruitment to focal adhesions through FAK-mediated paxillin phosphorylation. *J. Cell Biol.* **188,** 877–890 (2010).
201. Del Rio, A. *et al.* Stretching Single Talin Rod. *Science (80-.).* **323,** 638–641 (2009).
202. Case, L. B. & Waterman, C. M. Integration of actin dynamics and cell adhesion by a three-dimensional, mechanosensitive molecular clutch. *Nat. Cell Biol.* **17,** 955–963 (2015).
203. Schiller, H. B. *et al.* beta1- and alphav-class integrins cooperate to regulate myosin II during rigidity sensing of fibronectin-based microenvironments. *Nat. Cell Biol.* **15,** 625–636 (2013).
204. Sv, P., Am, P., Sabass, B. & Cm, W. Force Fluctuations within Focal Adhesions Mediate ECM-Rigidity Sensing to Guide Directed Cell Migration . **151,** 13–14 (2012).
205. Tse, J. R. & Engler, A. J. Stiffness gradients mimicking in vivo tissue variation regulate mesenchymal stem cell fate. *PLoS One* **6,** (2011).
206. Park, J. Y. *et al.* Increased poly(dimethylsiloxane) stiffness improves viability and morphology of mouse fibroblast cells. *Biochip J.* **4,** 230–236 (2010).
207. Eddington, D. T., Crone, W. C. & Beebe, D. J. Development of process protocols to fine tune polydimethylsiloxane material properties. *7th lnternational Conf. Miniaturized Chem. Blochemlcal Anal. Syst.* **7,** 1089–92 (2003).
208. Williams, T. M., Bengtson, P., Steller, D. L., Croll, D. A. & Davis, R. W. The healthy heart: Lessons from nature's elite athletes. *Physiology* **30,** 349–357 (2015).
209. Proctor, D. N., Beck, K. C. & David, N. Delay time adjustments to minimize errors ˙ O 2 during exercise in breath-by-breath measurement of V. *Chest* (1996). doi:10.1152/japplphysiol.00024.2003
210. Pachi, A. & Ji, T. Frequency and velocity of people walking. *Struct. Eng.* **83,** 36–40 (2005).
211. Fink, J. *et al.* External forces control mitotic spindle positioning. *Nat. Cell Biol.* **13,** 771–8 (2011).
212. Ueki, Y., Sakamoto, N. & Sato, M. Cyclic Force Applied to FAs Induces Actin Recruitment Depending on the Dynamic Loading Pattern. *Open Biomed. Eng. J.* **4,** 129–34 (2010).
213. Hirano, K. *et al.* Changes in the cytoskeleton of 3T3 fibroblasts induced by the phosphatase inhibitor, calyculin-A. *J. Muscle Res. Cell Motil.* **13,** 341–353 (1992).
214. Chartier, L. *et al.* Calyculin-A increases the level of protein phosphorylation and changes the shape of 3T3 fibroblasts. *Cell Motil. Cytoskeleton* **18,** 26–40 (1991).
215. Chen, Y., Pasapera, A. M., Koretsky, A. P. & Waterman, C. M. Orientation-specific responses to sustained uniaxial stretching in focal adhesion growth and turnover. *Proc. Natl. Acad. Sci. U. S. A.* **110,** E2352-61 (2013).
216. Guolla, L., Bertrand, M., Haase, K. & Pelling, a. E. Force transduction and strain dynamics in actin stress fibres in response to nanonewton forces. *J. Cell Sci.* **125,** 603–613 (2012).

217. Pelling, A. E., Veraitch, F. S., Chu, C. P.-K., Mason, C. & Horton, M. A. Mechanical dynamics of single cells during early apoptosis. *Cell Motil. Cytoskeleton* **66,** 409–422 (2009).
218. Esch, E. W., Bahinski, A. & Huh, D. Organs-on-chips at the frontiers of drug discovery. *Nat. Rev. Drug Discov.* **14,** 248–260 (2015).
219. Gupta, K. *et al.* Lab-on-a-chip devices as an emerging platform for stem cell biology. *Lab Chip* **10,** 2019–2031 (2010).
220. Zhang, L., Kahn, C. J. F., Chen, H. Q., Tran, N. & Wang, X. Effect of uniaxial stretching on rat bone mesenchymal stem cell: Orientation and expressions of collagen types I and III and tenascin-C. *Cell Biol. Int.* **32,** 344–352 (2008).
221. Carter, D. R. *et al.* The mechanobiology of articular cartilage development and degeneration. *Clin. Orthop. Relat. Res.* **427,** 69–77 (2004).
222. Schiele, N. R., Marturano, J. E. & Kuo, C. K. Mechanical factors in embryonic tendon development: Potential cues for stem cell tenogenesis. *Curr. Opin. Biotechnol.* **24,** 834–840 (2013).
223. Hashima, A. R., Young, A. A., McCulloch, A. D. & Waldman, L. K. Nonhomogeneous analysis of epicardial strain distributions during acute myocardial ischemia in the dog. *J. Biomech.* **26,** 19–35 (1993).
224. Chagnon-lessard, S., Jean-ruel, H., Godin, M. & Pelling, A. E. Cell Mechanosensing and Avoidance of Strain Gradients. *bioRxiv* 95976 (2016).
225. Sung, J. H. & Shuler, M. L. Prevention of air bubble formation in a microfluidic perfusion cell culture system using a microscale bubble trap. *Biomed. Microdevices* **11,** 731–738 (2009).
226. Zheng, W., Wang, Z., Zhang, W. & Jiang, X. A simple PDMS-based microfluidic channel design that removes bubbles for long-term on-chip culture of mammalian cells. *Lab Chip* **10,** 2906–2910 (2010).
227. Kolnik, M., Tsimring, L. S. & Hasty, J. Vacuum-assisted cell loading enables shear-free mammalian microfluidic culture. *Lab Chip* **12,** 4732 (2012).
228. Tonin, M., Descharmes, N. & Houdré, R. Hybrid PDMS/glass microfluidics for high resolution imaging and application to sub-wavelength particle trapping. *Lab Chip* **16,** 465–470 (2016).
229. Bianco, F. *et al.* Overflow microfluidic networks: Application to the biochemical analysis of brain cell interactions in complex neuroinflammatory scenarios. *Anal. Chem.* **84,** 9833–9840 (2012).
230. Sung, J. H., Kam, C. & Shuler, M. L. A microfluidic device for a pharmacokinetic-pharmacodynamic (PK-PD) model on a chip. *Lab Chip* **10,** 446–455 (2010).
231. Meza, D., Abejar, L., Rubenstein, D. A. & Yin, W. A Shearing-Stretching Device That Can Apply Physiological Fluid Shear Stress and Cyclic Stretch Concurrently to Endothelial Cells. *J. Biomech. Eng.* **138,** 31007 (2016).
232. Zheng, W. *et al.* A microfluidic flow-stretch chip for investigating blood vessel biomechanics. *Lab Chip* **12,** 3441–50 (2012).
233. Epshteyn, A. A. *et al.* Membrane-integrated microfluidic device for high-resolution live cell imaging. *Biomicrofluidics* **5,** 1–6 (2011).
234. Laasmaa, M., Vendelin, M. & Peterson, P. Application of regularized Richardson – Lucy algorithm for deconvolution of confocal microscopy images. **243,** 124–140 (2011).
235. Fouquet, C., Gilles, J., Heck, N. & Santos, M. Dos. Improving Axial Resolution in Confocal Microscopy with New High Refractive Index Mounting Media. 1–17 (2015). doi:10.1371/journal.pone.0121096
236. S. Hell, G. Reiner, C. Cremer, E. H. K. S. Aberrations in confocal fluorescence microscopy

induced by mismatches in refractive index. *J. Microsc.* **169,** 391–405 (1993).
237. Booth, M. J. Adaptive optics in microscopy. *Phil. Trans. R. Soc. A* **365,** 2829–2843 (2007).
238. Mata, A., Fleischman, A. J. & Roy, S. Fabrication of multi-layer SU-8 microstructures. *J. Micromechanics Microengineering* **16,** 276–284 (2006).
239. Bohl, B., Steger, R., Zengerle, R. & Koltay, P. Multi-layer SU-8 lift-off technology for microfluidic devices. *J. Micromechanics Microengineering* **15,** 1125–1130 (2005).
240. Guillot, C. & Lecuit, T. Mechanics of Epithelial Tissue Homeostasis and Morphogenesis. *Science (80-.).* **340,** 1185–1189 (2013).
241. Harris, A. R. *et al.* Characterizing the mechanics of cultured cell monolayers. *Proc. Natl. Acad. Sci.* **109,** 16449–16454 (2012).
242. Kajita, M. & Fujita, Y. JB Review EDAC : Epithelial defence against cancer — cell competition between normal and transformed epithelial cells in mammals. *J. Biochem.* **158,** 15–23 (2015).
243. Rajalingam, K., Schreck, R., Rapp, U. R. & Albert, ??tefan. Ras oncogenes and their downstream targets. *Biochim. Biophys. Acta - Mol. Cell Res.* **1773,** 1177–1195 (2007).
244. Slattum, G., Gu, Y., Sabbadini, R. & Rosenblatt, J. Autophagy in oncogenic K-Ras promotes basal extrusion of epithelial cells by degrading S1P. *Curr. Biol.* **24,** 19–28 (2014).
245. Gu, Y. *et al.* Defective apical extrusion signaling contributes to aggressive tumor hallmarks. *Elife* **2015,** 1–17 (2015).
246. Marshall, T. W., Lloyd, I. E., Delalande, J. M., Nathke, I. & Rosenblatt, J. The tumor suppressor adenomatous polyposis coli controls the direction in which a cell extrudes from an epithelium. *Mol. Biol. Cell* **22,** 3962–3970 (2011).
247. Bravo-Cordero, J. J., Hodgson, L. & Condeelis, J. S. Spatial regulation of tumor cell protrusions by RhoC. *Cell Adh. Migr.* **8,** 263–267 (2014).
248. Bao, G. *et al.* Molecular Biomechanics: The Molecular Basis of How Forces Regulate Cellular Function. *Mol. Cell* **3,** 91–105 (2010).
249. Jain, R. K., Martin, J. D. & Stylianopoulos, T. The role of mechanical forces in tumor growth and therapy. *Annu Rev Biomed Eng* **16,** 321–346 (2014).
250. Pathak, A. & Kumar, S. Independent regulation of tumor cell migration by matrix stiffness and confinement. *Proc. Natl. Acad. Sci.* **109,** 10334–10339 (2012).
251. Goldmann, W. H., Fabry, B., Klemm, A. H., Kienle, S. & Scha, T. E. Focal Adhesion Kinase Stabilizes the Cytoskeleton. **101,** 2131–2138 (2011).
252. Wang, H. B., Dembo, M., Hanks, S. K. & Wang, Y. Focal adhesion kinase is involved in mechanosensing during fibroblast migration. *Proc. Natl. Acad. Sci. U. S. A.* **98,** 11295–300 (2001).
253. Zhou, J. *et al.* Mechanism of Focal Adhesion Kinase Mechanosensing. *PLoS Comput. Biol.* **11,** 1–16 (2015).
254. Tomakidi, P., Schulz, S., Proksch, S., Weber, W. & Steinberg, T. Focal adhesion kinase (FAK) perspectives in mechanobiology: implications for cell behaviour. *Cell Tissue Res.* **357,** 515–526 (2014).
255. McLean, G. W. *et al.* The role of focal-adhesion kinase in cancer — a new therapeutic opportunity. *Nat. Rev. Cancer* **5,** 505–515 (2005).
256. Winklbauer, R. Cell adhesion strength from cortical tension – an integration of concepts. **2,** 3687–3693 (2015).
257. Wodarz, a & Nathke, I. Cell polarity in development and cancer. *Nat Cell Biol* **9,** 1016–1024 (2007).
258. Cowin, P., Rowlands, T. M. & Hatsell, S. J. Cadherins and catenins in breast cancer. *Curr. Opin. Cell Biol.* **17,** 499–508 (2005).

259. Cavallaro, U. & Christofori, G. Cell adhesion and signalling by cadherins and Ig-CAMs in cancer. *Nat. Rev. Cancer* **4,** 118–132 (2004).
260. Chang, Y.-W. E. & Jakobi, R. R. B. and R. Targeting RhoA/Rho Kinase and p21-Activated Kinase Signaling to Prevent Cancer Development and Progression. *Recent Patents on Anti-Cancer Drug Discovery* **4,** 110–124 (2009).
261. Marjoram, R. J., Lessey, E. C. & Burridge, K. Regulation of RhoA Activity by Adhesion Molecules and Mechanotransduction. *Curr. Mol. Med.* **14,** 199–208 (2014).
262. Lecuit, T. & Lenne, P.-F. Cell surface mechanics and the control of cell shape, tissue patterns and morphogenesis. *Nat. Rev. Mol. Cell Biol.* **8,** 633–644 (2007).
263. Bays, J. L. & DeMali, K. A. Vinculin in cell–cell and cell–matrix adhesions. *Cell. Mol. Life Sci.* **74,** 2999–3009 (2017).
264. Yamaguchi, H. & Condeelis, J. Regulation of the actin cytoskeleton in cancer cell migration and invasion. *Biochim. Biophys. Acta - Mol. Cell Res.* **1773,** 642–652 (2007).
265. Bravo-Cordero, J. J., Hodgson, L. & Condeelis, J. Directed cell invasion and migration during metastasis. *Curr. Opin. Cell Biol.* **24,** 277–283 (2012).
266. Hogan, C. *et al.* Characterization of the interface between normal and transformed epithelial cells. *Nat. Cell Biol.* **11,** 460–7 (2009).
267. Yamamoto, S. *et al.* A role of the sphingosine-1-phosphate (S1P)-S1P receptor 2 pathway in epithelial defense against cancer (EDAC). *Mol. Biol. Cell* **27,** 491–499 (2016).
268. Struckhoff, A. P., Rana, M. K. & Worthylake, R. A. RhoA can lead the way in tumor cell invasion and metastasis. *Front. Biosci.* **16,** 1915–26 (2011).
269. Lee, S. W. & Lee, S. S. Shrinkage ratio of PDMS and its alignment method for the wafer level process. *Microsyst. Technol.* **14,** 205–208 (2008).
270. Ji, N. Adaptive optical fluorescence microscopy. *Nat. Methods* **14,** 374–380 (2017).
271. Borysiak, M. D. *et al.* Simple replica micromolding of biocompatible styrenic elastomers. *Lab Chip* **13,** 2773–84 (2013).
272. DiFederico, E., Shelton, J. C. & Bader, D. L. Complex mechanical conditioning of cell-seeded agarose constructs can influence chondrocyte biosynthetic activity. *Biotechnol. Bioeng.* **114,** 1614–1625 (2017).